UNIVERSITY OF PORTSMOUTH

SCHOOL OF ENGINEERING

Mechanical Behaviour of Materials (MBM) Research Group

IMPACT OF P2RX7 PURINOCEPTOR ABLATION ON THE MORPHOMETRIC, MECHANICAL AND TISSUE PROPERTIES IN THE MURINE MODEL OF DUCHENNE MUSCULAR DYSTROPHY

by

Noor Shafini Mohamad

Thesis for the degree of Doctor of Philosophy

November 2016

Acknowledgment

Abstract

Duchenne muscular dystrophy (DMD) is an inherited, lethal disorder characterised by progressive muscle degeneration and associated bone abnormalities. It has previously demonstrated that P2RX7, a purinergic receptor, contributed to the pathogenesis of DMD, and found that P2RX7 ablation alleviated the severity of the disease. In this work a dystrophic *mdx* mouse crossed with the global P2RX7 receptor has been used to generate a knockout mouse model (*mdx*/P2X7$^{-/-}$), and compared its morphometric, mechanical and tissue properties against those of *mdx*, a mouse model without the dystrophin protein, as well as a wild type (WT) and a P2RX7 knockout (P2X7$^{-/-}$). Micro-computed tomography (μCT), three-point bending testing, scanning electron microscopy (SEM) and nanoindentation were utilised in the study. The bones were analysed at approximately 4 weeks of age to examine the impact of P2RX7 ablation on the bone properties during the acute disease phase, before muscle wasting is fully developed.

The results show that P2RX7 purinoceptor ablation has produced improvement or significant improvement in some of the morphological, mechanical and tissue properties of the dystrophic bones examined. Specifically, although the ablation produced smaller bones with significantly lower total cross-section area (Tt.Ar) and Second Moment of Area (SMA), significantly higher cortical bone area (Ct.Ar), cortical bone area ratio (Ct.Ar/Tt.Ar) and trabecular bone volume fraction (BV/TV) are found in the *mdx*/P2X7$^{-/-}$ mice than in any other types. Further, the *mdx*/P2X7$^{-/-}$ bones have relatively higher average flexural strength, work-to-fracture and significantly higher strain to failure compared with those of *mdx*, suggesting greater resistance to fracture. Indentation modulus, elasticity and creep are also significantly improved in the knockout cortical bones over those of *mdx*. These findings seem to suggest that specific pharmacological blockade of P2RX7 may improve dystrophic bones, with a potential for therapeutic application in the treatment of the disease.

Published Papers

1. Sinadinos, A., Young, C., Al-Khalidi, R., Teti, A., Kalinski, P., **Mohamad, S.**, Floriot, L., Henry, T., Tozzi, G., Jiang, T., Wurtz, O., Lefebvre, A., Tong, J., Vaudry, D., Arkle, S., DoRego, J.-C., Gorecki, D., Shugay, M., 2015. P2RX7 Purinoceptor: A Therapeutic Target for Ameliorating the Symptoms of Duchenne Muscular Dystrophy. PLoS Med 12(10), 1–33. doi:10.1371/journal.pmed.1001888

2. **Mohamad, N.S.**, Sinadinos, A., Górecki, D.C., Zioupos, P., Tong, J., 2016. Impact of P2RX7 ablation on the morphological, mechanical and tissue properties of bones in a murine model of Duchenne Muscular Dystrophy. J. Biomech. 49, 3444–3451. doi:10.1016/j.jbiomech.2016.09.016

Table of Contents

Author's Declaration

Whilst registered as a candidate for the above degree, I have not been registered for any other research award. The results and conclusions embodied in this thesis are the work of the named candidate and have not been submitted for any other academic award.

Shafini

Signature:………………………………………..…………………………………….

Noor Shafini Mohamad

Abbreviations

ANOVA	Analysis of Variance
BV/TV	Bone Volume/ Total Volume
BMD	Bone Mineral Density
BMU	Basic Multicellular Unit
DICOM	Digital Imaging and Communications in Medicine
HA	Hydroxyapatite
kVp	kilovolts peak
MC	Marrow Cavity
PS	Primary Spongiosa
ROI	Region of Interest
SEM	Scanning Electron Microscopy
SD	Standard Deviation
SNR	Signal-to-Noise Ratio
TB	Trabeculae
V	Tube Voltage
I	Tube Current
Z	Atomic Number
µCT	Micro Computed Tomography

Glossary

Gene   A gene is a functional unit, usually encoding a protein or RNA, whose inheritance can be followed experimentally.

Mutation   A mutation is a particular class of variant allele that usually confers a phenotypically identifiable difference to a reference "wild type" phenotype.

Recessive   A recessive phenotype is one that is only detected when both alleles have a particular variant or mutation

Genotype   Genotype is the description of the genetic composition of the animals, usually in terms of particular alleles at particular loci.

Phenotype   Phenotype is the result of interaction between genotype and the environment and can be determined by any assay.

Z-score   It can be derived by any value in such a set of data by dividing the value of its difference from the mean by standard deviation (SD) value.

Cardiomyopathy   The heart muscle becomes enlarged, thick, or rigid. In rare cases, the muscle tissue in the heart is replaced with scar tissue

Sarcolemma   Also called the myolemma, is the cell membrane of a striated muscle fiber cell.

Myolemma   The thin, transparent, extensible membrane covering every striated muscle fiber.

Promoter   A region of DNA that initiates transcription of a particular gene. Promoters are located near the transcription start sites of genes, on the same strand and upstream on the DNA.

DAP	Dystrophin-associated protein is a protein that helps to form the connection between intracellular dystrophin and the extracellular basal lamina.
GABA	Gamma-aminobutyric acid (GABA) is a major inhibitory neurotransmitter in the central nervous system.
Paracrine signaling	A form of cell-to-cell communication in which a cell produces a signal to induce changes in nearby cells, altering the behaviour or differentiation of those cells.
SAMR1	Age-matched normal mouse or control
SAMP6	Senescence-accelerated mouse or senile osteoporosis
PND 35	Postnatal days 35
PND 70	Postnatal days 70
$Ahr^{-/-}$	Aryl hydrocarbon receptor (AHR) knockout. It is a ligand-activated transcriptional regulator, is ubiquitously expressed in most organs and can be activated by a structurally diverse range of chemicals of which the best characterised ones include a variety of environmental contaminants.
$Ahr^{+/+}$	Wild-type or control
TCDD	2,3,7,8-tetrachlorodibenzo-p-dioxin is a polychlorinated dibenzo-p-dioxin (sometimes shortened, though inaccurately, to simply "dioxin") with the chemical formula $C_{12}H_4Cl_4O_2$. TCDD is a colourless solid with no distinguishable odour at room temperature. It is usually formed as a side product in organic synthesis and burning of organic materials.

Chapter 1

Introduction

Duchenne muscular dystrophy (DMD) is the most common type of muscular dystrophy. It is a debilitating disease causing progressive muscle degeneration leading to severe disability and death of young men. DMD is also associated with cognitive impairment. Loss of dystrophin in DMD disrupts structural scaffolds for dystrophin-associated proteins as well as specific signaling processes, causing cognitive and behavioural impairment and bone structure abnormalities (Blake et al., 2002), both independent of functional muscle impairment. Both patients (Rufo et al., 2011) and *mdx* (DMD model) mice (Nakagaki et al., 2011) were found to have lower bone mass, which is strongly associated with the degree of motor function and muscle strength. The decline in bone mineral density is usually attributed to the progressive muscle fiber degeneration, although there may be other factors inherent to the disease which also contribute to bone tissue impairment (Akhter et al., 2004; Beaupied et al., 2007; Nakagaki et al., 2011).

The ability of bone to adapt to mechanical loads is usually linked to muscle activity, and bone loss in muscle paralysis is indicative of the importance of mechanical stimulation for bone regulation. In the late stages of DMD progression, the impact of muscle loss on the dystrophic bone structure is evident. However, early bone abnormalities found prior to substantial muscle loss indicate that there may be other factors inherent to DMD, which also contribute to the loss of bone mass (Anderson et al., 1993; Bianchi and Morandi, 2008; Nakagaki and Camilli, 2012). Studies by Anderson et al. (1993), Rufo et al. (2011) and Novotny et al. (2011) showed up to 50% loss in strength and stiffness in *mdx* mouse model of DMD compared to those of the control, resulting in the development of micro-damage (Saito and Marumo, 2010) and bone fracture (Bianchi and Morandi, 2008).

As a result of low bone mass, DMD patients have significant increased risk of fracture (McDonald et al., 2002; Pouwels et al., 2013; Vestergaard et al., 2001) and commonly sustain low-energy fractures. Falling was the most common mechanism of fracture affecting mostly in the lower limb (McDonald et al., 2002). Early bone abnormality studies on mice bone have revealed severely reduced bone mass

causing bone structural changes. The structural changes in bone are sensed by bone cells which adjust bone tissue mass and architecture in response to the mechanical load applied (Anderson et al., 1993).

Bone tissue consists of organic and inorganic materials, such as minerals including calcium, phosphate and collagen. These elements make the bone tissue strong, and one of the most rigid structures in the body (Dalla and Bankoff, 2012). For example, collagen gives the bone tissue properties such as flexibility and the ability to support tensile loads, while minerals support compressive loads. It is essentially a complex viscoelastic composite with hierarchically organised structure (Figure 1-1). It has regular, yet optimised, arrangement and orientation of the components, making bone as a heterogeneous and anisotropic material (Rho et al., 1998).
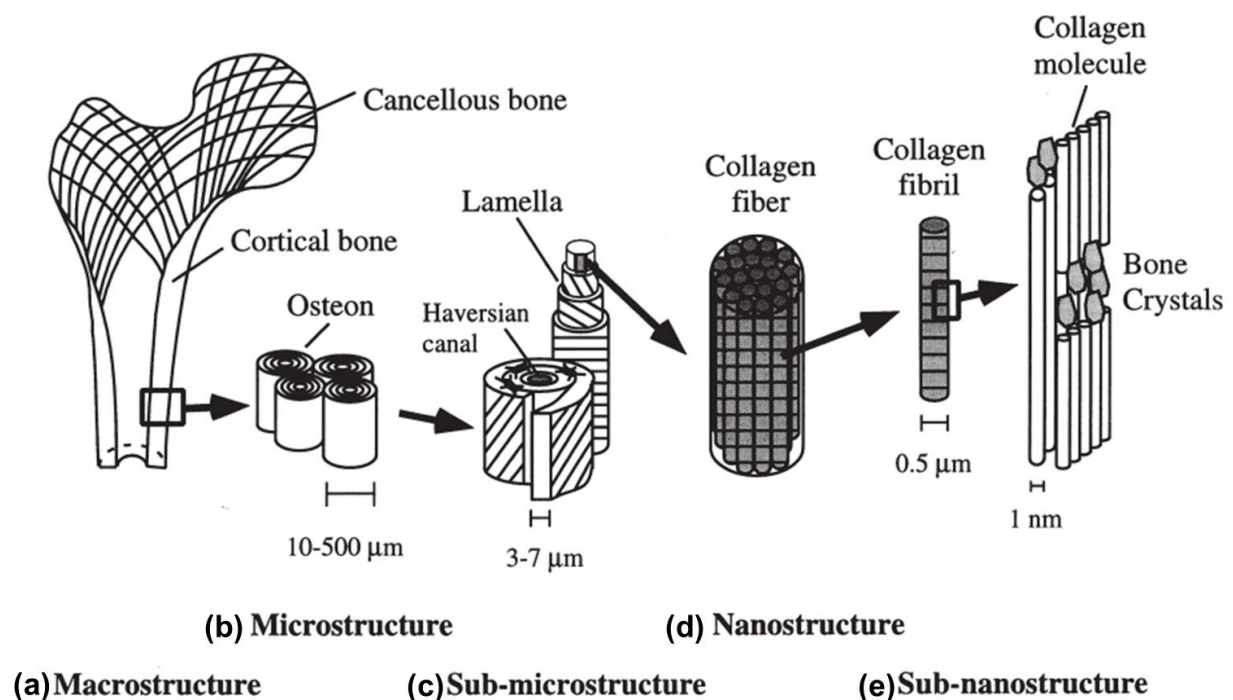
Figure 1-1 Hierarchical structural organisation of bone.
(a) cortical and cancellous bone; (b) osteons with Haversian systems; (c) lamellae; (d) collagen fiber assemblies of collagen fibrils; (e) bone mineral crystals, collagen molecules, and non-collagenous proteins (Rho et al., 1998).

Frost (Frost, 1987) was the first to articulate the importance of functional bone strain as a controlling stimulus for bone architecture, a relationship that has come to be known as the mechanostat, which is a model describing bone growth and bone loss.

2

It is a refinement of Wolff's law described by Julius Wolff (1836–1902). He suggested that survival of the skeleton (but also of other tissues, such as fibrous tissue, hyaline cartilage, fibrocartilage, cementum, or dentin) requires the functional coordination of modeling and remodeling. Modeling adapts bone to overloads, by enhancing additions of new bones and by changing bone architecture, and remodeling adapts bone to underloads by removing bone next to marrow and conserving normally used bone. Bone growth and bone loss is stimulated by the local mechanical elastic deformation of bone. Generally strains lower than 800µStrain would lead to resorption; a strain between 800µStrain and 1500µStrain would lead to bone adaptation, whilst over 1500µStrain leads to overload and fracture occurs at approximately 15000µStrain. There is a mechanism that monitors bone metabolism (longitudinal growth, bone modeling, and remodeling activities) in relation to mechanical usage (Tyrovola, 2015).

Several scenarios have been envisaged on the mechanisms behind the DMD bone abnormality (Abou-Khalil et al., 2013; Bianchi et al., 2003; Rufo et al., 2011). DMD causes absence of dystrophin, which disrupts structural scaffolds involving dystrophin-associated proteins and loss of anchoring for specific signaling proteins (Blake et al., 2002). Therefore, the absence of dystrophin could be directly responsible for bone structure alterations. However, there is no data on dystrophin being expressed in osteoblasts or osteoclasts. On the other hand, dystrophic muscle degeneration is associated with chronic sterile inflammation. Abou-Khalil et al. (2013) demonstrated that chronic inflammation contributes to dystrophic bone damage. In DMD patients, prolonged corticosteroid treatment can further exacerbate this abnormality (Bianchi et al., 2003; Söderpalm et al., 2007).

Genetic knockout mice have been widely studied to demonstrate the improvement or deterioration of diseases (Nakagaki et al., 2011). This approach has great significance in alternative therapeutic advances targeted towards clinical application in humans. Knockout mice have one or more genes disrupted to develop an animal model for a certain disease. These genetically disrupted mice can then be investigated to understand the physiology of their function, which can be applied to others. The characteristics of the animal models can be demonstrated through symptoms that depend on which genes or receptors are altered.

DMD gene mutations are associated with P2RX7 purinoceptor up-regulation, which leads to the death of human DMD lymphoblasts (Ferrari et al., 1994) and muscles in the *mdx* mouse model of DMD (Yeung et al., 2006; Young et al., 2012, 2013). P2RX7 activation in *mdx* muscles triggers a specific mechanism of autophagic cell death (Young et al., 2015). Recent work showed that this receptor is a good target for pharmacological treatment of DMD, as its genetic ablation (knockout) reduced both muscle loss and inflammation (Sinadinos et al., 2015). P2RX7 is expressed in both osteoblasts and osteoclasts, but it appears to have different roles in bone physiology and in disease states. Unfortunately, what these roles are is still unclear as different P2RX7 knockouts produced conflicting results on whether it affects bone formation or bone resorption or both. In this work, the influence of P2RX7 inhibition on the morphological and the mechanical behaviour of the bones were examined. Given that the bone abnormalities in *mdx* mice have been linked to chronic inflammation (Abou-Khalil et al., 2013), the reduced inflammation found in *mdx*/P2X7$^{-/-}$ muscles (Sinadinos et al., 2015) may be responsible for the reduced bone loss in these mice. If P2RX7 is abnormally active in dystrophic bones, its absence might improve the bone properties. On the other hand, activation of P2RX7 receptor has been linked primarily to osteoclast functions (Agrawal and Gartland, 2015; Agrawal et al., 2003; Gartland, 2012), hence its ablation could have a negative impact on the bone. It is hypothesise that P2RX7 ablation would not exacerbate the dystrophic bone phenotype. To test the hypothesis, a previously established double mutant (*mdx*/P2X7$^{-/-}$, Sinadinos et al. 2015) has been used, examined the morphometric, mechanical and tissue properties of long bones of *mdx*/P2X7$^{-/-}$ mice against those of *mdx* as well as wild type (WT) and P2RX7 knockout (P2X7$^{-/-}$) mice.

Young et al. (2012) reported that there was abnormally high activity of P2RX7 in the dystrophic muscle. Based on the alleviation of symptoms in *mdx* mice with the P2RX7 receptor disrupted (Sinadinos et al., 2015), it was concluded that the P2RX7 disruption improved the dystrophic mice bone and muscle in six-month-old mice. The positive impact of depletion of P2RX7 on bone tissue could be investigated using non-destructive μCT, which has significant advantages in terms of imaging the tissue at high resolution.

Biomedical imaging technology is of vital importance in the field medical diagnosis. Its contribution brings new knowledge leading to improved life for future generations.

There is no doubt that biomedical imaging has facilitated new treatments to disease. This is due to its unique ability to provide anatomical and physiological information. In humans, imaging modalities such as conventional x-ray, computed tomography (CT), magnetic resonance imaging (MRI) and ultrasound are well-established tools in modern medicine. They have made great contributions towards detecting and characterizing pathologies in humans, such as cancer. The same applies to animal research studies. The development of μCT has created a system that allows researchers to see the microstructure of animals without destroying tissues. This is of great significance in modern medicine, as it enables study of disease at the molecular level (Paulus et al., 2000; Ritman, 2006, 2002; Schambach et al., 2010).

Previous literature applying μCT and histomorphometry on *mdx* and wild-type mice has found evidence that bone tissues are affected in *mdx* mice similar to low Z-scores observed in patients (Nakagaki and Camilli, 2012; Rufo et al., 2011). Z-score is a measure of bone mineral apparent density (BMAD) using DXA machine. It is the number of standard deviation by comparing a measurement to a reference sample of age- and gender-matched of healthy population. However, both the segmentation and the image analysis methods used to image mice bones are in need of updating (Rufo et al., 2011). The techniques used in this work therefore aim to extend previous work by combining μCT with image processing tools such as ImageJ/BoneJ plugins to quantify the skeletal phenotype of two knockout mice, as well as wild-type and dystrophic mice. An extended study using a three-point bending technique to determine the mechanical properties of the bone has also been conducted across the genotypes. A study of fracture mechanisms using the Scanning Electron Microscopy (SEM) has been used later to examine the micro-fracture paths and fracture modes. This is followed by a nanoindentation experiment to further compare the material properties of the mice bone at a microscopic level. This is the first time such technique has been used for the assessment of bone across the genotypes.

Description of Gaps in Research Literature

The effect of P2RX7 disruption on bone morphology is unclear. There is no research data on the effects of the ablation of the receptor on bone morphology and properties in mice at an early age (four-week), or the impact of this receptor on *mdx* bones. Using the imaging protocol to create high-resolution μCT images, the bone

morphologies of knockout, *mdx* and wild-type mice can be quantified and compared. Furthermore, the biomechanical properties obtained from the mechanical testing can provide useful insight into the mechanical behaviour of the bones. Although several studies have reported on the biomechanical, biochemical and morphometry properties of *mdx* mice and control mice, there is no report on the tissue properties of the bones across the genotypes.

Research Questions

The fundamental question that motivates this doctoral research is: What role does the P2RX7 receptor play in the DMD disease process? To answer this question, the aim and objectives are given below.

Statement of Aims

Overall Aim

The aim of this work is to develop an understanding of morphological and mechanical behaviour of mouse bone across the genotypes, by imaging hard tissues using micro-computed tomography, mechanical testing and nanoindentation to evaluate the structural, material and tissue properties of the bones.

Objectives

1: To compare the morphometric properties of different genotypes using micro CT imaging

Utilising a state-of-the-art µCT scanner, imaging protocols were used to image mice tibias of four different genotypes.

Recent evidence suggests that, at three weeks of age, *mdx* mice show bone abnormalities that are unlikely to be caused by muscle irregularities (Nakagaki et al., 2011). For this reason, bones of wild-type, *mdx* and P2RX7 knockout and double knockout of four-week-old mice were used to establish whether blocking this receptor would have a direct effect on the bone structure.

Following µCT imaging and subsequent 3D reconstruction of the four genotypes, including P2RX7 knockout mice, the images underwent processing using semi-automated segmentation implemented in ImageJ (USA). The morphological

parameters implemented in BoneJ (Doube et al., 2010) involved were bone volume/total volume (BV/TV), trabecular thickness (Tb.Th), trabecular spacing (Tb.Sp) and connectivity density (Conn.D) at the proximal metaphyseal tibia, and total cross-sectional area (Tt.Ar), cortical bone area (Ct.Ar), and cortical area fraction (Ct.Ar/Tt.Ar) at the midtibia. These parameters define the bone structure and distribution for each genotype. Assessing whether disruption or blockade of the P2RX7 receptor can improve both muscles and bones in dystrophic mice is of great significance for the treatment of DMD, as all alternative therapeutic approaches used so far (including gene therapy) only target muscles.

2. To evaluate the biomechanical properties of bone across the genotypes.

Understanding how the bone responds to mechanical stress requires a description of the mechanical behaviour of bones. Thus, three-point-bending mechanical testing was carried out to assess the structural and material properties of the bones across the genotypes to assess the effects of the absence of dystrophin and P2RX7 receptors. The results were analysed together with the morphometric properties (1).

3. To evaluate the tissue properties of the bones across the genotypes

Nanoindentation was carried out to assess the bone tissue properties across the genotypes, and the results were analysed together with the morphometric properties (1) and structural and material properties (2).

Chapter 2

Literature Review

2.1 Bone Structure and Composition

Bone of present-day mammals and birds is a stiff skeletal material made principally of the fibrous protein collagen, impregnated with a mineral closely resembling calcium phosphate. Bone also contains water, which is very important mechanically. Bone is the only structure that is essentially collagen mineralised with calcium phosphate and containing cell bodies (Currey, 2002).

2.1.1 Bone Tissue

Bone tissues are organised in a hierarchical level as shown in Table 2-1 and Figure 2-1 (Rho et al., 1998).

Table 2- 1 Bone Hierarchical Structure.

Level	Structure
Macrostructure	Cortical bone and trabecular bone
Microstructure (10-500 µm)	Haversian systems, osteons, single trabeculae
Sub-microstructure (1-10 µm)	Lamellae
Nanostructure (from a few hundred nanometers to 1 µm)	Fibrillar collagen, embedded minerals
Sub-nanostructure (below a few hundred nanometers)	molecular structure of constituent elements, such as mineral, collagen, non-collagenous organic proteins

At the macrostructure level, bone consists of cortical bone and trabecular bone. The trabecular bone is actively remodelled compared with the cortical bone. Every year, 25% of trabecular bone whilst 2–3% of cortical bone undergoes remodelling (Swaminathan, 2001). In remodelling the bone involved is usually a small individual

packet called a basic multicellular unit (BMU), and typically the amount of bone remaining after the process is little changed; new bone has more or less replaced old bone. Therefore, the trabecular bone is considered younger than the cortical bone (Currey, 2002).

At the microstructure level, the bone is composed of mineralised collagen fibres stacked parallel to form layers, called lamellae. All mature bone is mostly lamellar. It also exists in a separate form: Haversian systems (used by British and other European) or secondary osteons (used by Americans) (Currey, 2002).
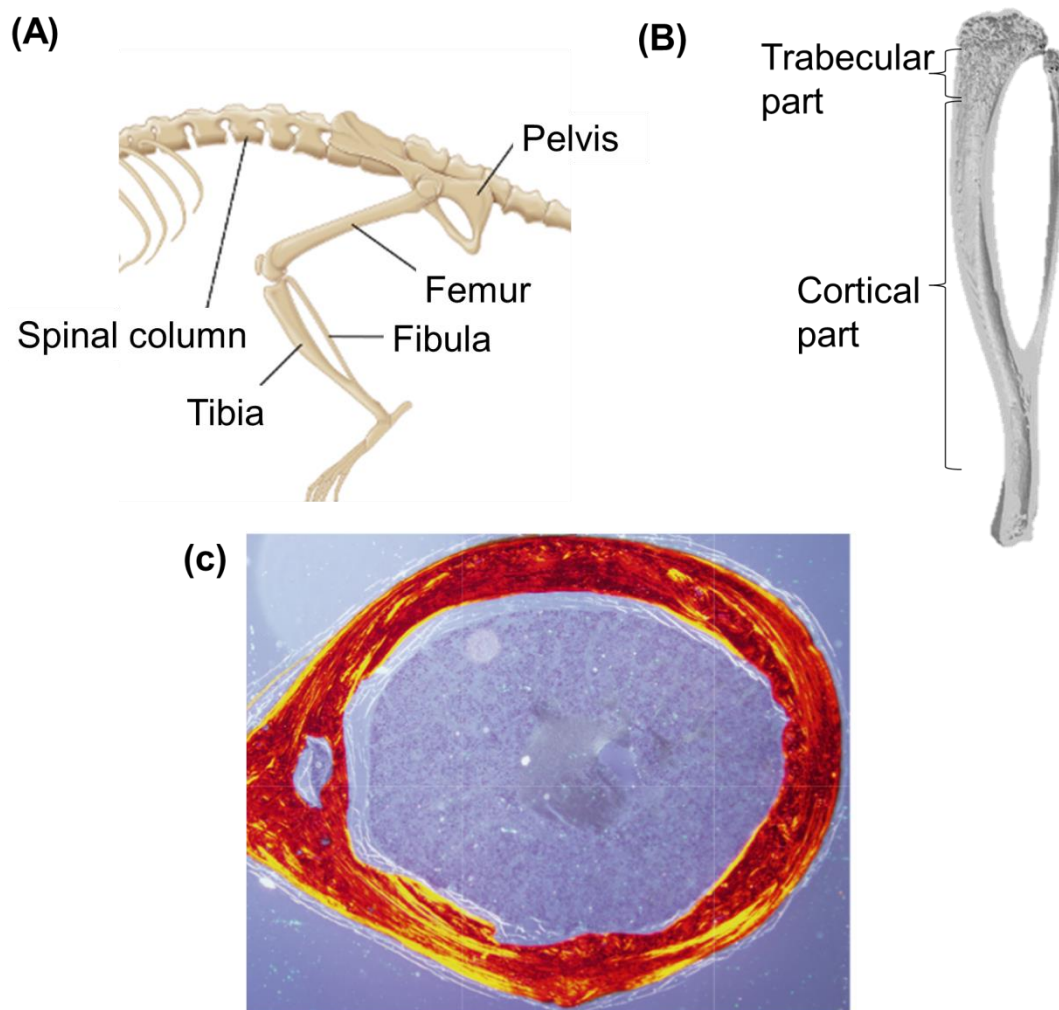
Figure 2-1 Bone structure.
(A) A gross anatomy of a mouse skeleton. (B) A mouse tibia bone showing the cortical part at diaphysis and trabecular part at the metaphysis towards the periphery. (C) A histological image of a transverse section of mouse cortical bone showing the circumferential lamellae. Cortical bone remodeling is rare in mice, and most of the cortex comprises circumferential lamellae laid down on the outer

(periosteal) surface as the bone grows. While the remnants of the less well-organised bone formed during endochondral ossification are seen on the inner (endosteal) surface (Adapted from Human and Mouse Atlas, 2012).

2.1.1.1 Cortical bone

Cortical bone, in both human and mouse species, forms a majority of the long bone diaphysis such as tibia and femur, and it surrounds a medullary cavity filled with yellow bone marrow that is mostly made of fat cells (Hadjidakis and Androulakis, 2006; Treuting and Dintzis, 2012). Cortical bone has higher volume fraction of mineralised material (90-95%) and lower surface area than trabecular bone. This is due to a slower turnover rate compare to that of trabecular bone. In human and mammalian bones, the cortical bone porosity is usually less than 5% (Clarke, 2008). In mice, the cortical bone comprises a mixture of woven bone formed by endochondral ossification and circumferential lamellar bone laid down on the outside. In very young mice, the diaphyseal cortex contains a high proportion of woven bone. As the mouse ages, the woven bone is lost, and only circumferential lamellae remain. Mouse diaphyseal cortical bone rarely undergoes Haversian remodelling seen in human bone, thus does not usually contain osteons (Figure 2-1). Although there are no Haversian Systems (osteons), marrow-filled intracortical porosities develop with age. In contrast to mice, human cortical bone is composed of osteons circumferential lamellae on the outer and inner surfaces and interstitial lamellas between osteons (Figure 2-2).
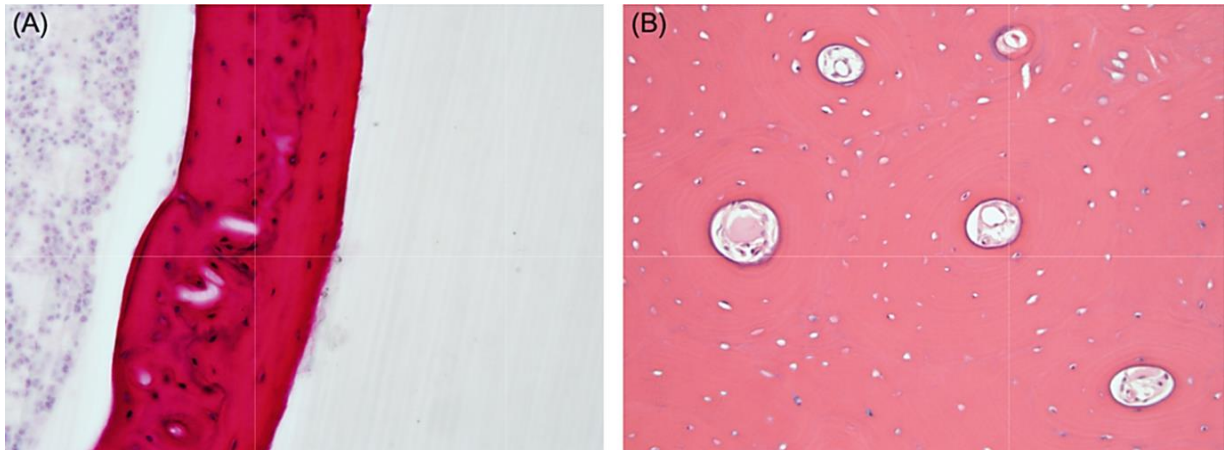
Figure 2-2 (A) In a mouse model, the cortex comprises a mixture of woven bone formed by endochondral ossification and circumferential lamellar bone laid down on the outside. As the mouse ages, the woven bone is lost, and only circumferential lamellae remain. Although Haversian systems (osteons) and marrow-filled intracortical porosities do not develop with age. (B) In humans, Haversian systems (osteons) are the product of remodeling of bone and comprise a central vascular channel surrounded concentrically by bone lamellae. Continuous remodeling leads to overlapping, partial osteons (Adapted from Human and Mouse Atlas, 2012).

2.1.1.2 Trabecular bone

Trabecular bone is also known as spongy or cancellous bone. It has a porous structure where the spaces are filled with bone marrow and blood vessels. In mice, the primary spongiosa, comprised of bony trabeculae with cartilage cores and relatively little marrow space, lies in the first 250 μm or so below the cartilage growth plate (Figure 2-3) (Treuting and Dintzis, 2012). It is believed that trabecular bone plays an important role in supplying nutrients to the bone and has a relatively high metabolic activity (Hadjidakis and Androulakis, 2006). In very young mice, trabecular bone is woven in structure. Trabecular bone more actively remodels itself than does the cortical bone. As a result, trabecular bone is younger than the more mature cortical bone. Similar to human, trabecular bone of mice also remodels. Trabecular bone turnover in mice is approximately 0.7% per day as measured in the distal femur. Each episode of remodeling takes about 2 weeks to complete. In human, bone turnover is about 0.1% per day and each remodeling takes about 6-9 months to

complete. Age-related changes in bone mass in mice are dominated by age-related factors, not sex steroid deficiency as in both human and rodents. Knowledge of the causes of the disease in mice should therefore be applicable to human when the inherent limitations are recognised (Jilka, 2013).
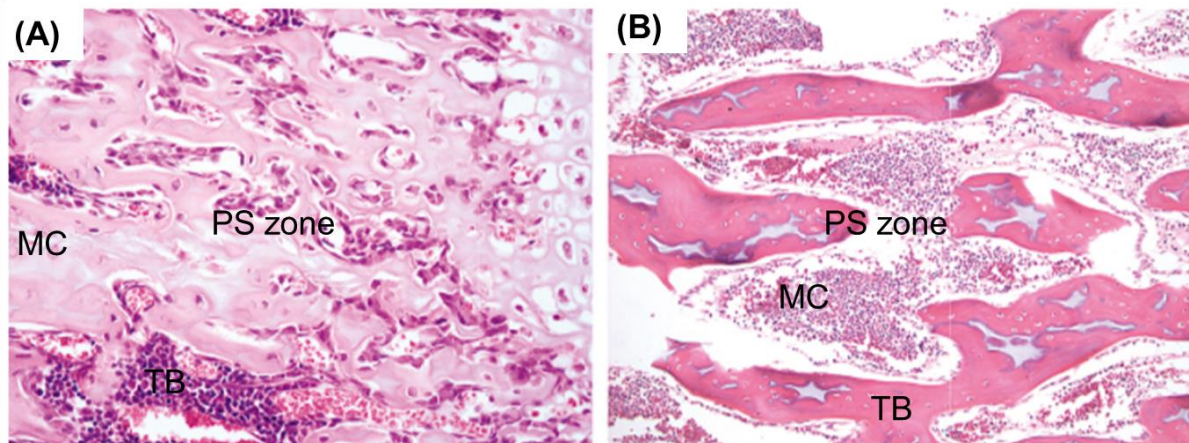
Figure 2-3 Histological images of immature trabecular bone.
(A) In 6-week old mice, cartilage cores are present in trabeculae (TB) of the primary spongiosa (PS). The marrow cavity (MC) predominantly filled by hemopoietic tissue. (B) In human fetal bone, the trabeculae have cartilage cores that are remnants of the cartilage anlagen or growth plate (Adapted from Human and Mouse Atlas, 2012).

2.1.2 Bone Matrix

Bone matrix consists of water, the organic materials (collagen and non-collagenous proteins) and inorganic materials (mineral crystals) (Currey, 2002). The major organic constituent of bone is type I collagen, with trace amount of types III and V and FACIT collagens (Clarke, 2008). Type I collagen represents approximately 90% of the organic composition of the whole bone tissue. The inorganic materials known as crystals of hydroxyapatite (HA) [$3Ca_3(PO_4)_2 \cdot (OH)_2$] are found within the collagen fibres in the bone matrix, they tend to be oriented in the same direction as the collagen fibres (Hadjidakis and Androulakis, 2006).

2.1.3 Bone Cells

Bone is permeated by and lined by various kinds of specialised cells. There are four commonly known types of bone cells (Figure 2-4). The bone lining cells, osteoblasts, and osteoclasts cover the bone tissue surface while osteocytes are imprisoned in the hard bone tissue and connect with neighbouring osteocytes (Currey, 2002; Hadjidakis and Androulakis, 2006).

Osteocyte (maintains bone tissue) **Osteoblast** (forms bone matrix) **Osteogenic cell** (stem cell) **Osteoclast** (resorbs bone)
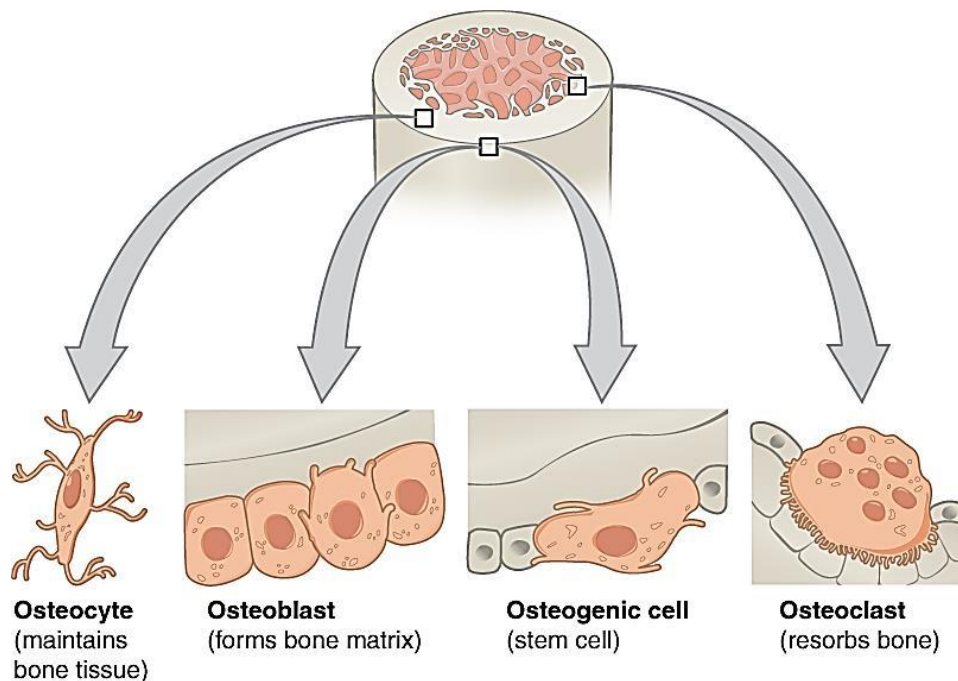
Figure 2-4 Four types of cells are found within bone tissue.
Osteogenic cells are undifferentiated and develop into osteoblasts. When osteoblasts get trapped within the calcified matrix, their structure and function changes, and they become osteocytes. Osteoclasts develop from monocytes and macrophages and differ in appearance from other bone cells (http://cnx.org).

2.1.4 Osteoblasts and Osteocytes

Osteoblasts derive from bone lining cells and are responsible for the formation of bone. They initially lay down the collagenous matrix, osteoid, in which mineral is later deposited, and they probably also have a role in its mineralisation (Currey, 2002). Osteoblasts do not function individually but are found in clusters along the bone surface, lining on the layer of bone matrix that they produce. They originate from

multipotent mesenchymal stem cells, which have the capacity to differentiate into osteoblasts, adipocytes, chondrocytes, myoblasts, or fibroblasts (Hadjidakis and Androulakis, 2006). As the new bone is formed, a small number of osteoblasts are trapped within the newly formed matrix and become osteocytes. The osteocytes are connected to each other and to the bone lining cells through a dense network of channels called canaliculli. They are responsible for regulating the bone remodelling by maintaining the oxygen and mineral levels in the bone through homeostasis process. In cancellous bone the density of the osteocytes varies from about 90,000 mm^{-3} in rats to about 30,000 mm^{-3} in cows. In general, the larger the animal, the lower the density of osteocytes (Currey, 2002).

Osteocytes are responsible for detecting and responding to mechanical loading and initiating the bone adaptation process. Osteocytes support osteoclast formation and activation when direct cell to cell contact with osteoclast precursors is allowed (You et al., 2008; Zhao et al., 2002). In addition, You et al. (2008) identified soluble signals as a mechanism osteocytes might use to regulate osteoclast formation due to mechanical loading.

2.1.5 Osteoclasts

Another type of bone tissue maintaining cells is osteoclasts. Osteoclasts are multinucleated cells derived from the monocytes which originate from bone marrow. Unlike osteoblasts, they are responsible for the resorption and replacement of old and damaged bone matrix. Osteoclasts are important in liberating minerals and other molecules stored in the bone matrix. They secrete an acid phosphatase to a specific site of the bone and unfix calcium in the mineralised bone to break it down. In time-lapse photography they give the appearance of being extremely aggressive, clamping themselves to the bone's surface and leaving a space underneath a ruffled border that is very mobile and beneath which the bone can be dissolving. Debris, both organic and mineral, are packed into little vesicles and pass through the cell body of the osteoclast and are dumped into the space above. When osteoclasts have done their job they disappear and presumably die (Currey, 2002).

The presence or absence of mechanical stimulation have been reported by previous studies to affect the bone homeostasis, in association with osteoporosis

(Manolagas, 2000). A study in mice has shown that bone resorption is amplified in the absence of mechanical loading. The osteocytes might serve to attract and guide active osteoclasts to replace regions of damaged and disused bones (You et al., 2008).

2.1.6 Bone Remodeling

Bone remodelling is a complex process to replace old with new bone tissues, and the interaction between the different cells is regulated by biochemical and mechanical factors (Hadjidakis and Androulakis, 2006). Bone cells include osteoblasts and osteoclasts responsible for formation of bone and break down the bone tissue to allow new bone formation, respectively. The functions of the bone cells are critical in providing bone tissue maintenance, repair and remodelling.

Figure 2-5 shows a basic human bone remodeling process at 3-weeks and 3-months, involving the bone cells and hormone regulator (i.e. parathyroid hormone (PTH), Calcitonin and Vitamin D). This process is important in both human and mice skeletal systems in order to maintain the homeostasis of the calcium and the integrity of bone structure. Histologically, the basic bone remodeling processes are similar. However, mouse cortical bone rarely undergoes Haversian remodeling as seen in human bone, and the mouse cortex mostly comprises circumferential lamellae instead of the osteonal structures common in human (Treuting and Dintzis, 2012).

Bone Remodeling Cycle
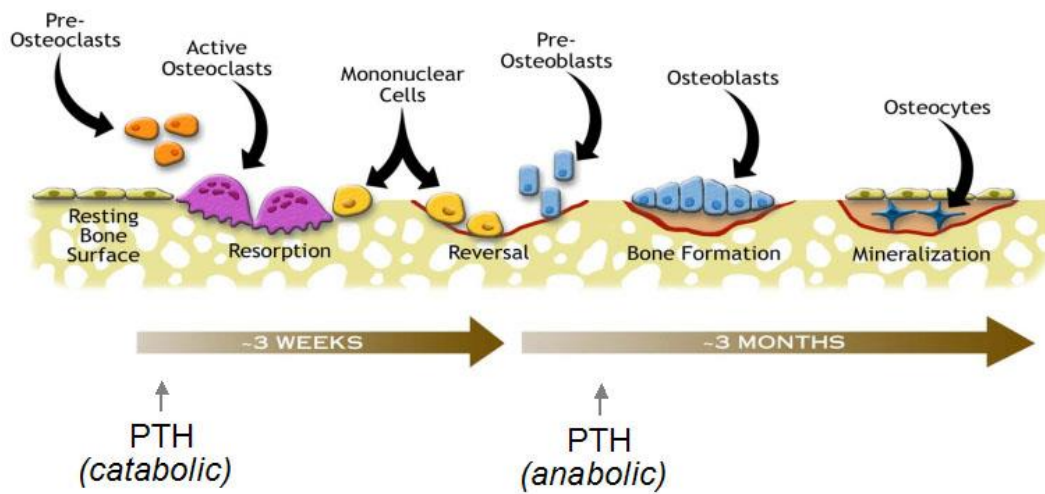
Figure 2-5 An illustration of cells involved in bone remodeling cycle.
The remodeling cycle consists of three phases: (1) resorption, at which point the osteoclasts digest old bone; (2) reversal, when mononuclear cells appear on the bone surface; and (3) formation, when osteoblasts form new bone in place of what has been resorbed (www.sierrasil.com).

It is also essential to subsequently remodel woven bone into mature lamellar bone. At the nano-structural level, the bone lining cells regulate the movement of ions between the plasma and the bone, and they can be found on all surfaces of the bones. Osteoblasts are responsible for developing new bone tissues. Osteoblasts are thought to be derived from cells associated with blood vessels. Once active, they start to produce the organic component of bone which is osteoid. Osteoid is predominantly made from collagen. Minerals start to crystallise around the collagen scaffold to form Hydroxyapatite (HA) which contains calcium phosphate.

2.1.7 Bone Mechanotransduction

Several studies have investigated the mechanisms of impact of mechanical loading on bone cells. The transduction of the mechanical signals into the bone cells is

termed bone mechanotransduction. The process is important for the maintenance of skeletal homeostasis in human adults. At cell level, the applied mechanical forces are sensed by individual cells or certain sensor cells, and the sensation is active at the cellular level. At tissue level, this will generate biochemical signals in order to transduce the mechanical signals and modulate bone formation and resorption (Sikavitsas et al., 2001).

It is believed that the mechanical properties of bone depend on a multi-level bone structure (Weiner and Wagner 1998; Rho et al., 1998). There is a correlation between the bone structures and their mechanical functions. Different levels of bone structure may provide information on various pathological diseases such as aging, osteoporosis, osteoarthritis and other degenerative diseases (Rho et al., 1998). In their review, Rho et al. (1998) highlighted several research challenges that may advance our knowledge of bone structure as a structure and as a material.

The adaptation of bone to mechanical stimulation is important to initiate osteogenesis process. When a body is subjected to external loading, the muscles will be stimulated to adapt to the loading conditions and their activities increased. This will in turn stimulate the bone cells and initiate the bone formation. By contrast, when mechanical stimulation is lacking, the bone will respond by reducing its density that may lead to bone resorption and fracture. A study by Oppl et al. (2014) on human subjects suffering from immobilization or disuse of the musculoskeletal system found profound reduction in whole body bone density. In the animal study, the importance of mechanical adaptation of bone structures in mice was shown in a report by Fritton et al. (2005). They showed an increase of 9% to 14% bone mineral content in proximal metaphysis of mouse tibia at 2 and 6 weeks of age, respectively, due to increased controlled cyclic axial loading. Findings of Lynch et al. (2010) supported the report of Fritton et al. (2005), where enhanced trabecular bone mass and density regardless of sex were found when dynamic compressive loads were applied. These findings open up further research opportunities in the use of mechanical loading to enhance bone mass and to combat low bone mass related diseases, such as osteoporosis.

2.2 Duchenne Muscular Dystrophy (DMD)

Duchenne Muscular Dystrophy (DMD) is the most common and severe form of muscular dystrophy affecting 1 in 5000 boys (McGreevy et al., 2015; Pant et al., 2015). It causes progressive muscle degeneration and wasting leading to severe disability and eventually death in young males.

This most frequent disease in children starts in striated muscles. Progressively lost, dystrophic muscle is replaced with connective tissue and fat (Bianchi and Morandi, 2008; Wagner, 2008) (Figure 2-6). Consequently, the patient would experience muscle weakness including difficulties in standing, climbing stairs and walking. In some cases, disease will affect cardiac muscles leading to cardiomyopathy.

DMD is also associated with cognitive impairment and bone abnormalities. The latter two symptoms were initially considered to be the consequences of muscle weakness i.e. the lack of educational opportunities and asymmetrical strength distribution affecting the intellectual development and bone formation and function, respectively.

DMD is caused by mutations in the DMD gene encoding dystrophin (Ito et al., 2006). It is the largest gene in the human genome (Nowak and Davies, 2004). DMD patients lack dystrophin which is extremely important for human muscle function. Primary muscle weakness eventually leads to death due to the secondary effect of the disease such as respiratory failure related to functional loss of respiratory muscles and diaphragm or due to the cardiac failure. A definite diagnosis for DMD is the absence of dystrophin protein in muscle biopsy (Deconinck and Dan, 2007). According to Deconinck & Dan (2007), the pathological features of dystrophic muscle fibres were often observed in clusters where muscle necrosis was always found. Patients at an early age suffer from progressive loss of ambulation and skeletal deformities leading to severe disability developing long before death. There is no cure for the disease (Bianchi and Morandi, 2008; Blake et al., 2002) and the current treatment focuses on alleviating the symptoms and prolonging the patient's life. However, current research trials are actively looking at the potential of gene (Wagner, 2008; Wang, 2010) and myoblasts or stem cells therapy (Nowak and Davies, 2004).
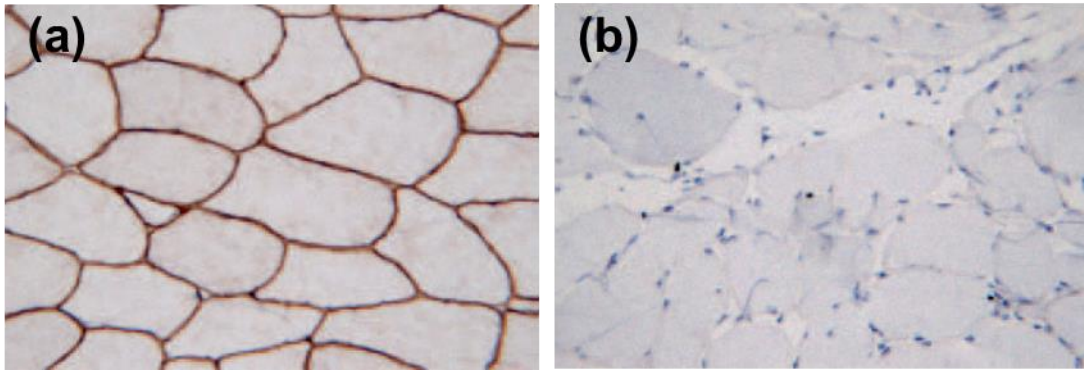
Figure 2-6 Comparison of (a) healthy and (b) *mdx* muscle tissues.
(a) Healthy muscle shows a normal sarcolemmal immunostaining pattern (b) *mdx* muscle tissues show the complete absence of sarcolemmal staining in muscle fibers which is a characteristic of DMD (Adapted from Davies and Nowak, 2006).

2.2.1 Clinical Progression of DMD

The clinical symptoms of DMD manifest at 3-5 years of age. DMD eventually leads to wheel-chair dependence at the age of 10 to 12 years. Symptoms associated with DMD are typically muscle degeneration that causes thin and weak thigh, tip-toeing, weak stomach muscles that cause the stomach to protrude, shoulders and arms held backward, swayback, weak buttock muscles, and thick calves due to fat tissue accumulations. Also, the patient will experience poor balance and awkward walking with difficulties in rising from a lie down position (Figure 2-7).

Patients with DMD have frequently been reported to have cognitive impairment. This occurs as a result of signaling abnormality and the most likely cause of these cognitive behavioural phenotypes is independent of the functional muscle impairment (Blake et al., 2002). A recent study on 3 to 16 year old children has shown a cumulative loss of dystrophin isoforms (Rasic et al., 2014). This has been identified to cause a greater risk in the reduction of intellectual ability among DMD males. This impaired cognitive performance in DMD patients is non-progressive, indicating its developmental origin. The precise pathological mechanisms underlying this abnormality are still poorly understood.
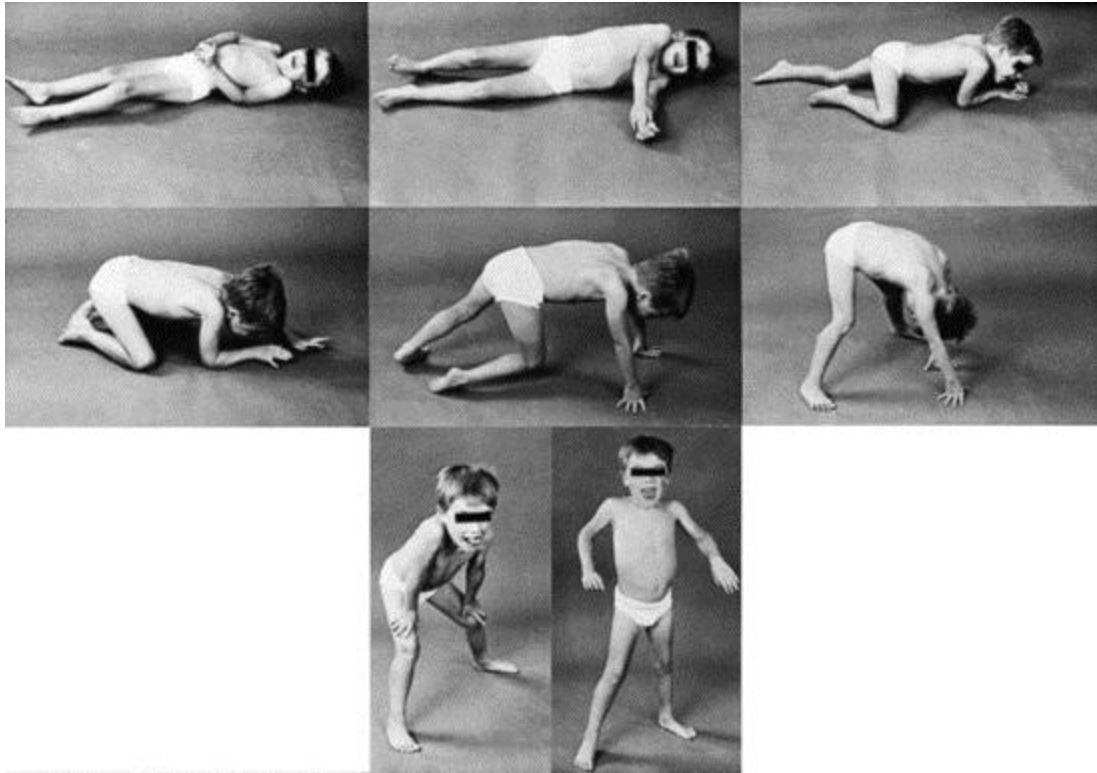
Figure 2-7 An illustration of Gowers' sign in a patient with Duchenne muscular dystrophy.
The figure shows a sequence of manoeuvres required to rise from the supine position (http://clinicalgate.com).

In addition, DMD patients are known to suffer a decline in bone mineral density. The old theory implied that patients are immobile and therefore less muscle activity attributed to the progressive muscle fibre degeneration and wasting causes the bone (Fritton et al., 2005; Lynch et al., 2010; Oppl et al., 2014). Bone adaptation to mechanical loads is known to be linked mainly to muscle activity, where the forces due to muscle contraction result in osteogenic simulation. Therefore, muscle wasting and immobility cause the bone loss, highlighting the importance of mechanical stimulation for bone tissue regulation. This fits with the impact of muscle loss on the dystrophic bone structure being more profound during later stages of the disease. However, more recent studies found that bone abnormalities occur prior to muscle loss e.g. already present in 4-week old dystrophic mouse bones (Nakagaki et al., 2011; Rufo et al., 2011). This could indicate that other, primary factors inherent to the disease are responsible (see below).

Considering the clinical features of DMD, fracture prevalence in this group has been studied by McDonald et al. (2002). About 40% of 378 males were found to have fractures, most commonly at the age of 8 to 11 years old and about 47% has lost mobility permanently because of such fractures. The study also estimated that 20-25% of boys (Bachrach, 2005) will experience long bone fractures. The key contributing factor is the reduced bone density (Blake et al., 2002; Nowak and Davies, 2004)

The main medication given to the child having DMD are glucocorticosteroids (deflazacort and prednisone) (Ay et al., 2009; Bianchi and Morandi, 2008; Bonifati et al., 2000; Wagner, 2008). These drugs prolong the ambulation period by a few months (Bianchi and Morandi, 2008; Bianchi et al., 2003). Earlier studies based on analysis after 2 year trial period, suggested that the earlier the drug is given to the child, the slower the progression of the disease (Bonifati et al., 2000). However, more recent studies indicate severe side effects associated with this treatment. Particularly relevant to this thesis, Bianchi & Morandi (2008) suggested that the status of bone of the patient should be obtained prior to steroid therapy being initiated because the side effects were found to particularly affect the bone, with bone density deteriorating rapidly, exacerbating the bone phenotype and contributing to the higher frequency of fractures in DMD patients (Wagner, 2008).

2.2.2 Structure and Functions of the Dystrophin gene and its products

Dystrophin is located at the intracellular side of muscle sarcolemma and is a key element of a membrane-spanning protein complex that connects the cytoskeleton to the basal lamina (McGreevy et al., 2015). Dystrophin is the largest known gene (Figure 2-8). It can be found predominantly in skeletal and cardiac muscles. The precise functions of dystrophin are still unclear although its absence in DMD resulting in the severe and multi-organ pathology shows its importance (Blake et al., 2002). The identification of mutations in the dystrophin gene as the cause of DMD led the way for the positional cloning of many other genes responsible for single gene disorders. Figure 2-8 shows the organisation of these promoters and the resulting proteins. Dystrophin can be organized into four separate regions based on sequence homologies and protein-binding capabilities. These are the actin-binding domain at the NH2 terminus, the central rod domain, the cysteine-rich domain, and

the COOH-terminal domain. The expression of the full-length dystrophin transcript is controlled by three independently regulated promoters. The brain (B), muscle (M) and Purkinje (P) promoters reflect the major sites of expression of this particular dystrophin. The B promoter drives expression primarily in cortical neurons and the hippocampus of the brain while the P promoter is expressed in the cerebellar Purkinje cells and also skeletal muscle. The M promoter results in high levels of expression in skeletal muscles and cardiomyocytes, and also at low levels in some glial cells in the brain. These three promoters are situated within a large genomic interval of 400 kb (Blake et al., 2002).
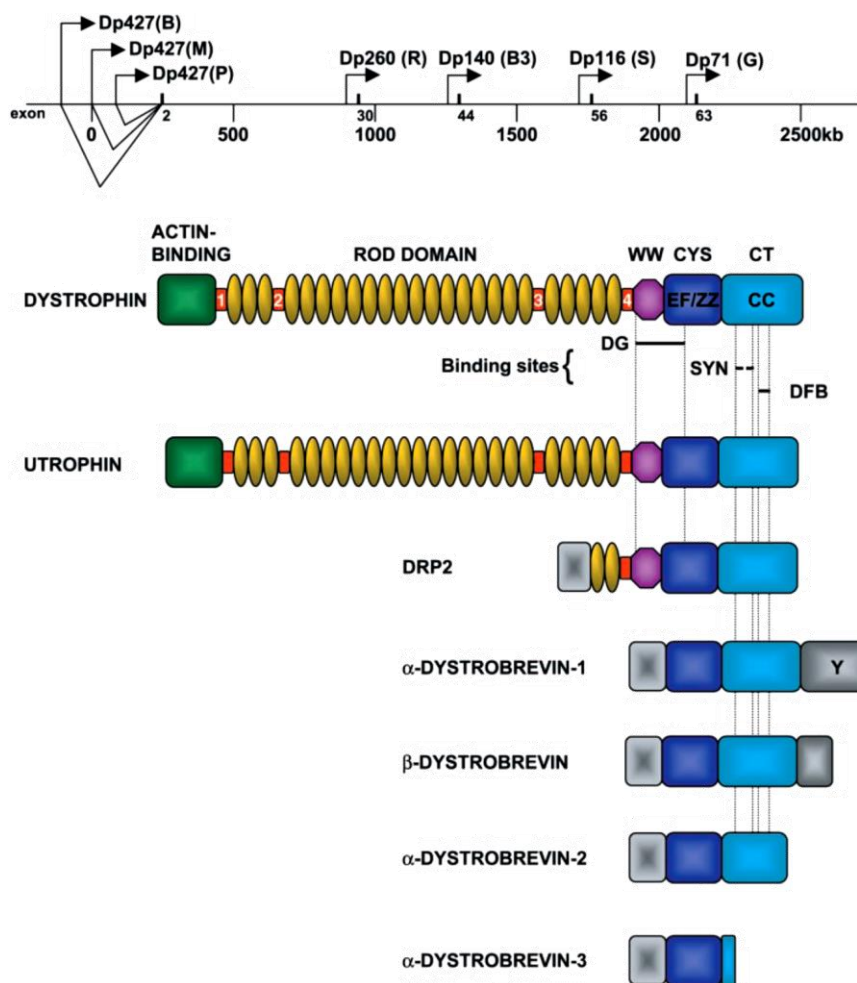
Figure 2-8 The DMD gene and proteins.
The DMD gene encompasses 2.5 Mb in the Xp21 locus and encodes 7 different protein isoforms. The full-length dystrophin transcripts are expressed in brain (B), muscle (M), and cerebellar Purkinje cells (P) and encode the 427-kDa proteins. The shorter isoforms are Dp260, Dp140, Dp116, and Dp71 kDa and show predominant expression in retina (R), brain (B3), and Schwann cells (S), respectively with the

smallest isoform (G) having generalised expression. The utrophin is an autosomal homologue of dystrophin with a similar structure but a different pattern of expression (Adapted from Blake et al. 2002).

Figure 2-9 shows the dystrophin anchors a complex of dystrophin-associated proteins including dystroglycans, sarcoglycans, and various combinations of α/β-dystrobrevins and syntrophins. It is responsible for interacting with the muscle cell cytoskeleton and connecting it with the proteins in the extracellular matrix (ECM) and other molecules to support the muscle cell membrane (sarcolemma) structure (summarised in Ervasti (2007)). The absence of muscle dystrophin causes disruption and reduction in dystrophin-associated proteins leading to costamere disorganization, sarcolemmal fragility causing excessive levels of calcium ions to enter the muscle cells causing muscle necrosis. Muscle death results in progressive muscle weakness and eventually is followed by fibrosis and fat replacement of the muscle tissue (Jiang et al., 2005; Klingler et al., 2012).
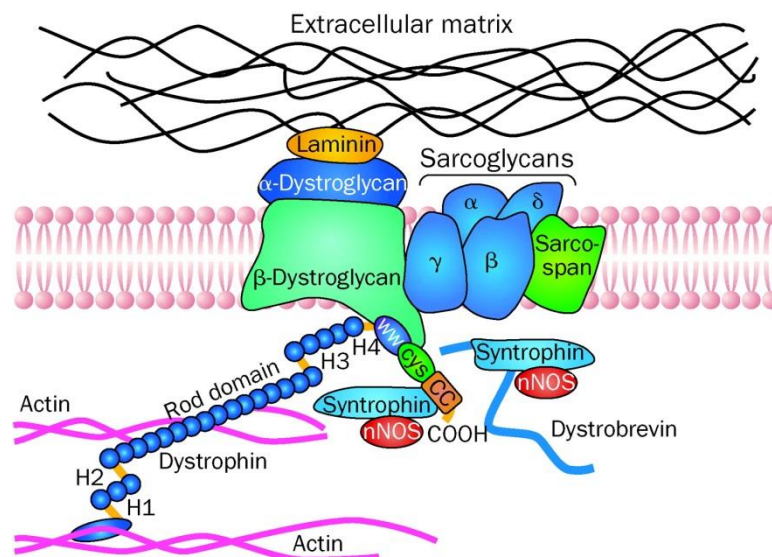
Figure 2-9 Structure of dystrophin-associated protein (DAP) complex in normal mouse skeletal muscle.
Dystrophin has a critical role in the maintenance of stability by creating a link between the contractile machinery in the cell and the extracellular matrix via the dystroglycan complex (Kapsa et al., 2003).

Regarding the cognitive impairment associated with DMD, Taylor et al. (2010) and Rasic et al. (2014) provided some evidence that mutations affecting Dp140 and Dp71/Dp40 expressed in the brain have been more frequently associated with more severe cognitive impairment. In general, based on standard intellectual assessment they found that the risk is increased as a result of the cumulative loss of central nervous system expressed dystrophin isoforms. Multiple lines of evidence point to an important role of dystrophin at central synapses and to its absence impacting on synaptic transmission (Knuesel et al., 2000; Moukhles and Carbonetto, 2001). More recent data show that the absence of dystrophin alters the spatio-temporal pattern of GABAergic synaptic transmission within the specific brain regions (Krasowska et al., 2014).

Another important non-muscle aspect of the pathology of particular significance for this thesis is low bone mineral density associated with DMD, which has been reported in human (Bianchi and Morandi, 2008; Bianchi et al., 2003; Rufo et al., 2011; Söderpalm et al., 2007) and dystrophic mouse bones (Nakagaki et al., 2011; Novotny et al., 2011; Rufo et al., 2011). In the human, the authors published information on bone markers in DMD patients where increased bone turnover, mainly in the form of bone resorption was confirmed. As a consequence, it can be expected that bone formation is elevated. This was in accordance with their finding of a decreased level of osteocalcin. In mice, these authors demonstrated that the DMD model mouse (*mdx*) presents with bone abnormalities at 3 weeks of age, which is too early for the bone disease process to be influenced by muscle wasting. Interestingly, analysis of biochemical and biomechanical properties showed the *mdx* femur having significantly lower bone tissue quality when compared with the healthy femur. They found that *mdx* femur showed the characteristic presentation of osteopenia at a time when muscle fiber degeneration was still not significant. They suggested that there are intrinsic factors that might be interact with the reduced mechanical stimuli in children with DMD and compromise the bone quality.

In the late stages of DMD progression, the impact of muscle loss on the dystrophic bone structure is evident. However, early bone abnormalities found prior to substantial muscle loss indicate that there may be other factors inherent to DMD, which also contribute to the loss of bone mass, bone mineral density, cellular,

molecular and mineral composition (Anderson et al., 1993; Bianchi and Morandi, 2008; Nakagaki et al., 2011). For example, studies by Anderson et al. (1993), Rufo et al. (2011) and Novotny et al. (2011) showed up to 50% loss in strength and stiffness in the *mdx* mouse model of DMD compared to those of the control, resulting in the development of micro-damage (Saito and Marumo, 2010) and bone fracture (Bianchi and Morandi, 2008).

Several scenarios have been envisaged on the mechanisms behind the DMD bone abnormality (Abou-Khalil et al., 2013; Bianchi et al., 2003; Rufo et al., 2011). DMD causes absence of dystrophin, which disrupts structural scaffolds involving dystrophin-associated proteins and loss of anchoring for specific signalling proteins (Blake et al., 2002). Therefore, the absence of dystrophin could be directly responsible for bone structure alterations. However, there is no data on dystrophin being expressed in osteoblasts or osteoclasts. On the other hand, dystrophic muscle degeneration is associated with chronic sterile inflammation, and Abou-Khalil et al. (2013) demonstrated that chronic inflammation contributes to the dystrophic bone damage. In DMD patients, prolonged corticosteroid treatment can further exacerbate this abnormality (Bianchi et al., 2003; Söderpalm et al., 2007).

2.3 Animal models of DMD

Experiments in animal models have allowed the roles of specific genes *in-vivo* to be studied and provided useful information on the disease mechanisms (Allamand and Campbell, 2000) and on the development of potential treatment strategies for DMD (Kornegay et al., 2012; McGreevy et al., 2015).

Particularly effective have been gene knockouts or the introduction of a pathogenic (mutant) genes in mice. For DMD, there are a number of animal models that are widely used in research. These include fish (Bassett and Currie, 2010; Kawahara et al., 2014), mouse (Nakagaki and Camilli, 2012; Nakagaki et al., 2011; Rufo et al., 2011) and dogs (Kornegay et al., 2012). On average, the protein-coding regions of the mouse and human genomes are 85% identical; some genes are 99% identical while others are only 60% identical. Most recently, Selsby and co-workers (2015) have studied the potential of the porcine animal model for DMD. They identified and completed the initial characterization of a natural porcine model of dystrophin

insufficiency. Muscles from these animals display characteristic focal necrosis concomitant with decreased abundance and localization of dystrophin-glycoprotein complex components. These pigs recapitulate many of the cardinal features of muscular dystrophy, have elevated serum creatine kinase activity, and preliminarily appear to display altered locomotion. They also suffer from sudden death preceded by EKG abnormalities. Pig dystrophinopathy models could allow refinement of dosing strategies in human-sized animals in preparation for clinical trials.

2.3.1 Dystrophin-deficient mouse model (*mdx*)

Dystrophin-deficient mouse (*mdx*) was developed in 1984 (Bulfield et al., 1984) and is still the most widely used animal model for DMD. It is so because the *mdx* has a rapid disease onset (i.e. around 3-4 weeks of age), short maturation period and are less expensive than other models. The *mdx* mouse is therefore well-established as a pre-clinical model for DMD (Montgomery et al., 2005). Although there are a few distinctions with the human pathological process, the X-linked recessive mutation in the dystrophin gene of the *mdx* mouse resembles that seen in boys with DMD (Lovering et al., 2005). It is also a valuable tool in the development of therapeutic strategies (Allamand and Campbell, 2000). Up until the age of 1-week, muscles appear normal and start to degenerate and regenerate in cycles of around 3 to 4-weeks of age (Turk et al., 2005). From 4 month the degeneration process in *mdx* leg muscles becomes less severe and regeneration starts to dominate. However, the pathology progresses, albeit at a much lower rate while it is present continuously in the diaphragm. For average life span, female wild-type mice lived 27.0 months and male wild-type mice lived 26.5 months. In contrast, the average life span for female *mdx* mice was 22.5 months and for male *mdx* mice 21.5 months (Chamberlain et al., 2007; Grounds et al., 2008).

mdx presents with the typical increased levels of muscle creatinine kinase (MCK) and pyruvate kinase in the serum, accompanied by histological indicators of skeletal muscle degeneration and regeneration. The mouse muscle cannot withstand mechanical forces due to compromised function of the dystrophin associated protein complex (DAPC) (Whitmore and Morgan, 2014). Whitmore and colleagues (2014) suggested that the different parts of the complex play different roles in the regulation of muscle function. Despite the same complex being functionally compromised there

are different degrees of severity, affecting different tissues, depending on which part of the complex is inactivated.

The *mdx* mouse model has been used to study DMD pathogenesis (Montgomery et al., 2005; Nakagaki et al., 2011) and to develop its treatment (Allamand and Campbell, 2000; Gussoni et al., 1999; Wang, 2010). At an early stage, *mdx* mouse pathology was found to parallel the severity of human DMD (Nowak and Davies, 2004; Wagner, 2008). Although the *mdx* mouse does not show progressive muscle fibrosis in leg muscles, as seen in human DMD (Anderson et al., 1993), recent studies revealed that it has a pro-fibrotic phenotype (Sinadinos et al., 2015). Moreover, the main advantage of *mdx* and the reason these mice have been used in most of DMD studies, is the ability of manipulating the mouse genome for functional experiments. Nakagaki et al. (2012) found that there is a change in muscle activities of *mdx* mice, which lead to loss of muscle function at 21 days of age, i.e.during the pre-necrotic stage. At the age of 4 weeks, Anderson et al. (1993) and Nakagaki et al. (2011) reported the muscle degeneration to be more severe and also accompanied by intense muscle inflammation.

2.3.2 P2RX7 Receptor Knockout Model

In the present study, the role of the P2RX7 purinergic receptor in the pathogenesis of DMD will be investigated. Purinergic receptors respond to extracellular ATP and lots of ATP is released from damaged muscles (inflammatory condition). P2RX7 is one member of the large family of P2 receptors and it is different from the others in many ways. As an example, its activation is well known to induce cellular apoptosis (Agrawal and Gartland, 2015). In response to prolonged, high ATP stimulation, P2RX7 can exhibit wider permeation to molecules that may be associated with cell death by apoptosis or necrosis. P2RX7 has been shown to induce autophagy in various cell types and its high level of activation is cytotoxic to cells whilst the low level P2RX7 stimulation can provide metabolic advantage which is the ability to adapt to conditions of limited nutrient supply (Amoroso et al., 2012; Young et al., 2015). Importantly, P2RX7 receptor is also associated with the modulation of bone formation and function. ATP is released from osteoblasts upon mechanical and nucleotide stimulation and mediates paracrine signalling to neighbouring cells via P2RX7 activation. P2RX7 expression in osteoblasts is a differentiation-dependent

expression and the receptor is mainly expressed in mature bone forming osteoblasts. In osteoclasts, ATP release is associated with P2RX7 activation, but the exact mechanism has not yet been determined (Kvist et al., 2014).

DMD gene mutations are associated with P2RX7 purinoceptor up-regulation, which leads to the death of both human DMD (Ferrari et al., 1994) and *mdx* cells (Yeung et al., 2006; Young et al., 2012). P2RX7 activation in *mdx* muscles triggers a specific mechanism of autophagic cell death (Young et al., 2015). Recent work showed that this receptor is a good target for pharmacological treatment of DMD, as its genetic ablation (knockout) reduced both muscle loss and inflammation (Sinadinos et al., 2015). P2RX7 is expressed in both osteoblasts and osteoclasts, but it appears to have different roles in bone physiology and in disease states. If P2RX7 is abnormally active in dystrophic bones, its absence might improve the bone properties. On the other hand, activation of P2RX7 receptor has been linked primarily to osteoclast functions (Agrawal and Gartland, 2015; Agrawal et al., 2003; Gartland, 2012) hence its ablation could have a negative impact on the bone.

Specific animal models of DMD (*mdx)* have been created in which the P2RX7 receptor has been genetically disrupted (*mdx*/P2X7$^{-/-}$, double knockout). Using the *mdx* (Bulfield et al., 1984) and the P2RX7 receptor knockout mice (Solle et al., 2001). The genetically disrupted P2RX7 receptor mouse generated by Solle et al.(2001) has been explored by Ke et al. (2003) to assess the receptor involvement in bone development and remodelling. They found that the P2RX7 receptor is a good target in management of skeletal disorders. The receptor was found in both osteoblasts and osteoclasts of wild-type (WT) but not in the knockout mice. This model has shown a direct function of P2RX7 in bone formation: The study found the reduction of total and cortical bone content as well as of the periosteal circumference occurring in the femur while there was a reduction in periosteal bone formation and excessive increment in trabecular bone resorption in tibia of the P2RX7 knockout mice.

2.4 Evaluation of Bone Microstructure using Micro-Computed Tomography (µCT)

2.4.1 Basic Concepts

Micro-Computed Tomography (µCT) has the same basic principles as CT for medical diagnosis currently available in most hospitals. The main difference between them is the higher resolution obtained from µCT, which can reach between 50 microns (Davis and Wong, 1996; Paulus et al., 2000) and 50 nm (Bruker µCT) (Stock, 2009). µCT is considered more cost-effective than Magnetic Resonance Microscopy (MRM) and it is preferable to others in terms of high resolution and signal-to-noise ratio (SNR) in imaging implants and mineralized tissues (Krug, Burghardt , Majumdar, 2011). Most µCT systems have high resolution flat panel and small focal spot size that allow high resolution imaging of small animals. In µCT the same image reconstruction techniques as in clinical-scale CT are applied. CT systems using fan-beam geometries apply fan-beam reconstructions based on filtered back-projection algorithms originated from the early days of clinical CTs. The recently introduced flat panel based µCT employs variants of the Feldkamp-David-Kress (FDK) algorithm for cone-beam reconstruction. Both reconstruction techniques need to be adapted to the specific small animal scanner geometry (Bartling et al., 2007). Currently, there is an increasing interest in animal research studies using µCT, as these animal models may lead to clinical applications (Chappard et al., 2005; Holdsworth and Thornton, 2002; Paulus et al., 2000).

The past decade has seen the rapid development of µCT in small animal imaging (Paulus et al., 2000; Schambach et al., 2010). µCT has now become the gold standard for the evaluation of bone morphology and other small animals (Martı´n-Badosa et al., 2003). µCT has been used to evaluate morphology measurements in animal (Bonnet et al., 2009; Waarsing et al., 2004) and human tissues (Müller et al., 1998; Thomsen et al., 2005). This increasing demand in utilising µCT for research purposes has demonstrated that the scanner capability of providing high spatial resolution in high contrast structures (Jiang et al., 2000). In addition, its ability to image the internal structure without destroying the original specimens is valued and allows further investigation such as histomorphometric analysis (Bischoff et al., 2011). The acquired three-dimensional (3D) data sets have also been used as inputs

for finite element (FE) analysis which can be used to estimate the bone mechanical properties virtually (Brassey et al., 2012; Oftadeh et al., 2015; Rietbergen et al., 1996; Silva et al., 2005).

The principles of CT implies taking x-ray projection images of an object from many angles around the object, and mathematically converting this set images into a stack of cross-sectional image slices, which represents a 3D image. These projection images are taken incrementally over a total rotation of either 180° or 360°. While the individual projection x-ray images are 2D images, the rotation of the imaged sample relative to the x-ray source and camera allows the precise 3D location of the scanned objects to be calculated (provided the objects are within the camera field of view at all angles of rotation) (Figure 2-10) (Bruker microCT, n.d.).
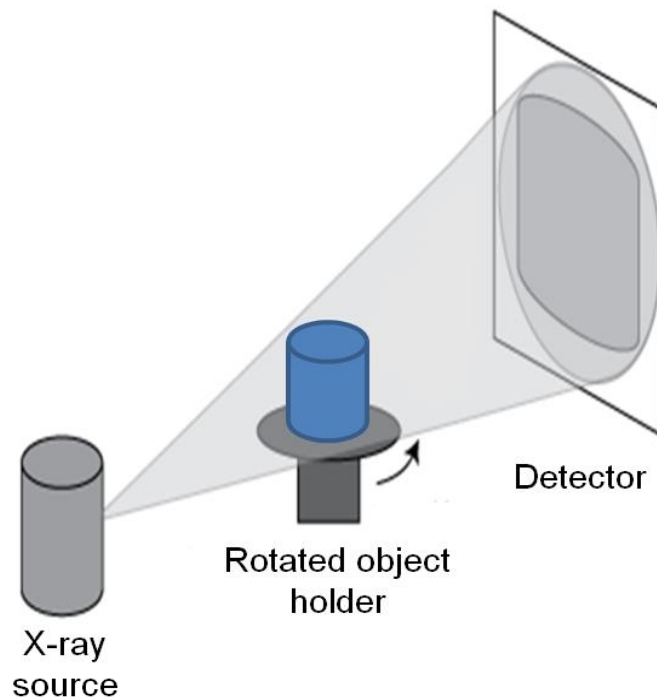
Figure 2-10 An illustration of a µCT scanner geometry.
A cone beam x-ray projection to enable volume scanning of the object. The object is located between the x-ray source and the detector, and rotates on the holder during scanning.

High spatial resolution is an important feature in µCT imaging. Spatial resolution describes how far two features of the object need to be separated to be distinguishable in the measured image (Rueckel et al., 2014). µCT provides higher

spatial resolution than that of current clinical CT. µCT can provide a resolution of below 100 µm for small animal imaging, (Bartling et al., 2007; Stock, 2009). The imaging resolution is determined largely by the size and number of detector elements, the size of the X-ray focal spot, and the source-object-detector (SOD) distances (Bartling et al., 2007; Verdelis et al., 2011).

For example, a short SOD would place the animal closer to the x-ray source than the detector, thereby be magnified by the factor of M= (ODD/SOD), improving the spatial resolution. However, the Field of View (FOV) will be compromised. With the advent of large flat-panel detector, higher magnification factors will be possible. This is because active detector area will increase significantly. Short SOD, however, requires micro-focus x-ray tubes since larger focal spot size will cause significant image blurring (penumbral blurring) (Bartling et al., 2007) (Figure 2-11). Focal spot size is an important factor to determine image resolution and quality of the x-ray image. Focal spot is the actual area on the target where the electrons transfer their energy to the target atoms where the X-rays are generated. Typical focal spot size for micro-focus CT is 3 µm.
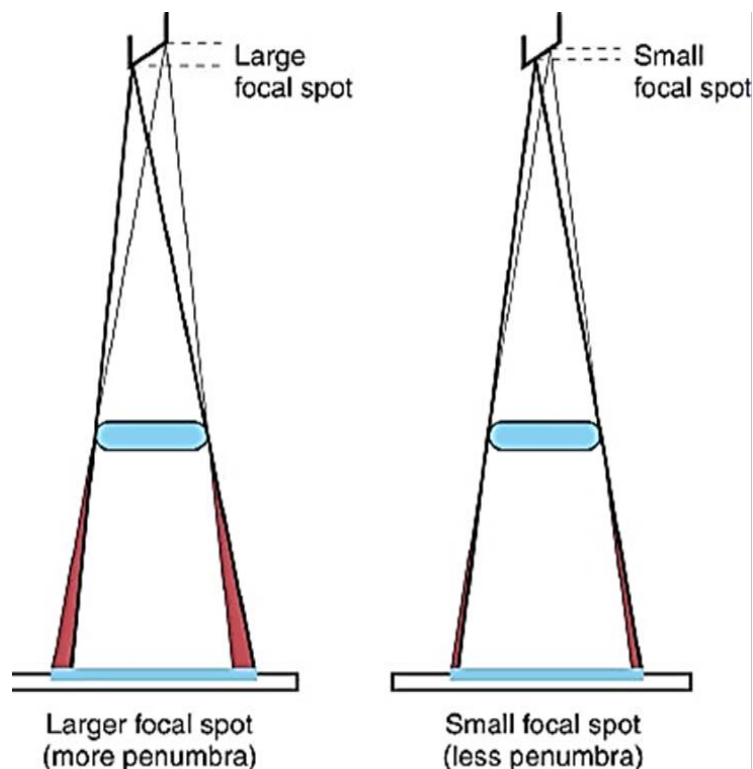
Figure 2-11 Focal spot size.
Large focal spot size (left) increase geometric blurring which is called penumbra whilst small focal spot size (right) improves in-plane resolution, where the ability to

detect details is improved enabling geometric or projection magnification without penumbra.

Before the advent of μCT, histology often used where the object is cut into thin slices and examined under a light microscope, a time-consuming, labour-intensive process. The conventional x-ray system produces 2D shadow images of the internal structures; however, the depth information is overlapped or superimposed. Therefore, μCT provides an alternative technique to produce image of the object non-invasively and less time consuming.

Scanner Geometry

There are four types of scanner geometry system, as discussed in Stock (2009): (1) pencil, (2) fan, (3) parallel, and (4) cone beam geometries. μCT employs the cone beam geometry. The geometry consists of a micro-focus x-ray tube source that is suitable for volumetric scanning. When x-rays diverge and travel from the tube source, they pass through the object and are detected by a high resolution detector. Specifically in this geometry, each of the detector rows receives the information from more than one slice of the object, except for the middle row. This effect becomes greater when the x-rays pass through a rotational axis object. In addition, short scanner geometries, where the source-to-object distance (SOD) is smaller than object-to-detector distance (ODD), will bring the object close to the source and high spatial resolution will be produced. According to Bartling et al (2007) and Stock (2009), a micro-focus x-ray tube with a small focal spot size will reduce significant image blurring (penumbral blurring) which degrades resolution.

X-ray Source

There are three criteria for a micro-focus x-ray source: (1) Small focal spot size; (2) a high photon flux, ϕ and (3) a suitable range of x-ray energy. The small focal spot size produces high spatial resolution which eliminates the negative influence of image blurring. The emitted x-ray photon flux, ϕ, is roughly proportional to the product of the x-ray anode current (I) and the square of the tube voltage (V) and the tube power is $P = V \cdot I$, the available x-ray flux is limited by the size of the focal spot, which can only absorb a certain amount of heat (anode heating). The maximum

power that an x-ray tube can emit thus also depends on the heat capacity of the anode material and the tube technique used. Tubes with rotating anode support much higher output than tubes with stationary anodes since heat is evenly distributed along the focal spot trajectory.

High x-ray flux is desirable for small animal CT imaging to achieve high temporal resolution and short scan times: if the photon flux is high enough, sufficient x-ray photons reach the detector and can be collected in short times for each projection. A sufficient amount of x-ray photons is required to limit image noise and allow good low-contrast spatial resolution (Bartling et al., 2007).

2.4.2 Image Acquisition

In the µCT system, the animal is positioned on a rotating stage and sandwiched between source and detector. The animal rotates on a single axis over 360° during scanning, allowing the attenuated x-rays to be detected on a 2D planar array. A series of 2D slices are reconstructed to create 3D reconstruction by means of filtered back projection. This projection has become a standard algorithm to filter the blurred reconstruction across regions (Stock, 2009).

In x-ray acquisition, the image contains information about the intensity reduction inside the 3D object. This is because the X-ray absorption is corresponding to exponential law. In order to achieve the best low-contrast spatial resolution in small animal CT imaging, a range of tube voltages should be considered to select the appropriate x-ray energies. For higher x-ray energies the energy-dependent absorption coefficient µ(E) is small and low-contrast spatial resolution is limited due to the small number of x-ray photons absorbed in the animal. If x-ray energy is low and thus µ(E) large, most photons are absorbed in the animal and the contrast resolution is limited by the small amount of x-ray photons reaching the detector (Bartling et al., 2007).

There are several artefacts as a result of x-ray attenuation, such as geometrical blurring, streak-like artefact due to reconstruction and beam hardening. The most common artefact relevant to bone density measurement is beam hardening, its occurrence can be more than 36.2% (Meganck et al., 2009). Beam hardening is

caused by a preferential absorption of low energy photons. It can be corrected either during image acquisition or image reconstruction (software or added filter).

2.4.3 Image Processing

The next step after image acquisition is processing the stack of images including filtration and segmentation. The function of each type of filter in the field of bone imaging has to be reported as suggested in Bouxsein et al. (2010). During image reconstruction, noise reduction is carried out as part of the procedure to maintain sharp contrast between bone and marrow. The most commonly used filters are Gaussian filter and median filter. A Gaussian filter is easy to use and fast for large dataset. Both filters can provide good results, although minimum filtering is required to avoid degrading the image data. One has to bear in mind that reducing the noise will simultaneously reduce the image details or signal-to-noise (SNR) ratio. Different filter materials will have different ability to reduce beam hardening artefacts by affecting the x-ray spectrum. X-ray beam filtration is known to affect the signal to noise ratio and the contrast to noise ratio, therefore, careful selection of a filter is important, as given in Meganck et al. (2009) and Bouxsein et al. (2010).

Segmentation is one of the crucial parts in the evaluation of morphological parameters of the bone. The segmentation process is defined as separation of bone and non-bone based on the grey scale level for subsequent quantitative analysis. Accurate segmentation is to ensure that errors due to artefacts are minimised in the determination of morphometric parameters (Bouxsein et al. 2010). There are several techniques for segmentation, the common and simplest technique is to use threshold technique. Previous studies have proposed techniques on threshold selection relative to image histogram (Weszka and Rosenfeld, 1978). They established two criteria on threshold evaluation: discrepancy and error measures as well as busyness measures. A discrepancy measure was based on the difference between the original and the smoothed pictures whilst a busyness or roughness measure was computed on the smoothed picture. Both methods produced good results on segmented images. An important issue in segmentation relates to the contouring method employed to define the area in each slice to be included for segmentation and subsequent morphology quantifications (Bouxsein et al. 2010). The easiest method is to create a constant circular or rectangular area. However, this method

does not allow separation of cortical and trabecular bone as well as the background. More precise contouring for specific cortical and trabecular bone regions therefore is required, and this may be achieved manually on a slice-by-slice basis or using automated algorithms (Buie et al., 2007). Alternatively, semi-automated segmentation (Janc et al., 2013) and global thresholding (Kohler et al., 2005) methods may be used to generate more reliable bone morphometric data. There are several approaches in delineating the trabecular region, such as a uniform ROI, an irregular anatomic contour adjacent to the endocortical surface, or an irregular anatomic contour a few pixels away from the endocortical boundary (Figure 2-12).
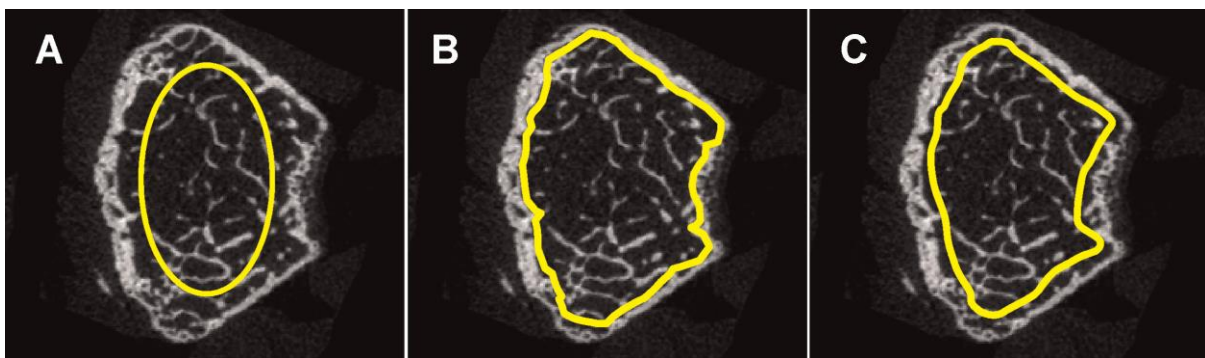
Figure 2-12 Contouring methods used to delineate the trabecular bone from the cortical bone. Three approaches: (A) A regular, uniformly shaped region of interest; (B) an irregular, anatomic region of interest adjacent to the endocortical boundary, drawn using an automated algorithm (Buie et al., 2007) and (C) an irregular, anatomic region of interest drawn manually a few voxels away from the endocortical surface (Bouxsein et al., 2010).

A built-in thresholder can use the stack histogram (frequency distribution plots) and apply several different auto threshold algorithms. The automatic threshold calculates a threshold without any human judgment involved. Therefore it may offer an advantage of reducing human bias in the segmentation step. The preference of a method or threshold algorithm greatly depends on the problem to be solved.

2.4.4 Image Analysis

Reliable freeware has been used to analyse bone parameters. ImageJ is a public domain image processing program that has flexible plugins and functions for bone morphological measurement. The plugin is called BoneJ. The parameters for image analysis such as volume fraction and bone thickness and other parameters are recommended in the guidelines of Bouxsein et al (2010). BoneJ has provided the most powerful image processing program in the public domain to analyse bones (Doube et al., 2010).

2.4.5 Image Segmentation

Following µCT scanning and data acquisition, the µCT data sets undergo segmentation, an important step in image analysis (Bouxsein et al., 2010). Segmentation is used to identify which pixels in the image belong to one or several regions of interests (Mateos-Perez and Pascau, 2013). A recent study has implemented a modified segmentation method by Buie et al. (2007) using Matlab (Cervinka et al., 2015). Buie et al (2007) proposed a dual threshold technique to segment the bone regions by utilizing the C+ Visualization Toolkit. Firstly, the periosteal surface is produced by thresholding the reference image, followed by applying morphological closing operations and connective filtering. Next, the reference image is thresholded again and combined with the non-bone region mask to get marrow cavities where subsequent steps eliminate the trabeculae. The output of the two steps is combined where masks of trabecular, cortical and non-bone region are created. However, Cervinka et al (2015) pointed out that this method fails to remove larger cortical pores. There are alternative methods developed as in-house software algorithms (Janc et al., 2013; Liu et al., 2009).

To be accurate in segmenting the bone, it is important to compare the processed images with the reference image. This ensures that the processed images are a good representation of the actual structures. Previous studies segmented the cortical and trabecular bones using the threshold method determined from the attenuation histogram of the volume of interest (VOI) (Microview Software v.2.2, GE Healthcare). By using visual inspection, they correlated the threshold value with the grey scale

image of the cortical bone and with the masked bone volume of the trabecular bone (Monir et al., 2010).

IsoData algorithm is a default automatic thresholding algorithm in ImageJ. The algorithm used is based on operator judgement whether the ROI is well segmented. The algorithm works by dividing the image into object and background by taking an initial threshold, then the averages of the pixels at or below the threshold and pixels above are computed. The averages of those two values are computed, the threshold is incremented and the process is repeated until the threshold is larger than the composite average. Threshold= (average background + average objects)/2.

In this work, a slice-by-slice hand contouring technique was applied to separate trabecular bone over cortical bone and subsequently segmented using default IsoData algorithm. This technique is the gold standard and has been used to validate other proposed methods, for example, the dual-threshold method (Buie et al., 2007). Automated software can be used to separate the trabecular bone from cortical bone, however, some bone sites, such as close to the growth plate or in vertebrae, the cortical bone is thin, perforated and poorly defined, so that automated methods are limited in application. Manual VOI delineation has the advantage of providing quality control for the scanned datasets, and letting the analyst actually look at the imaged bone structures and gain a visual impression of the experimental outcome (*Analysis of bone by micro-CT General information*, n.d.). The semi-automated slice-by-slice hand contouring and default IsoData algorithm technique described in Section 3.4.3 was used in this study to separate the trabecular and cortical bone from the background.

2.4.6 ImageJ and BoneJ

Image processing software commonly comes with the scanning hardware. The software can be costly and its functionality inflexible (Doube et al., 2010). Furthermore, the method or algorithm of the software is not detailed in most of the literature (Baiker et al., 2012; Verdelis et al., 2011). ImageJ was developed as an open source plugin. It can be operated using computer hardware remote from the scanning machine, regardless of the specifications except for Java program. It has been extensively used for image processing and analysis of various image formats.

BoneJ is one of the ImageJ plugins specifically developed for bone measurements. It has features and standard measurements for bone image analysis. The algorithms in the plugin were validated by analysing image data from 3D µCT, CT and synchrotron µCT. Doube et al. (2010) described the philosophy and validation of BoneJ, and illustrated its applicational scenarios. Algorithms in BoneJ were validated by running them on test data and comparing computed results to expected results. Test data included synthetic images, images of real objects and mathematically defined clouds of points (Fit Sphere and Fit Ellipsoid), all with known geometry.

Most recent studies have shown the validity of BoneJ plugin in the determination of the common trabecular bone parameters such as Bone Volume Fraction (BV/TV), Trabecular Thickness (Tb.Th), and Trabecular Space (Tb.Sp) (Collins et al., 2015; Doube et al., 2011; Hsu et al., 2016; Macintosh et al., 2013; Salmon et al., 2015). BoneJ is also capable of analysing human muscle as seen in Frank-Wilson et al (2015). The applications of the software are further utilised to examine the differences in different species of animals (Doube et al., 2011). Furthermore, BoneJ is useful to display bone thickness as a heat map which is easy to understand. For example, the osteoarthritic trabeculae are thicker and better connected than the osteoporotic elements (Abel et al. 2013).

In addition to the capability of BoneJ in quantifying the morphological properties of the bone, it is also able to quantify geometric properties, for example, second moment of area (I) (Collins et al., 2015). BoneJ has been used to calculate the diaphyseal cross-section geometry properties of humeral, femoral and tibial bones (Macintosh et al., 2013). Further, BoneJ has been used to calculate the 3D moment of inertia of feline limb bones (Doube et al., 2009).

2.5 Quantitative morphological properties of bone.

Bone morphological properties have been studied by a numerous researchers to investigate pathophysiological diseases and the effects of treatments, particularly in mouse bones. Critical morphological parameters have been identified quantitatively to assess bone microarchitecture changes across studies, as described in Section 2.5.1 and 2.5.2 (Bouxsein et al., 2010). The changes due to bone diseases and treatments can be evaluated quantitatively rather than qualitatively because bone

remodel at a rate of 10% a year for human adult whilst it is rare for mouse. Because bone microarchitecture has a major role in determining bone quality and strength, μCT has been utilised as a non-invasive method for evaluation of 3D bone geometry, volumetric bone density, microarchitecture and properties of the bone matrix (Brandi, 2009). Bouxsein et al. (2010) has produced practical guidelines to evaluate bone microarchitecture in rodents using μCT. The guidelines include the approaches to image acquisition, image evaluation, and reporting the findings. Bouxsein et al. (2010) asserted that four parameters as the minimal set of variables that should be reported when describing trabecular bone morphology (i.e., BV/TV, Tb.Th, Tb.Sp, and Tb.N) and cortical bone morphology (i.e., Tt.Ar, Ct.Ar, Ct.Th, and Cr.Ar/Tt.Ar).

Using μCT, the bone morphology of different mouse strains can be quantified for different parts of the mouse skeletal system (Alexander et al., 2001; Hsu et al., 2016; Kohler et al., 2005; Turner et al., 2001; Zhang et al., 2015). Microstructural properties, such as trabecular bone volume fraction (BV/TV) and bone thickness, are the common parameters in evaluating bone microstructure. They have been shown to change under the influence of genetic factors (Boutroy et al., 2005; Turner et al., 2001).

The well recognised clinical consequences of DMD bone phenotypes are bone mineral density deficiency (Bianchi et al., 2003; Morgenroth et al., 2012; Rufo et al., 2011; Söderpalm et al., 2007) and increased bone fracture incidence (McDonald et al., 2002; Pouwels et al., 2013; Vestergaard et al., 2001). Hence, a comprehensive approach to investigate the material and structural properties of bone is required to better understand the bone phenotype in DMD.

2.5.1 Trabecular bone morphometry

Bone Volume Fraction
Bone volume fraction (BV/TV) is the ratio of mineralised bone volume to total of bone with marrow space volume (Equation 2-1)

$$\text{Volume fraction} = \frac{\text{Bone volume}}{\text{Bone volume} + \text{Marrow space volume}} \qquad \text{2-1}$$

Volume fraction is one of the most widely reported to determine the amount of mineralised tissue. In a study to determine the treatment efficacy, bone volume

fraction represents the net response of the osteoblasts for bone formation and osteoclasts for resorption. Bone volume fraction does not provide information on the bone microstructure; therefore mean trabecular thickness and mean trabecular spacing were introduced (Boskey, 2001). Various indicators can be used to describe trabecular and cortical bone microarchitecture. Other related parameters are listed in Bouxsein et al. (2010). A summary of morphometric parameters for cortical and trabecular bones of healthy and *mdx* mice reported in the literature is given in Table 2.2.

Trabecular thickness (Tb.Th) and Spacing (Tb.Sp).
The BoneJ algorithm calculates the thickness of the trabecular bone struts in the region of interest. It calculates the diameter of the maximum sphere that fits within the structure at every point in the ROI (Figure 2-13). A method by Hildebrand and Rüegsegger (1997) was implemented by BoneJ. This method used the volume-based local thickness to accommodate the anisotropic properties of the bone. This method has overcome the limitations of surface-based methods which overestimate arbitrary and irregular structures. Moreover, the plugin also provides a thickness map with colour gradients for morphological assessments (Abel et al., 2013; Doube et al., 2010).
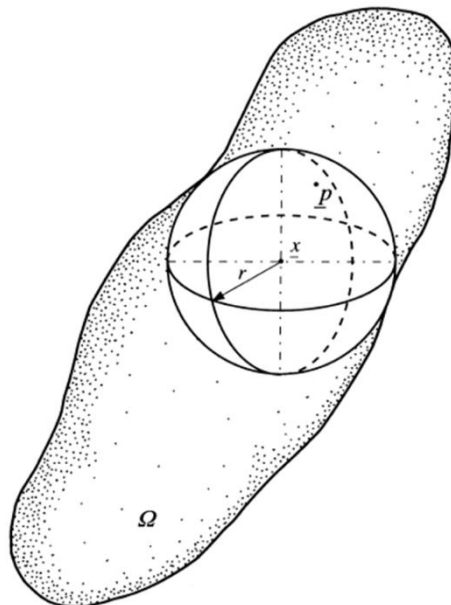
Figure 2-13 An example of local thickness.
Local thickness, T(p), of a structure, Ω, determined by fitting maximal spheres to the structure (Hildebrand and Rüegsegger, 1997).

2.5.2 Cortical bone morphometry

Bouxsein et al. (2010) asserted that at least four parameters (Tt.Ar, Ct.Ar, Ct.Ar/Tt.Ar, Ct.Th) must be used in describing cortical bone morphology. Therefore, these indicators were used in this study for cortical bone assessment. These parameters allow comparison across studies when different sized volumes of interest are scanned.

Total cross-sectional area (Tt.Ar) and cortical bone area (Ct.Ar)

According to Bouxsein et al. (2010), to compute average cross-sectional area measurements, the volume of interest (ie, a cylinder) is divided by the number of slices and voxel height or slice thickness. For total cross-sectional area, Tt.Ar =Tt.V /(no. of slices × voxel height) and cortical bone area , Ct.Ar = Ct.V/ (no. of slices × slice thickness). The unit is mm^2. These measurements were used to obtain accurate internal and external diameter measures for calculating the second moment of area (SMA) at the point of failure for bone structural evaluation. Tt.Ar characterises the resistance to axial compression and tension. Ct.Ar is a separate measurement for each tranverse slice section (AnalyzeDirect, 2014). In the present study, the 'Slice geometry' plugin in BoneJ was used. It calculates the cortical bone parameters for each transverse slice section and the cross-sectional geometric properties of shapes (Figure 2-14). The parameters extracted from the plugin are cross-sectional area (or cortical area), centroid, mean density, second moment of area, section modulus and local thickness (2D and 3D). The input image should be in 8-bit or 16-bit stack and the measurement can be limited to rectangular ROI.
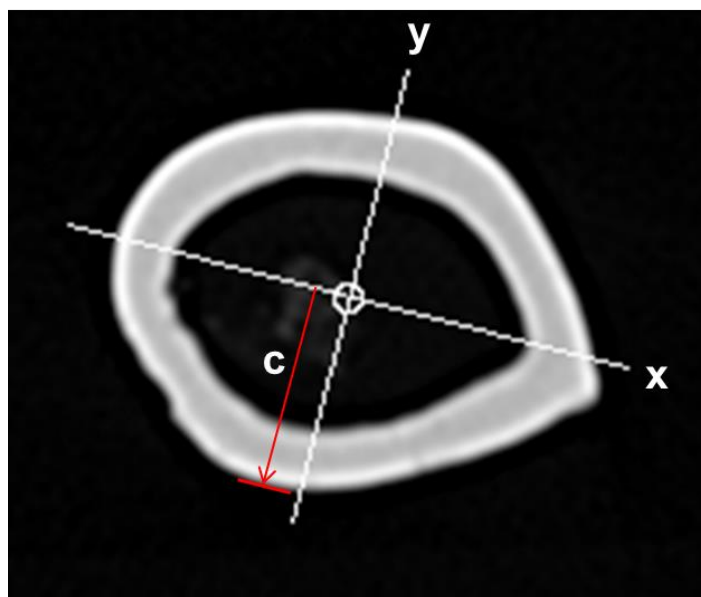
Figure 2-14 3D annotation displays the stack, principal axes and centroids. Cortical bone parameters were calculated based on the directions defined. Slice geometry is used to calculate the cross-sectional geometric properties of shapes for all slices in a stack of images.

Cortical bone area fraction (Ct.Ar/Tt.Ar) and cortical bone thickness (Ct.Th)

Ct.Ar/Tt.Ar is the ratio of cortical bone area to total cross-sectional area within a given volume of interest. Ct.Th is the average thickness of the cortex in a stack of images. The 'Thickness' plugin in BoneJ as mentioned above, defines the thickness at a point as the diameter of the greatest sphere that fits within the structure and which contains the point. The plugin calculates the mean and standard deviation of the volume of interest. Table 2-2 shows a comparison of morphometric parameters for cortical and trabecular bones of healthy and *mdx* mice from the previous studies. The authors reported different bone parameters to compare the bone phenotypes and they were using limited number of samples. Although there are differences in mice age, weight and bone parts, the authors showed similar pattern of significantly higher cortical and trabecular bone properties in WT compared to those of *mdx* mice.

Table 2-2 A comparison of morphometric parameters for cortical and trabecular bones of healthy and *mdx* mice from the literature.

Reference	Type of bone	Cortical			Trabecular		
		Tt.Ar (mm^2)	Cr.Th (mm)	Cr.Ar (mm^2)	BV/TV	Tb.Th (mm)	Tb.Sp (mm)
Nakagaki et al. (2011)	3-weeks mice femur	WT: 0.812±0.11 mdx: 0.615±0.09	WT: 0.065± 0.004 *mdx*: 0.037± 0.005	WT: 0.204± 0.02 mdx: 0.114± 0.01	N.R	WT: 0.029± 0.001 *mdx*: 0.018± 0.001	N.R
Novotny et al. (2011)	7-weeks mice tibia	N.R	WT: 0.202± 0.004 *mdx*: 0.210± 0.007	WT: 0.69±0 .03 mdx: 0.114± 0.01	WT: 0.092± 0.013 *mdx*: 0.059± 0.005	WT: 0.041± 0.002 *mdx*: 0.038± 0.002	WT: 0.192 ± 0.006 *mdx*: 0.237 ± 0.008
Rufo et al. (2011)	24-weeks mice tibia	WT: 0.62±0.04 mdx: 0.55±0.02	WT: 244.0± 13.0 *mdx*: 230.0± 11.0	WT: 0.40±0 .01 mdx: 0.35±0 .02	WT: 9.2±0.9 *mdx*: 5.7±1.1	WT: 0.036± 0.0023 *mdx*: 0.037± 0.0026	WT: 0.236 ± 0.007 3 *mdx*: 0.289 ± 0.028 5

*N.R= Not reported

Structural Model Index (SMI)

A primary bone parameter in the description of the microstructure of trabecular bone is SMI. SMI may be used to determine the geometry of the trabeculae is of a plate or a rod shape in 3D trabecular bone images (Figure 2-15). "Rods" are regions of trabecular bone characterized by being elongated and cylindrical, whereas "plates" are extensive, flatter regions (Salmon et al., 2015). SMI is included in BoneJ and it is based on the mathematical model by Tor Hildebrand & Ruegsegger (1997). The method calculates the change in bone surface area. The limiting SMI values to indicate plateness and rodness are 0 and 3, respectively. In human, trabecular plates have a higher tissue mineral density compare to that of trabecular rods. Interestingly, Wang et al. (2015) found that this suggests a lower bone turnover as a result of lower surface to volume ratio in trabecular plates. To study trabecular architecture and mechanics, connectivity and anisotropy should also be studied (Odgaard, 1997).
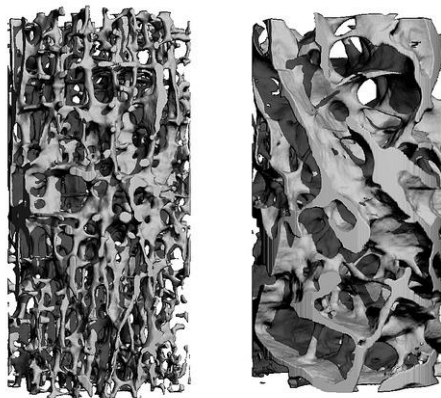
Figure 2-15 3D µCT of trabecular bone.
The structural elements of trabecular bone showing a plate-like (right) and a rod-like bone structure (left). The relative proportion of rods to plates in trabecular bone is thought to be important for bone's mechanical competence, with plates considered to be mechanically superior to rods (Adapted from www.metafilter.com).

SMI has been used as a standard measurement parameter for trabecular bones. However, a recent report questioned this approach to determine the rodness and plateness of trabecular bone (Salmon et al., 2015). It argued that SMI assumes that the entire surface is convex while the intricate connections within the trabecular continuum suggest that a high proportion of the surface could be concave. Moreover, they tested SMI and compared the results with the fraction of the surface that is

concave (CF) and mean ellipsoid factor (EF). The proportion of the surface area that is concave (the "concave fraction," CF) can be calculated as the proportion of the total surface area (S) covered by triangles that decrease in area during mesh dilation (U). Briefly, for each point of the structure's medial axis, a small ellipsoid is seeded and iteratively dilated, rotated, and translated slightly until no further increase in volume is achieved. Then, the largest ellipsoid containing each point in the structure is determined, and the EF calculated for that point. Mean EF values summarizing all the foreground pixels in each image were calculated and used for comparisons (Salmon et al., 2015). They found EF method is able to discern better the trabecular geometries of mammalian and avian bones (Doube, 2015).

Connectivity Density (Conn.D)

According to Russ & Dehoff (2001), connectivity is a property that applies primarily to network structures such as blood vessels or neurons in tissues used to describe the number of redundant connections between locations. It was also defined as the maximum number of trabeculae that can be cut without separating the structure. By the definition of Conn.D, plate perforation and rod connection contribute to an increase in Conn.D and plate perforation filling and rod disconnection contribute to decreased Conn.D (Odgaard, 1997). Connectivity can be determined by various methods as discussed in Odgaard (1997). A practical method is the topological approach where trabecular bone is considered as a node-and-branch network. BoneJ Connectivity density uses the Euler characteristic or Euler number of 3D data (Figure 2-16). In ImageJ, this value is very sensitive to the number of particles in the image and noise. Connectivity density (Conn.D) can be calculated by dividing the connectivity estimated by the volume of the sample. It is recommended to present the connectivity in a density form (Bouxsein et al., 2010).
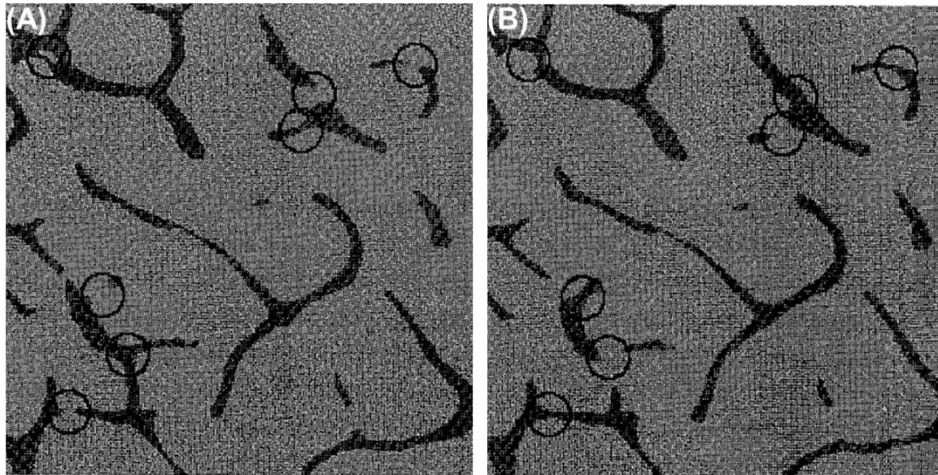
Figure 2-16 Two consecutive serial sections of trabecular bone.
Topological changes between the two sections are indicated by the circles. By noting and counting these occurrences, the Euler number density may be calculated (Odgaard, 1997).

2.6 Evaluation of Bone Mechanical Competency using Three-Point Bending Testing.

The ability of bone to resist fracture is important for the study of the mechanical competence of the bone. Many types of mechanical tests have been proposed for testing of mouse bones (Akhter et al., 2004). Bone has a well-defined organisational hierarchy, mechanical tests scale the natural length scale from mineral and protein levels to whole bone tests. Beaupied et al. (2007) critically reviewed biomechanical tests available for measuring bone fragility. There are torsional testing, traction and compression as well as bending testing. Reviews on specimen preparation prior testing are also included. A practical guideline by Jepsen et al. (2015) has provided recommendations for evaluating phenotypic changes in mouse bones.

Three-point bending is one of the most common arrangements for testing of whole bones. Due to its simplicity, the mechanical properties of mouse bones have been determined using this setup. The changes in the structural and material properties might be due to exercise (Frajacomo et al., 2013; Wallace et al., 2007; Wergedal et al., 2006), variation among inbred mouse strains (Wergedal et al., 2006), accelerated senescence (Silva et al., 2002) and ovariectomy (Maïmoun et al., 2012). Akhter et al.

(2004) reported a comprehensive analysis of transgenic mice using three-point bending tests.

Mechanical testing of bone may contribute to the understanding of how bone responds to mechanical stimuli in selected genotypes, such as the absence of dystrophin and P2RX7 receptor. Such an investigation has been conducted by Nakagaki et al. (2011) on *mdx* and control (wild-type, WT) 21-day old mice bones. Using three-point bending test, Nakagaki et al. (2011) found that *mdx* mice have reduced fracture resistance compared to WT mice bones. The results corroborate the findings of Novotny et al. (2011), with a similar trend observed for 7-weeks and 24-months old mice. They found that *mdx* mice have reduced 50-80% in tibial strength and stiffness compared to that of the WT mice. The cross-sectional moment of inertia (CSMI) and the cortical cross-sectional area of the *mdx* midtibia was 25% and 6-17% lower than those of the WT mice. This shows that *mdx* bones are smaller than WT.

Silva et al. (2002) compared morphological, mechanical and densitometric properties of long bones from SAMP6 (senile osteoporosis) mice to those of SAMR1 (control strain). They found increased bone size, decreased bone strength and increased mineralisation in SAMP6 mice. The results were analogous to changes in aging adult bones. Further, Silva et al (2004) reported mouse bone structural and material properties using four-point bending and nanoindentation approaches. These approaches allow determination of bone tissue properties to identify changes as the result of pathogenesis process.

A report on muscle-bone interactions by Montgomery et al (2005) showed that mdx mice have significantly larger hindlimb muscles than controls due to extensive fibrosis. Larger hindlimb muscles may have contributed to greater BMD and fracture strength in *mdx* mice than controls even when accompanied by a dystrophic phenotype. The data showed a relationship between the hindlimb muscle mass and the femoral BMD.

A number of guidelines (Jepsen et al., 2015; Turner and Burr, 1993) and experimental work have been published on whole bone bending testing (Akhter et al., 2004; Donnelly et al., 2010). Whole bone three-point bending test is useful for measuring the mechanical properties of small animal bones and it is easy to

implement. In this test, the whole-bone is loaded in bending until failure at a constant loading rate. Table 2-4 shows a summary of the reported three-point bending tests.

To date, there have been no reports of bone properties from P2RX7 receptor knockout mouse bones. A recent work shows that this receptor is a good target for the pharmacological treatment of DMD, as its blockade ameliorated muscle and non-muscle symptoms as well as inflammation (Sinadinos et al., 2015). However, ablation or blockade of P2RX7 could affect bone formation and function directly due to its regulatory role in bone cells, where this receptor activation has been linked, primarily, to osteoclast functions (Agrawal and Gartland, 2015; Agrawal et al., 2003; Gartland, 2012). If P2RX7 is abnormally active in dystrophic bones in a manner similar to the over-activation in muscles, its disruption might improve the bone structure. On the other hand, its ablation leading to deficient bone formation and excessive resorption could have a negative impact. It is therefore of great interest to examine the impact of P2RX7 receptor ablation on the dystrophic bone structure, as this might be a new treatment avenue for this lethal disease.

2.6.1 Biomechanical properties of bone

The fracture prevalence in DMD patients is increased as the disease progresses. A report by McDonald et al. (2002) has revealed that the peak age for the occurrence of fractures in DMD is in 8-11 years old (40.2%) and the most predominance fracture site is in the lower limb. 47% of fractures occurred more commonly in the independently mobile group than other mobility group (total of 102 number of fractures). They suggested the contributing factors are reduced bone density, diminished power and motor agility and increased susceptibility to injury during play. Moreover, the effects of any treatment on bone structural properties may be reflected on changes in material and/or tissue properties (Ferretti et al., 2001; Van der Meulen et al., 2001). Therefore, it is of great interest to assess bone strength and fracture risk in bone related diseases to evaluate the bone quality. For trabecular bone, however, the biomechanical properties traditionally obtained using compressive testing may cause error up to 40% and may not be able to detect changes in the mechanical properties (Odgaard, 1997). According to Odgaard (1997), there are two

important problems with all studies of mechanical properties of trabecular bone. First, the mechanical properties have almost never been described completely. The mechanical properties vary with loading orientation, that is, trabecular bone is mechanically anisotropic. Second, reported mechanical constants are rarely accurate. Mechanical tests are influenced by inherent errors and problems, which include specimen geometry, friction of endplate, structural end phenomena, storage, continuum assumption, viscoelasticity and temperature effects. Consequently, the mechanical test of trabecular bone may not be able to detect changes in the mechanical properties of the bone.

The mechanical properties of bone tissue may play a critical role in bone strength, in addition to bone mineral density. For clinical investigations, laboratory tests of whole bone strength are often used as a surrogate measure for in vivo fracture prediction. These will provide comprehensive knowledge on the specific gene functions and disease mechanisms (Blank, 2001; Chen et al., 2015; Finnilä et al., 2010; Herlin et al., 2013; Volkman et al., 2004). Alterations in these mechanical properties would be expected to play a significant factor in bone fracture risk, even though it has not been clear what mechanical properties are most important (Currey, 2004). A number of parameters can be obtained to understand comprehensively the bone fracture mechanism (Table 2-3). The most recent work (Jepsen et al., 2015) has provided a practical and systematic guideline focused on the testing of long diaphysis and cortical bones.

Table 2-3 Basic biomechanical terminologies (Jepsen et al. (2015).

Structural properties	Material properties
Stiffness (N/mm)	Elastic Modulus (or tissue level stiffness) (N/mm^2)
Maximum load (or whole bone strength) (N)	Ultimate stress (tissue-level strength) (N/mm^2)
Postyield displacement (mm)	Postyield strain (mm/mm)
Work-to-fracture (N·mm)	Toughness (N/mm^2)

An investigation of the relationship between the material properties and the geometry and mechanical behaviour of whole bone is challenging and complicated. This is

because bone is a composite hierarchical material (Poundarik and Vashishth, 2015). To understand the mechanical behaviour of whole bones during physiological loading would facilitate the understanding of the effects of various pathological processes and drug treatments (Poundarik and Vashishth, 2015; Sharir et al., 2008).

The biomechanical parameters shown in Table 2-3 may be used to characterise the bone integrity. The structural or whole-bone properties are measured using intact bones which are size-dependent whereas material or tissue level properties assess the material and are size-independent (Jepsen et al, 2015). The load-displacement curve has been used to determine the structural and material properties (Figure. 2-17). From the slope of the linear part of the curve, stiffness (or flexural modulus) can be determined. Maximum load, postyield displacement and work-to-fracture can be derived from the same curve. The maximum load represents the general integrity of the bone structure. Postyield displacement and work-to-fracture represent ductility and fracture resistance, respectively.
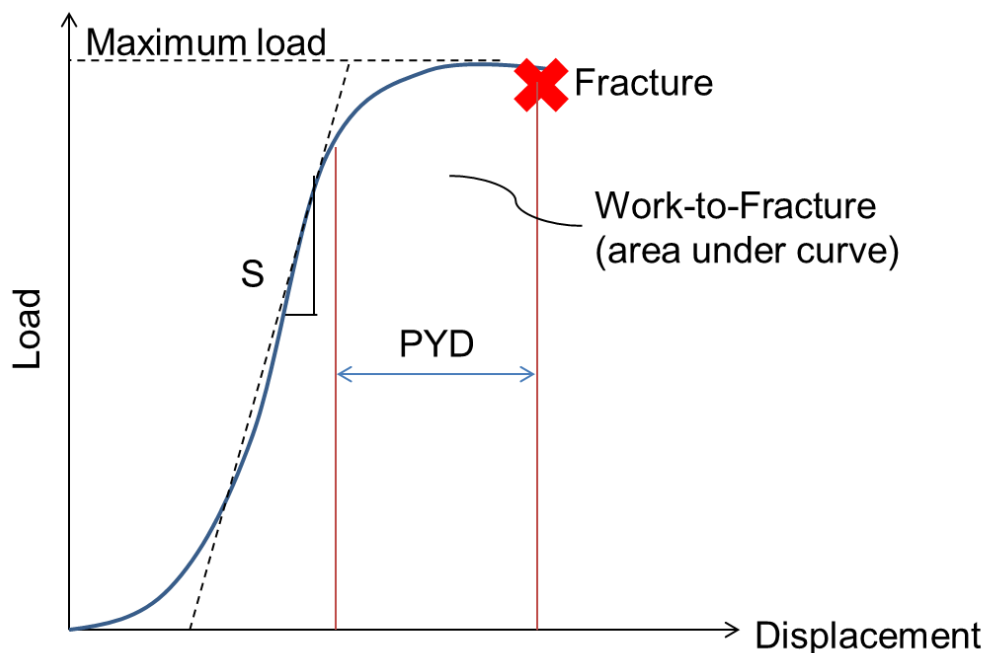
Figure 2-17 A typical load-displacement curve.
The stiffness, S (slope of the curve); maximum load, work-to-fracture (area under the curve) and postyield displacement (PYD) (indicative of ductility). Red Cross represents final fracture (Adapted from Jepsen et al. 2015).

Stress and strain curve is obtained when load converts into stress and deformation converts into strain. The slope of the curve within the elastic region is defined as the elastic or Young's modulus. The Young's modulus obtained from the slope of the elastic portion of the stress-strain curve is a measure of the intrinsic stiffness of the material (Turner, 2006).

The strength of the bone is defined by the load sustained before the failure (Dalla and Bankoff, 2012). It is not directly proportional to risk of fracture for which work-to-fracture should be used. Bone strength is a first parameter to assess bone competency following a treatment. Bone mineral density (BMD) is considered as a gold standard to evaluate the bone strength (Amman and Rizzoli, 2003), although BMD cannot predict bone fracture risk accurately (Graeff et al., 2007). Bone mineral provides strength and stiffness to the tissue while collagen provides viscoelastic properties and resistance to fracture. The mineral to collagen ratio does affect the bone strength and brittleness (Wang et al., 2002).

A multi-scale analysis was reported in which they found differences in the mineralisation level between Phospho1$^{-/-}$ (lack of phosphatase) and oim$^{-/-}$ (osteogenesis imperfecta model) mouse bones (Rodriguez-Florez et al. 2014). However, the tissue elastic modulus was reduced in both bones. They concluded that mineralization is not the only determinant of tissue elastic moduli and that they are not necessarily correlated. They also suggested other determinants such as the deviation in size, composition and organisation of bone mineral affecting bone micro-mechanics.

Table 2-4 A summary of three-point bending tests from the literature.

Reference	Type of bone	Disease	Displacement Rate (mm/s)	Span (mm)
Ammann et al. (1997)	24-week-old mice tibia	Estrogen deficiency	0.033	8
Turner et al. (2000)	16-week-old mice femur & lumbar	Low bone mass	0.500	5
Akhter et al.	17-week-old	LRP5 mutant	0.0500	5

(2004)	mice femur			
Montgomery et al. (2005)	16-week old mice femur	DMD	0.100	5
Finnila et al. (2010)	35 & 70 post natal days rat	Dioxin	0.155	13
(Donnelly et al., 2010)	6-week-old male rat	Vitamin D and calcium deficiency	0.050	7.5
Nakagaki et al. (2011)	4-week-old mice femur	DMD	0.050	5
Novotny et al. (2011)	7-week-old mice tibia	DMD	0.033	10
Herlin et al. (2013)	8-12-week-old mice tibia	TCDD-induced toxicity	0.155	6.5
Melville et al. (2014)	4-18-week-old mice femur	Estrogen Receptor-Alpha deficiency	0.100	6

*N.R= Not reported

Table 2-5 The mechanical properties of *mdx* and control mice reported in the literature.

Reference	Type of bone	Max. Load (N)	Stiffness (N/mm)	Yield Load (N)	Energy to Fracture (N·mm)
Montgomery et al. (2005)	16-weeks old mice femur	WT: 20.9±2.2 *mdx*: 23.1±1.9	WT: 45.8± 9.6 *mdx*: 55.1±15.6	N.R	WT: 4.8±0.72 *mdx*: 5.1±1.6
Novotny et al. (2011)	7-weeks mice tibia	N.R	N.R	N.R	WT: 3.15±0.24 *mdx*: 2.32±0.28

| Nakagaki et al. (2011) | 3-weeks old mice femur | WT: 4.60±1.05 *mdx*: 2.25±0.41 | WT: 10.76±1.62 *mdx*: 5.82±2.69 | WT: 2.98±0.51 *mdx*: 1.76±0.37 | N.R |

*N.R= Not reported

2.7 Evaluation of Bone Fracture Surface Morphology using Scanning Electron Microscope (SEM)

Scanning electron microscope (SEM) is a powerful technique for investigating bone architectural integrity and bone quality. It is effective in investigating the bone morphology and fracture surfaces (Zhang et al. 2015; Banse et al. 2005). SEM can be used to compare morphologically the fracture surfaces of the genotypes that have undergone mechanical testing to investigate the failure mechanisms. It uses electrons produced by heating of a tungsten filament or a field emission gun. The electron beam is accelerated through a high voltage field and makes its way through electromagnetic lenses which focus and direct the beam towards the sample. Once it hits the sample, other electrons (backscatter or secondary) are ejected from the sample. Detectors collect the secondary or backscattered electrons, and convert to signals sent to a viewing screen. Coating is necessary for nonconductive materials like bone before scanning (Li et al., 2013). Creating a conductive layer of metal on the sample inhibits charging, reduces thermal damage and improves the secondary electron signal required for topographic examination in the SEM.

To date, no studies have been reported on SEM studies post mechanical testing of mouse bones of different genotypes. The established histomorphometry techniques, where the bone was sliced into thin sections is destructive compare to SEM, although it may provide higher resolution (Carbonare et al., 2005).

Back-scattered Electron (BSE) and SEM were carried out together with Thermogravimetry Analysis (TGA) to assess the mineral content in the 7 week young mouse bones (Rodriguez-Florez et al., 2014). Chen et al. (2006) investigated mouse bones of 4 to 32 week old of SAMP6 (senescence-accelerated mouse or senile osteoporosis) and SAMR1 (age-matched normal mouse or control); while Rubin et al. (2004) investigated C57BL/6J (low bone mass) and C3H/HeJ (high bone mass)

types. Both studies utilised SEM and TEM. At periosteum level at 1 month of age, Chen et al (2006) found no difference in Sharpey's fiber diameters and number of mast cells using SEM and TEM, respectively. Sharpey's fibers are the fibers rooting from the periosteum and seen continuously with anteromedial bundle. Rubin et al (2004) found fewer trabecular numbers in the vertebra and femur in C57BL/6J compared to those of C3H/HeJ, but morphologically at the meso-structural level, they appeared similar.

2.8 Evaluation of Bone Material Properties using Nanoindentation.

Nanoindentation has been used to investigate the intrinsic bone material properties by measuring the hardness and elastic modulus at the nanoscale in human bone (Fan et al., 2002; Hoffler, 2005; Zioupos and Currey, 1998; Zioupos, 2005; Zioupos et al., 2008), dentin (Habelitz et al., 2001; Zioupos and Rogers, 2006) and mouse or rat bone (Akhter et al., 2004; Finnilä et al., 2010; Herlin et al., 2013; Jämsä et al., 2002; Rodriguez-Florez et al., 2013). In addition, the use of nanoindentation has been extended to assess also storage and loss modulus (viscoelastic properties) in dynamic nanoindentation when dynamic oscillation is included, as reviewed by Cohen & Kalfon-Cohen (2013). The nanoindentation technique is useful in investigating the nanomechanical properties of bone microstructure of different phases due to changes caused by specific bone disease (Jämsä et al., 2002; Maïmoun et al., 2012). However, there has been no literature reported on the nanomechanical properties of *mdx* and P2RX7 receptor knockout mouse bones.

Storage modulus (E') is an indication of bone tissue's ability to store deformation energy in elastic manner. Higher E' denotes higher strength and mechanical rigidity characteristic as oppose to lower E'. Loss modulus (E'') is a measure of energy dissipation. Though material is less stiff or hard, more energy may be dissipated as heat, increasing E''. Much less energy is stored if the molecules can move with the force leading to a rapid decline in E'. The relative changes in E' and E'', for example, E' is larger than E" indicates that the material has some capacity to store energy and should be able to return, to some extent, to its initial configuration before a

mechanical force is applied. The material behaves as an elastic solid, although some of the mechanical energy is dissipated. When the applied force is higher, the microstructure collapses and the mechanical energy given to the material is dissipated. This means that the material flows; E" becomes larger than E'. Reduced modulus, E_r is related to the stiffness of the bone. A higher modulus represents a stiffer material. For diamond indenter, the E_r is dominated by the sample properties.

Previous studies using nanoindentation have been carried out in small animal bones such as mouse bones. For example Silva et al. (2004) has extended their work from Silva et al. (2002) on assessing the material properties of mouse bones of SAMP6 (senescence-accelerated mouse or senile osteoporosis) and SAMR1 (age-matched normal mouse or control) at 4 and 12 months of age using the nanoindentation technique. They found distinct changes for elastic modulus and hardness in SAMP6 mouse bones. It is known that the elastic modulus of cortical bone depends on its degree of mineralisation. Modulus correlates with calcium content in cortical bone across a range of animal species, and ash fraction or other measures of mineralisation explain 25-30% of the variation in the elastic modulus of human cortical bone. The same conclusion was also made for cortical and tibia bones of rat exposed to dioxin (Finnila et al., 2010).

The nanoindentation parameters from both standard and dynamic protocols have been used to quantitatively measure the hardness of the trabecular and cortical bone of new born rats. In their study, the findings showed a disturbed maturation process of the pup tibia at the bone matrix level as a result of the exposure to Tetrachlorodibenzo-p-dioxin (TCDD) (Finnila et al., 2010). The limitation of this method is variations within a single sample may be as high as 40% to 60%, due to sample surface roughness (Hengsberger et al., 2002), for example. To reduce the variation, precise and selective positioning of the indent in the heterogeneous bone microstructure is needed.

A most recent study utilised the nanoindentation technique to examine mouse cortical and trabecular bones to study the multi-scale hierarchy organizational bone for a better understanding of the age related changes in bone properties. The study reported a detailed multi-scale analysis of long bones in male Wistar rats with ages of 1, 3, 5, 7, 9, 11, 14, 15, 16, and 17 months. Femoral trabecular and cortical bone

properties (i.e., microarchitecture, mechanical properties, and mineral contents) were measured by multi-level tests. This study partly provided a theoretical basis for an understanding the age-related macro-mechanical properties, microarchitecture and material properties, and the degradation of male skeleton properties caused by aging. Age-related bone properties at multi-levels (i.e., microarchitecture parameters of femur, failure load and elastic modulus of femoral cortical bone, and size and roughness of bone mineral grains) will provide a fundamental basis for clinical research on age-related bone properties (Zhang et al. 2015).

The nanoindentation approach has an attractive feature of testing precisely local mechanical properties of a single bone structural unit. For this reason, nanoindentation may help in understanding the bone quality and bone alteration at the nanoscale of the *mdx*/P2X7$^{-/-}$ and DMD model of mouse bones. Furthermore, nanoindentation test can assess local time-dependent viscoelastic mechanical properties. No research has been reported so far to use the nanoindentation to investigate the *mdx* and WT as well as associated animal model bone matrix properties at nanoscale.

Nanoindentation has been used to investigate tissue quality by measuring both hardness and elasticity with high resolution. The viscoelastic properties of the material can be determined from small areas at high spatial resolution (30 nm) (Ammann and Rizzoli, 2003; Lewis and Nyman, 2008). Depth-sensing indentation systems thus, appear well suited for investigating bone properties at matrix level. Bone matrix level contains inorganic salts primarily hydroxyapatite and some calcium carbonate and collagen fibers.

One of the challenges to obtain reliable data in bones is their anisotropy, inhomogeneity and irregularity. Fan et al. (2002) were the first to quantitatively evaluate the anisotropy of cortical bone using the nanoindentation technique. Anisotropic properties are due to the three-dimensional arrangement of collagen fibrils, a main reason for the reported high variation in the results (Finnilä et al., 2010; Herlin et al., 2013).

Ritchie et al. (2008) and Isaksson (2010) reported a variation in results between 9 and 40%, respectively. The latter employed different nanoindentation methods to

compare the time-dependent viscoelastic properties of cortical and trabecular bones. They found that a high frequency semi-dynamic test (Coefficient of Variation 9-10%) showed higher precision. There are potential sources of error in the determination of stress intensities from the edge-cracked thick-walled cylinder in bending stress-intensity solutions due to (i) the experimental precision with which the bone geometry and mechanical parameters can be measured and (ii) the deviations of the cross sections of rat and mouse bone from the circular cylinder with uniform wall thickness (Ritchie et al., 2008).

Turner et al. (1999) reported the elastic modulus of cortical and trabecular bones of human femur using nanoindentation. The calculation of Young's modulus using nanoindentation assumes that the material is elastically isotropic. The results suggest that this assumption does not limit nanoindentation as a technique for measurement of Young's modulus in anisotropic bone. The review by Ruppel et al. (2008) focused on the changes in bone structure due to osteoporosis and associated diseases. They also discussed the importance of matrix organisation and how the constituents differ from each other i.e. trabecular, cortical, lamellae, mineral crystal and collagen fibers; and nanoindentation was able to discriminate the microstructural details of bone.

A review by Lewis and Nyman (2008) comprehensively discussed the principles of the nanoindentation technique and presented information on areas for future studies. Bone tissues and teeth as mineralised hard tissues were discussed, hence a good reference for studying the material properties of the tissues. The principle of nanoindentation lies in measuring the load and the deformation of an object using a very small tip probe as it is advanced into the surface of the object producing an imprint (Shepherd et al., 2011). Diamond is most commonly used and it has a tip radius less than 25 nm to ensure good imaging resolution and nanometer-scale indents at the level of osteons and lamellae. The data from load-displacement curves are used to estimate the elastic modulus using the Oliver and Pharr method (Oliver and Pharr, 2004). This is done from the unloading phase data as the near maximum load derivative of a power law fitted polynomial (Zioupos and Rogers, 2006). The most commonly used protocol is quasistatic or standard, comprising a loading, a hold and a unloading phase. When dynamic oscillation is included, viscoelastic

behaviour can also be assessed. The viscoelastic behaviour of bone at the macroscopic scale is primarily due to microstructural features, interfaces, or fluid flow, rather than viscous behaviour of the bone tissue. As viscoelasticity affects the fatigue behaviour of materials, the microscale properties may provide a measure of bone quality associated with initial damage formation (Shepherd et al., 2011).

2.8.1 Advanced (Standard) Nanoindentation

The fundamental nanoindentation equations were developed by Oliver and Pharr (1992), who developed an analytical model and a measurement protocol to quantitatively calculate elastic modulus and hardness. The modulus was defined as the ratio between stress and strain (σ / ε), and can be directly computed from the nanoindentation load-displacement curve under a small load. The Oliver & Pharr method (Oliver and Pharr, 2004) has been developed into an acceptable standard analytical technique for mechanical property deconvolution. This technique has been widely used where the indentation technique is adapted specifically for the characterisation of small-scale mechanical behaviour. It relies on a time-independent response in the experimental time frame, developed without the need to image the hardness impression. An assumption in this method is that the slope of the unloading response is purely elastic. A review by Lewis and Nyman (2008) has the most complete synthesis to date of characterisation of mineralised hard tissues.

In addition, Zioupos and Rogers (2006) explained in detail the various parameters of the nanoindentation method in investigating the structure of human dentine and enamel. A number of nanoindentation protocols can be used to produce various impression characteristics. The most commonly used is quasi-static or standard protocol, which consists of a loading, a hold and an unloading. The indentation modulus is calculated from the load-deformation curve during unloading-retracting phase as per Oliver and Pharr method (1992). Zioupos and colleague showed that nanoindentation can be used to study biomaterial in general and for the local characterisation where it is used to probe properties within small volumes.

As mentioned above a nanoindentation loading protocol consists of a loading phase, a hold phase, and an unloading phase, as shown in Figure 2-18(a). The fundamental

experimental parameters of nanoindentation are illustrated in Figure 2-18(b). In dynamic mode as shown Figure 2-18(b), a further implementation may result from analysis of the amount of energy absorbed (ψ_p) and recovered upon indentation (ψ_e). This may provide some quantification of the plastic response of the material.
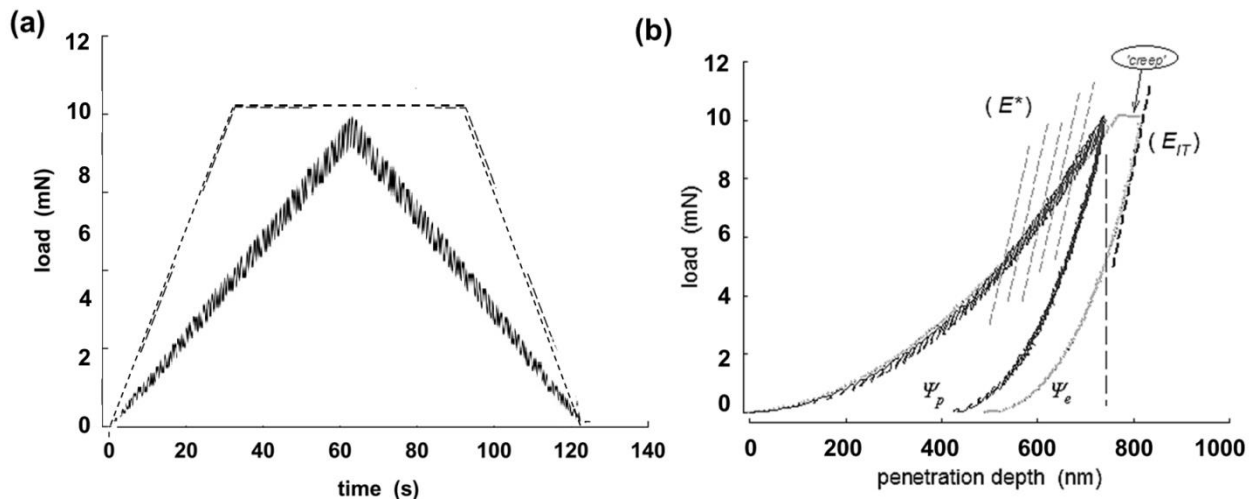
Figure 2-18 Advanced and sinus load-time curves.
(a) Load-time traces for two examples of advanced/standard and dynamic/sinus nanoindentation loading protocols at a maximum load of 10 mN. The standard protocol includes a hold phase to study penetration creep strain. (b) Load-depth traces of the protocols showing where the elastic modulus values are produced in the unloading phase of the indentations and two further implementations we derived here to quantify plasticity (by measuring the plastic and elastic work fractions ψ_p, ψ_e under the sinus trace) and the development of creep penetration strain in the hold phase of the standard protocols (Zioupos and Rogers, 2006).

Considering the hierarchical structure of bone, the viscoelastic properties from nanoindentation may not reflect the macroscopic behaviour of bone, regardless of the loading protocol used. The deformation mechanisms during indentation differ from those in macroscopic testing. When a Berkovich indentation tip is used, there is damage formation below the tip where permanent deformation occurs (Shepherd et al., 2011).

Table 2-6 shows the application of advanced nanoindentation technique on small animal bones. The nanoindentation instruments make it possible to examine the

material properties at the bone matrix level considering the hierarchical structure of bone.

Table 2-6 Bone matrix properties obtained using the nanoindentation technique on small animal bone from the literature.

Reference	Type of bone	Hardness (GPa)	Elastic Modulus (MPa)	Creep, C_{it} (%)
Silva et al. (2004)	4mo & 12 mo mice tibia	4mo **SAMR1**:980±90 **SAMP6**:1110±103 12mo **SAMR1**:1110±90 **SAMP6:**1260±80	4mo **SAMR1**:27.8±1.8 **SAMP6**:29.9±2.1 12mo **SAMR1**:30.8±1.8 **SAMP6**:33.1±1.3	N.R
Finnila et al. (2010)	Post natal days (PND) 35 & 70 rat	PND 35 **Control:**804.2±55.5 **Treated:**838.0±76.8 PND70 **Control:**978.8±102.9 **Treated:**923.1±91.9	PND 35 **Control:**19.0±1.7 **Treated:**19.4±1.5 PND70 **Control:**19.3±2.3 **Treated:**20.0±3.0	A_{creep} (overall creep strain amplitude) PND 35 **Control:**0.019±0.002 **Treated:**0.019±0.003 PND70 **Control:**0.016±0.004 **Treated:**0.017±0.004
Herlin et al. (2013)	8-12 weeks old mice	$Ahr^{+/+}$(**Cortical**) **Control**: 677±33 **TCDD**: 710±46 $Ahr^{-/-}$(**Cortical**) **Control**: 732.41±2.0	$Ahr^{+/+}$(**Cortical**) **Control**: 24.1±2.0 **TCDD**: 24.7±3.3 $Ahr^{-/-}$(**Cortical**) **Control**: 25.5±1.4	$Ahr^{+/+}$(**Cortical**) **Control**: 9.1±0.7 **TCDD**: 9.0±0.7 $Ahr^{-/-}$(**Cortical**) **Control**: 8.6±0.3

		TCDD: 710±35 Ahr[+/+](**Trabecular**) **Control**: 635±38 TCDD: 712±46 Ahr[-/-](**Trabecular**) **Control**: 663±67 TCDD: 622±86	TCDD: 25.2±1.5 Ahr[+/+](**Trabecular**) **Control**: 19.3±1.9 TCDD: 21.8±1.0 Ahr[-/-](**Trabecular**) **Control**: 19.8±2.0 TCDD: 19.4±2.9	TCDD: 8.8±0.4 Ahr[+/+](**Trabecular**) **Control**: 9.2±0.5 TCDD: 8.3±0.6 Ahr^{-/-} (**Trabecular**) **Control**: 9.1±1.4 TCDD: 9.6±1.2

[*]N.R= Not reported

2.8.2 Sinus (Dynamic) Nanoindentation

Dynamic nanoindentation provides an evaluation of time-dependent properties of a material. Herlin et al (2013) and Finnila et al. (2010) reported results using both quasi-static and dynamic protocols on rodents' bones. Sun et al. (2014) also used both protocols on other biomaterials (nacre, cattle horn and beetle cuticle).

Time-dependent viscoelastic properties of animal bones have been studied by Isaksson et al. (2010). They examined the time-dependent behaviour of bovine cortical and trabecular bones including creep, the effect of loading rate, dissipated energy, and semi-dynamic testing. They suggested a high frequency semi-dynamic test, and the protocol was used to demonstrate that the bone has the ability to adapt to mechanical loading by storing and damping the energy exerted (Cohen et al, 2013). Table 2-7 shows the primary dynamic protocol measurements reported in the literature; while Table 2-8 shows the additional parameters representative of the viscoelasticity of the bone.

Table 2-7 Primary bone matrix properties obtained from the nanoindentation technique on small animal bones using the dynamic protocol. * ($p < 0.05$)

Reference	Type of bone	Hardness (GPa)	Elastic Modulus (MPa)	Plasticity
Finnila et	Post	PND 35	PND 35	PND 35

al. (2010)	natal days (PND) 35 & 70 rat	**Control:**951.4±94.0 **Treated:**940.3±100.5 PND70 **Control:**1196.6±166.5* **Treated:**1074.8±145.9	**Control:**19.6±1.6 **Treated:**19.6±1.6 PND70 **Control:**20.0±1.8 **Treated:**20.3±3.2	**Control:**0.75±0.03 **Treated:**0.76±0.03 PND70 **Control:**0.71±0.03 * **Treated:**0.74±0.04
Herlin et al. (2013)	8-12 weeks old mice	Ahr[+/+](**Cortical**) **Control**: 845±51* **TCDD**: 921±52 Ahr[-/-](**Cortical**) **Control**: 864±52 **TCDD**: 844±53 Ahr[+/+](**Trabecular**) **Control**: 804±52 **TCDD**: 863±56 Ahr[-/-](**Trabecular**) **Control**: 795±73 **TCDD**: 789±94	Ahr[+/+](**Cortical**) **Control**: 23.0±0.8 **TCDD**: 23.9±1.1 Ahr[-/-](**Cortical**) **Control**: 23.6±1.2 **TCDD**: 22.5±1.4 Ahr[+/+](**Trabecular**) **Control**: 17.4±1.4* **TCDD**: 19.5±1.1 Ahr[-/-](**Trabecular**) **Control**: 17.8±1.4 **TCDD**: 17.9±2.2	Ahr[+/+](**Cortical**) **Control**: 25.9±0.5 **TCDD**: 26.7±1.8 Ahr[-/-](**Cortical**) **Control**: 25.1±0.4* **TCDD**: 26.0±1.3 Ahr[+/+](**Trabecular**) **Control**: 31.8±1.5 **TCDD**: 30.6±0.8 Ahr[-/-](**Trabecular**) **Control**: 30.8±0.8 **TCDD**: 30.5±1.2

Table 2-8 Additional bone matrix properties obtained from the nanoindentation technique on small animal bones using the dynamic protocol. * ($p<0.05$)

Reference	Type of bone	Phase Diff. (º)	E.Store (GPa)	E.Loss (GPa)
Finnila et al. (2010)	Post natal days (PND) 35 & 70 rat	PND 35 **Control:**107±1.3 **Treated:**11.4±1.7 PND70 **Control:**9.9±1.7 **Treated:**11.1±1.9	PND 35 **Control:**22.9±1.7 **Treated:**22.6±1.7 PND70 **Control:**25.8±3.0* **Treated:**25.1±3.4	PND 35 **Control:**4.5±0.7 **Treated:**4.7±1.0 PND70 **Control:**4.7±0.9 **Treated:**5.1±1.3

Chapter 3

Experimental Methods

This research was ethically reviewed and approved by the University of Portsmouth. The microCT imaging and mechanical testing were conducted in the Mechanical Behaviour of Materials (MBM) laboratory, School of Engineering; animal preparation and SEM at the School of Pharmacy and Biomedical Sciences laboratory, University of Portsmouth (Approval gained from the Institutional Ethical Review Board and the Home Office UK ref 70/7479) while the nano-indentation experiments were conducted in the Biomechanics Labs, Cranfield Forensic Institute, Cranfield University, Shrivenham, Defence Academy of the UK.

3.1 Experimental Design

A summary of four primary experiments and two secondary experiments is represented in Figure 3-1.

The animals were selected based on previous studies and detailed in Sinadinos et al. (2015). The soft tissue was dissected to obtain tibia bones from each mouse (n=6 per genotype). To assess the specific role of P2RX7 receptor in DMD pathogenesis, P2RX7 ablation in *mdx* mice (*mdx*/P2X7$^{-/-}$) was adopted. The impact of ablation was determined at 4-weeks of age. This age group was chosen because at 4 weeks, it has been found that muscle inflammation is not prominent and they are considered to be in a more reparative or fibrotic phase (Giordano et al., 2015). At this age, the disease is fully manifested but the muscle loss and its effects on bone properties are thought not yet significant.

The present study utilised state-of-the-art micro-focus CT to create high resolution images of mouse bones to investigate whether the disrupted gene will have a direct effect on the bone structure. A previous study has shown that at approximately 3-weeks of age development of bone abnormalities can be observed. Notably, at this age,

degeneration of the bone cannot be affected by a previous muscular alteration as a result of modifications in gait and posture and by muscle weakness (Nakagaki et al., 2011).

Figure 3-1 shows the experimental flowchart for imaging, biomechanical and tissue properties analyses. µCT scanning was used for 3D microstructure analysis, bone image analysis for morphometric properties evaluation, three-point bending test for bone strength assessment, SEM for fracture morphology evaluation, two nanoindentation protocols for tissue properties analysis and TGA technique for bone composition analysis.

Nano- and micro- indentation testing, microtensile and microcompressive testing, and bending tests on whole bone specimens, offer the possibility to mechanically probe small animal bone and investigate the effects of aging, therapeutic treatments, disease, and genetic variation. In addition to traditional strength tests on small animal bones, fracture mechanics tests were also used to test tissue properties for fracture (Ritchie et al., 2008; Vashishth, 2008).
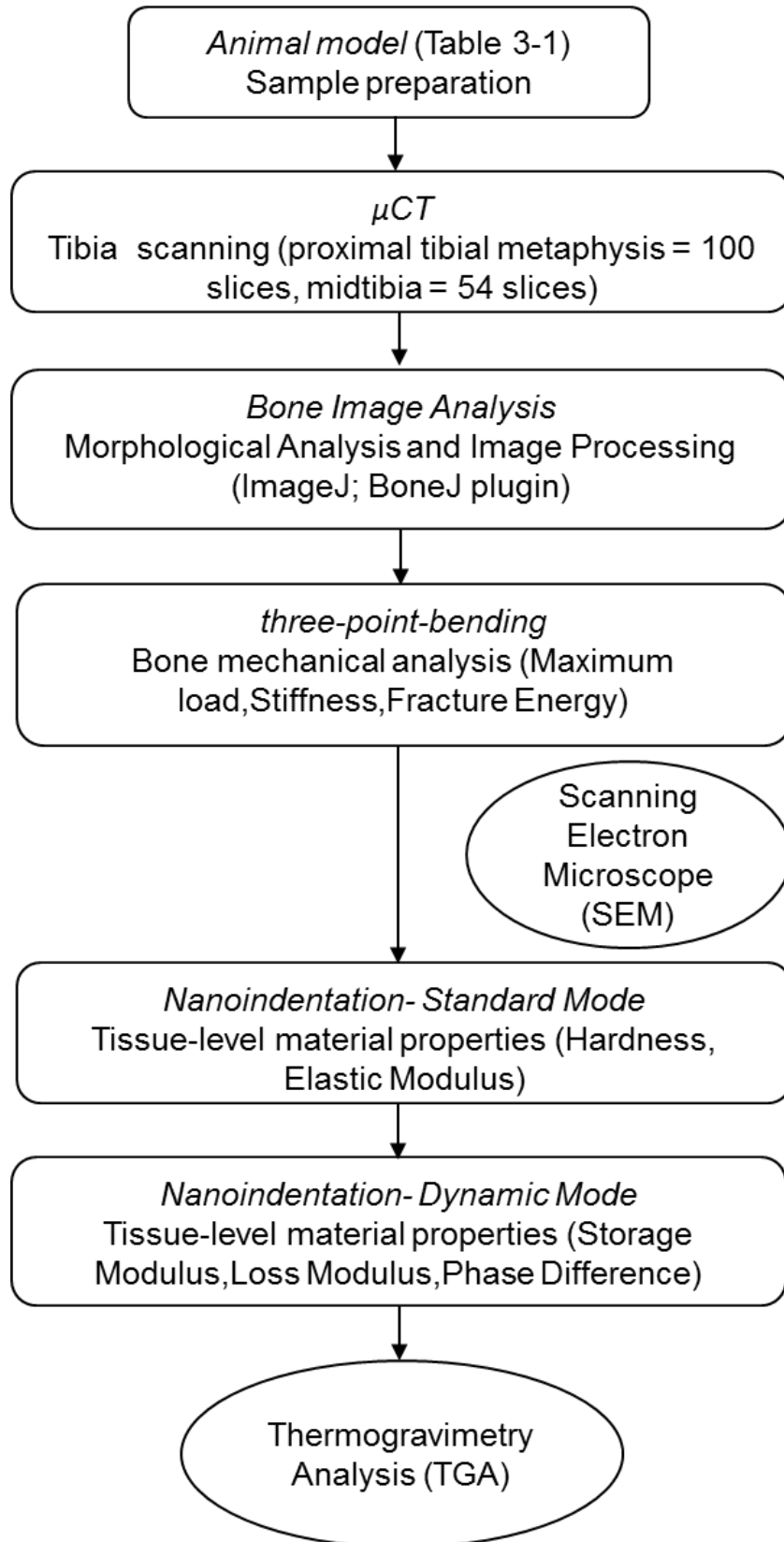
Figure 3-1 The experimental approaches used in this study.

3.2 The animal models

The animal models were prepared at the School of Pharmacy and Biomedical Sciences laboratory, University of Portsmouth. Animal models were central to the research as there is no *in vitro* system allowing testing a disease involving interdependent processes of muscle damage and inflammation. The *mdx* mouse is currently considered the most appropriate pre-clinical model to test treatment efficacy for DMD (http://www.treat-nmd.eu/research/preclinical/dmd-sops/). All animal experiments were performed in accordance with the approvals of the Institutional Ethical Review Board and the Home Office UK (70/7479).

Age matched male mice (wild-type, *mdx*, P2X7$^{-/-}$, *mdx*/P2X7$^{-/-}$) of mean age 31 days were used in the experiments. Some mice were collected at 28 days of age, some at 29 days, and some at 31 days (Table 3- 1).

Table 3- 1 Types of mice used in this study.

Genotype	Genetic background	Age	Gender	N
WT	C57BL10, wild-type, healthy	28 days	Male	6
mdx	DMD or dystrophic mice (Bulfield et al., 1984)	29 days and 31 days	Male	6
P2X7$^{-/-}$	P2RX7 receptor knockout mice (Solle et al., 2001)	29 days and 31 days	Male	6
mdx/P2X7$^{-/-}$	*mdx* and P2RX7 receptor knockout (double mutant) mice (Young et al., 2015)	28 days	Male	6

N=number of sample tested.

The *mdx*/P2X7$^{-/-}$ were generated by crossing P2RX7 receptor knockout male mice (Solle et al., 2001)(Solle et al., 2001) with *mdx* C57Bl/10ScSn-Dmd*mdx*/J female mice (Harlan Lab, UK), and genotypes were confirmed by genomic DNA PCR (Sinadinos et al., 2015). Animals were maintained in a 12 hours light/dark cycle and fed normal diet and water ad libitum. A total of 24 male mouse bones were used in the study. These included wild-type (C57BL10, n=6), dystrophic (*mdx,* n=6) (Bulfield et al., 1984), P2X7$^{-/-}$ (n=6) (Solle et al., 2001) and *mdx*/P2X7$^{-/-}$ (n=6) (Young et al., 2015), as summarised in Table 3- 1.

3.3 Sample Preparation

The tibia was prepared by carefully dissecting the muscle tissues and also other leg parts under a microscope. The tibias were placed in 10% buffered formalin overnight prior to saline storage in a fridge at 4°C for scanning and mechanical analysis. The tibias were kept in the saline solution until they were ready for scanning and mechanical testing. Left tibias for each of the genotypes were used for µCT scanning after about 2 weeks in the saline solution, followed by three-point bending testing, SEM examination and nanoindentation in up to 50 weeks.

After dissection the left tibia from each experimental genotype group were subjected to gross tibias geometry measurement before further radiological and biomechanical analysis. They were measured three times using a micrometric digital calliper and the average was calculated. The length and diameter measurements were taken from the centre of the condyles (proximal tibia) to the medial malleolus (distal tibia) (Di Masso et al., 2004), as shown in Figure 3-2.
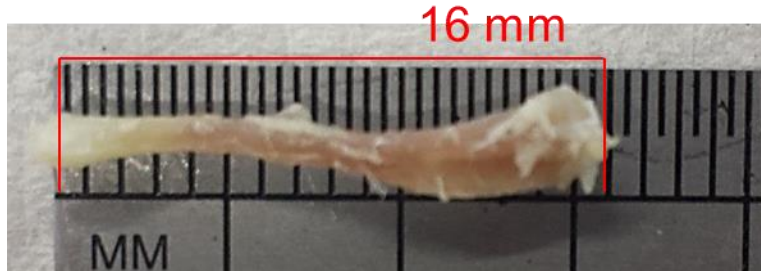
Figure 3-2 An illustration of the tibia length measured.
Tibial gross length and diameter measurements were taken from the centre of the condyles (proximal tibia) to the medial malleolus (distal tibia).

3.4 Micro-computed tomography (μCT)

The tibias underwent μCT scanning prior to mechanical test using a CT X-Ray Inspection System (XT H 225, X-Tek Systems Ltd, UK, Figure 3-3) to acquire a series of images of the region of interest of the tibias. The μCT scanner is composed of a sealed micro focus X-ray tube with optional rotating target, real-time x-ray visualisation, fast CT reconstruction, CT measuring volume up to 250 mm and 600 mm height, 5-axis fully programmable part manipulator, customizable macros automate measurement workflow and small footprint and castors and roller for easy handling. The maximum weight of object that is capable of fitting into this device is 15 kg. The μCT system is capable of generating x-ray source at maximum 225 kV with small spot size of 3 μm to work with various range of sample sizes. A target was rotating during the x-ray scanning to ensure the heat was dissipated effectively and the object can be scanned in a short time to produce high resolution images. Using a rotating target, the electron beam falls on a moving instead of a fixed surface, which yields much more effective cooling. This offers the opportunity to measure objects faster, or denser objects with high accuracy.
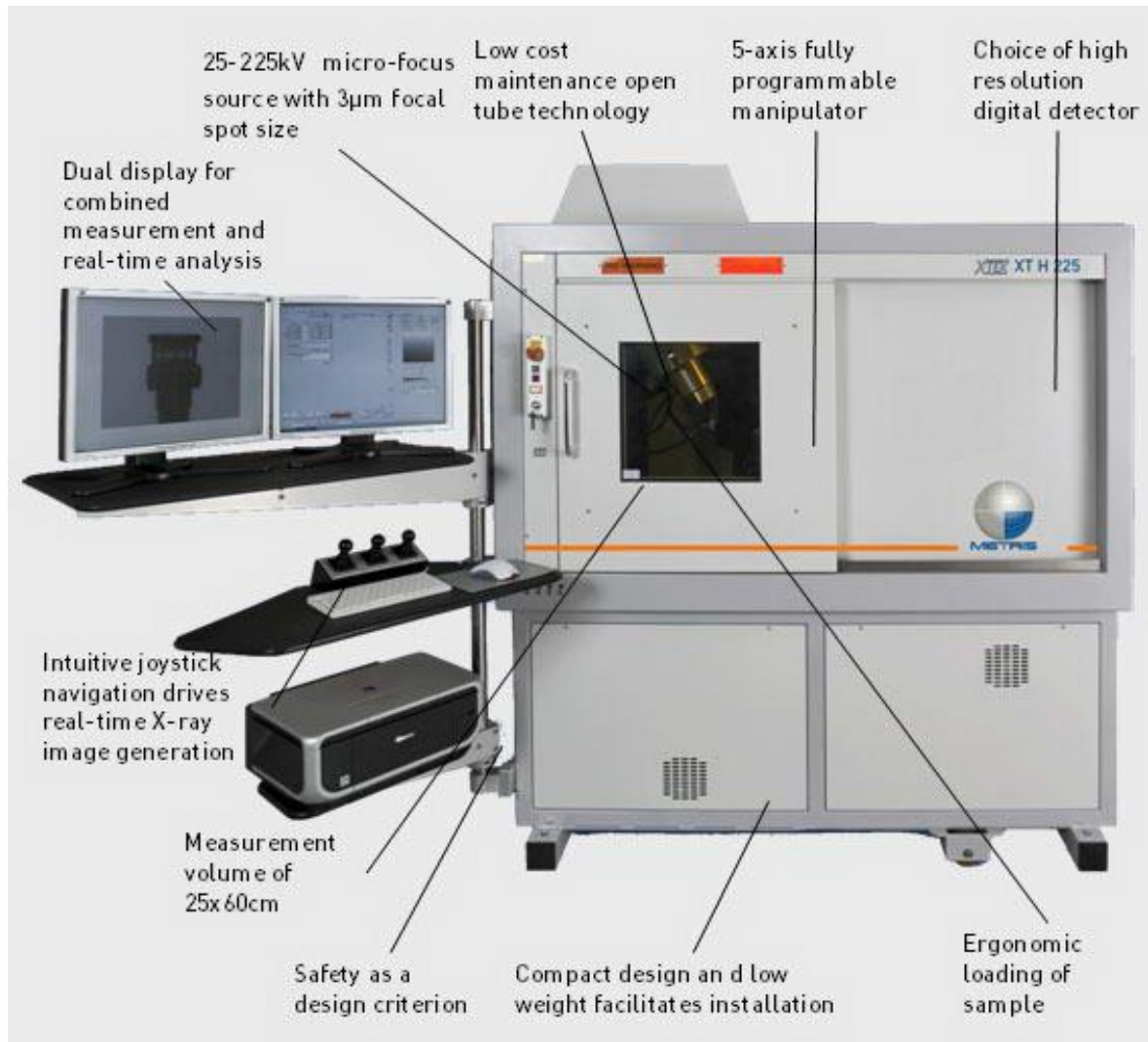
Figure 3-3 The µCT machine XT H 225 system used in this study (Adapted from www.nikonmetrology.com).

The tibia was positioned vertically and secured in a µCT holder to avoid any small movements during scanning (Figure 3-4). The tibia was positioned at the center of the holder between the detector and the x-ray source (Figure 3-5). The µCT image volume included the proximal and the distal tibia, though only proximal metaphyseal and midtibia were used in this analysis.
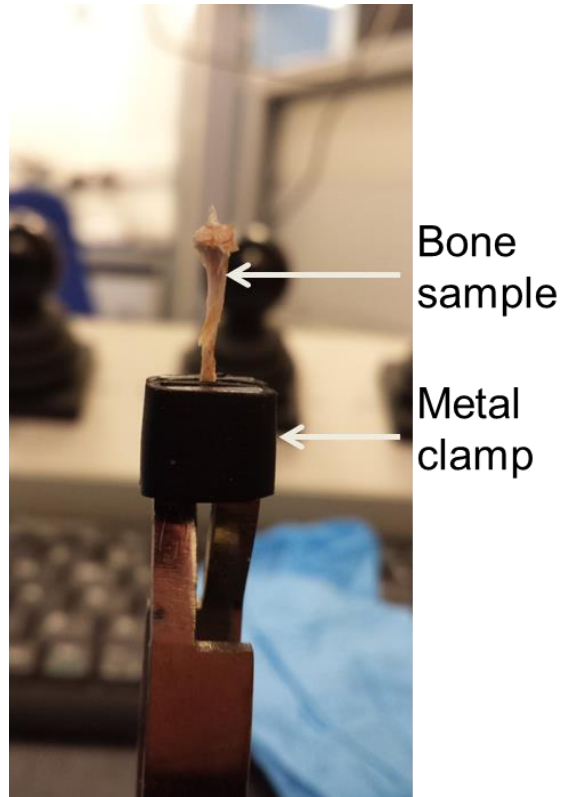
Figure 3-4 The position of the mouse tibia.
The mouse tibia secured in the holder to prevent movement during scanning therefore reducing motion artefacts.

μCT scanning parameters included: Bone reconstruction kernel, axial scanning plane, 50 - 55 kVp tube voltage, 95 - 300 μA tube current, voxel size = 6 - 8 μm, rotational step = 0.19°/360°. Full data acquisition of the tibia took about 90 minutes and the dataset was stored in a separate computer in the same network. The whole process of acquiring images, reconstruction and analysis requires a large dataset to be moved between the file servers and the different workstations used.   After the scanning finished, the projection images were loaded into the reconstruction program CTPRO (Metris X-Tek, UK). A reconstruction option includes beam hardening correction. The optimal settings need to be assessed empirically for mouse bone sample. Another option is smoothing, however, it was not activated to prevent impair detection of fine detail in the image. Ring artefact reduction is another correction option to reduce the motion artefact resulting

from the rotating sample. Figure 3-6 shows the regions of interest (ROI) selected for image evaluation. A destination folder was then chosen for the reconstructed images and the reconstruction started. These 3D image stacks were analysed using standard image analysis package available provided by the manufacturers of the µCT systems. Subsequently, the file extension .vgi (Volume Graphics Info file) was visualised using VG Studio Max 2.0 software (Volume Graphics, Heidelberg, Germany). The multiplanar reconstruction (MPR) method in the software was used to view the slice images. A volume of interest (VOI) was identified to contain a reasonable amount of trabecular and cortical bones.
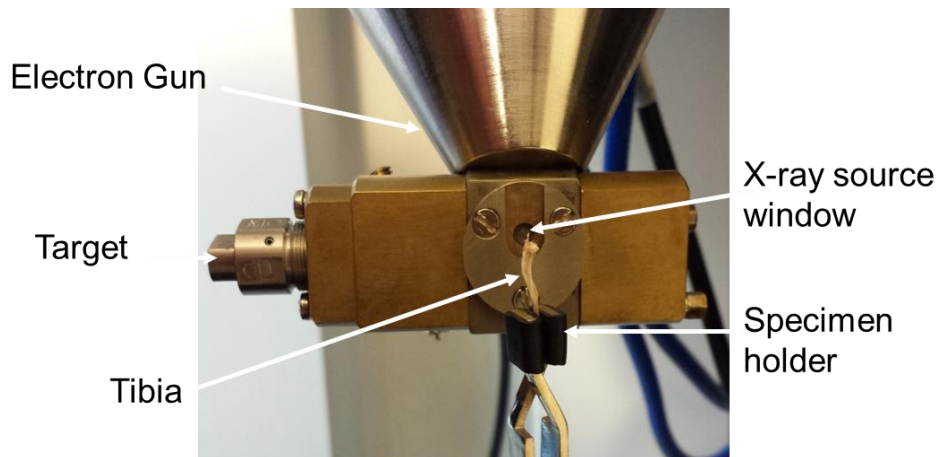
Figure 3-5 The arrangement of the tibia inside the µCT chamber.
The tibia was positioned close to the x-ray window sandwiched by the x-ray tube and the detector.

ImageJ was used to carefully select the proximal tibial metaphysis ROI 0.50 mm below the growth plate to avoid the primary spongiosa. The image stack for this region was 1.0 mm with 0.01 mm slice thickness. The ROI in midtibia consists of 0.54 mm thick of bone volume from 4.32 mm below the growth plate.
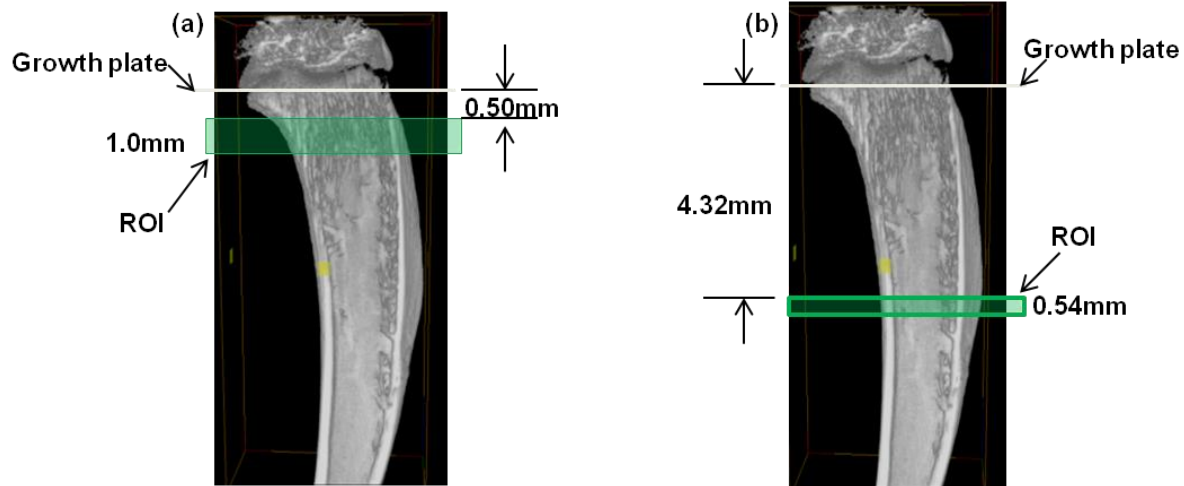
Figure 3-6 Regions of interest (ROI) studied in this work.
(a) proximal tibia metaphyseal; (b) midtibia.

3.4.1 Image Analysis

ImageJ

ImageJ (ImageJ v.1.46r, National Institutes of Health, USA) was used for the image analysis. At proximal metaphyseal tibia level, the whole bone ROI consists of bone marrow, trabecular bone and cortical bone; while at midtibia level, the ROI consists of bone marrow and cortical bone.

The quantification of cortical and trabecular bone morphometrics requires an accurate image processing method. The images were linearly rescaled to 0 and 255 to get 8-bit images and to avoid memory issues. The images were crop down to the minimum rectangle that contains the bone of interest. This limited the calculations of pixels inside the region of interest, and avoided processing the large image areas outside the sample to reduce the dataset size. Further, increasing the RAM to 6000 MB increased the ImageJ memory.

To quantify the cortical and the trabecular bone separately, image segmentation was carried out prior to bone parameter analysis. There are various image segmentation

methods (Buie et al., 2007; Janc et al., 2013). In this study, two methods were implemented to separate bone over the background; and the cortical bone over the trabecular bone. The methods are described in Section 3.4.3.

BoneJ

BoneJ (Version 1.3.8) was used throughout the bone image analysis process. BoneJ is made for bitmap data, and it uses a 7×7 median filter to reduce noise. The image was thresholded into binary images for further analysis using default setting in ImageJ. This setting was a variation of the IsoData Algorithm also known as iterative intermeans (Ridler and Calvard, 1978). Bone morphometry parameters were obtained from the BoneJ analysis. The parameter measurements used in this study are shown in Table 3-2 and Table 3- 3, as recommended by Bouxsein et al. (2010).

Table 3- 2 Cortical bone morphometry parameters (Refer to Section 3.4.3 for measurements).

Abbreviation	Variable	Description	Standard Unit
Tt.Ar	Total cross-sectional area	Total cross-sectional area inside the periosteal envelope using 'Slice geometry'.	mm^2
Ct.Ar	Cortical bone area	'Slice geometry' measure the cross-sectional area (CSA) of the bone pixels.	mm^2
Tt.Ar/ Ct.Ar	Cortical area fraction		%
Ct.Th	Cortical Thickness	Average cortical thickness	mm

Table 3- 3 Trabecular bone morphometry parameters (Refer to Section 3.4.3 for measurements).

Abbreviation	Variable	Description	Standard Unit
BV	Bone Volume	Volume of the entire region of interest	mm^3
TV	Total Volume	Volume of the entire region of interest(volume inside the periosteum)	mm^3
BV/TV	Bone Volume Fraction	Ratio of the segmented bone volume to the total volume of the region of interest	%
Tb.Th	Trabecular Thickness	Mean thickness of trabeculae, assessed using direct 3D methods	mm
Tb.Sp	Trabecular Spacing	Mean distance between trabeculae, assessed using direct 3D methods.	mm
Conn.D	Connectivity Density	A measure of the degree of connectivity of trabeculae normalised by TV	$1/mm^3$

3.4.2 Image Analysis

ImageJ was used for bone segmentation while the BoneJ plugin was used for the analyses of BV/TV (%), the bone thickness (mm), and the bone spacing (mm). 100 and 54 contiguous µCT slices were selected at the proximal tibial metapysis and midtibia, respectively. VOIs were identified in all genotypes which contain a reasonable amount of trabecular or cortical bones.

The bones (n=24) were analysed and the resulting microarchitectural indices were compared across the genotypes. The determination of the threshold level was based on visual inspection and automatic thresholding (revised IsoData algorithm) (Bouxsein et al., 2010; Stock, 2009) using the reference image (original gray-scale image) (Bouxsein et al., 2010). The images were then rescaled to 0 and 255 to get 8-bit images (Bayat et al., 2005). The images contain the information of the maximum (255) and the minimum (0) values of a pixel. It can store 256 different level of intensity (2^8 = 256). The more bits per pixel an image uses, the more intensity levels can be stored. However, the image will need more disk memory space (Mateos-Perez and Pascau, 2013).

Reducing the bit depth of the images retain the small features of the samples. This will reduce the size of the image and make the segmentation step easier with regard to lower memory requirements and reduced amount of pixels to process. Another step is cropping the images in order to keep the necessary objects within the volume limits. This will limit the algorithm to calculate within the pixels of the ROIs.

After thresholding was performed images were further cleaned by removing small fragments. Trabecular bones are highly connected structure, therefore any unconnected small objects are unlikely to be bone and can be removed using despeckle operator. Volksmann's canals or tubular passages that perforate the surfaces of the cortex must be removed using morphological operations, where dilation followed by erosion was implemented prior to extraction.

3.4.3 Image Analysis using Semi-automatic Segmentation.

Semi-automatic segmentation procedure was employed in this study. This procedure involved manually selecting and drawing the trabecular regions slice by slice. This is followed by thresholding and measuring the bone pixels.

3.4.3.1 Cortical bone

1. Calculating Total Cross-sectional Area (Tt.Ar)

The cortical bone images were analysed using 'Slice Geometry' plugin. It calculates cross-sectional geometric properties of shapes: cross-sectional area, centroid, mean density, second moment of area, section modulus, Feret diameter and local thickness (2D and 3D) (www.bonej.org/slicegeometry). Measurements can be made prior thresholding the images into binary images. To improve the performance of the algorithm measurement, a rectangular ROI was drawn around the cross-sectional cortical bone to limit the calculation of cross-section geometry to pixels inside ROIs.
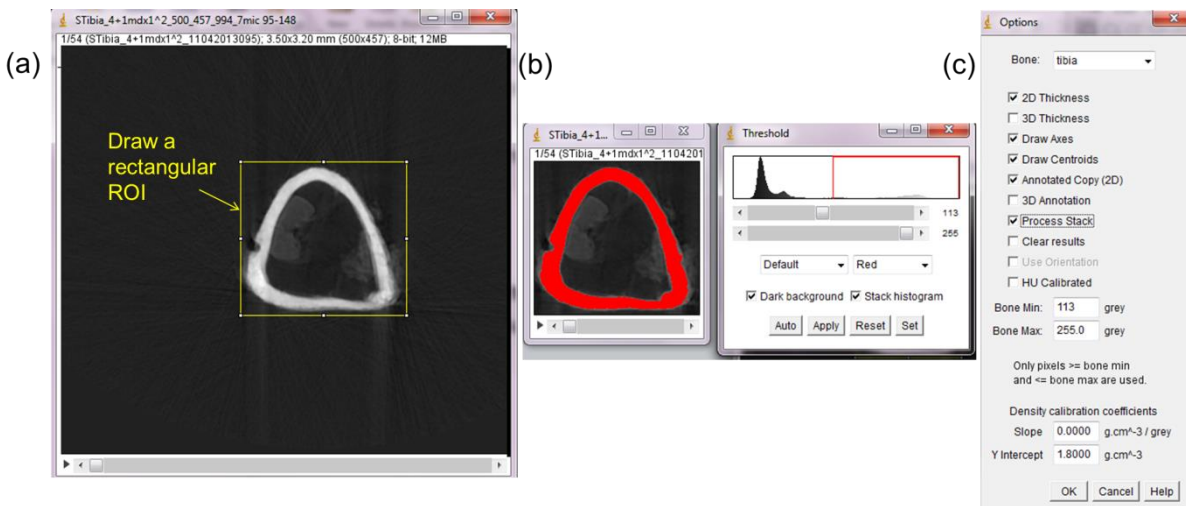
Figure 3-7 A sequence of analysis using 'Slice Geometry' option.
(a) A rectangle shape was drawn to limit the ROI measured, (b) The process of binarisation (thresholding) followed by despeckle & morphological operators, (c) 'Slice Geometry' options. Note that density-weighted calculations are only applied to centroid determination present.

The sequence of the analysis is:

1. Draw a rectangular ROI to include the cross-sectional cortical bone.
2. Convert stack of images into 8-bits and threshold them into binary input.
3. Run the 'Slice Geometry'.

2. Calculating Cortical Bone Area (Ct.Ar)

As recommended in Bouxsein's guidelines, cortical bone area was calculated by using cortical volume (Ct.V) ÷ (number of slices × slice thickness). However, using BoneJ, 'Slice Geometry' plugin was used to determine the cross-sectional area of the midtibia. The plugin calculates the Ct.Ar in transverse plane. Prior to that, the images were converted into 8-bits, segmented, cleaned and then 'Slice Geometry' was used. The plugin scanned the rectangular ROI and count pixels that are above minimum and below bone maximum then multiplies by pixel area. The minimum and maximum bone values were determined during the thresholding.

3. Calculating Cortical Thickness

'Thickness' plugin was used to obtain the mean and standard deviation of the cortical thickness. It uses pixel values in the resulting thickness map. The algorithm makes a sphere fitting or voxelic spheres which are voxel/pixel size. The image resolution is reduced so that each pixel is resolved by fewer, larger pixels. 'Thickness' was selected to calculate the cortical thickness based on the pixels selected.

3.4.3.2 Trabecular bone

The trabecular bone was selected manually as an irregular anatomic contour adjacent to the endocortical surface or an irregular anatomic contour a few pixels away from endocortical boundary, as suggested in Bouxsein et al. (2010). This method was used for all image slices. The ROIs were then added to the ROI manager. This allows only the selected pixels in the ROI contribute to the BV/TV measurement. The same steps were applied to the other parameters. The pixel values were managed carefully because the ImageJ default known as black is 0 and white is 255, where 255 is 'foreground' and 0 is 'background'. BoneJ treats 255 as bone and 0 as non-bone.

The validation of individual threshold values was done by setting up a gold standard threshold manually and then tested whether the automatic procedure discovers a value that is suitably close.

To restrict the BV/TV measurement to the relevant ROIs, ROI Manager option was selected to instruct the plugin to use the ROIs that were added previously.
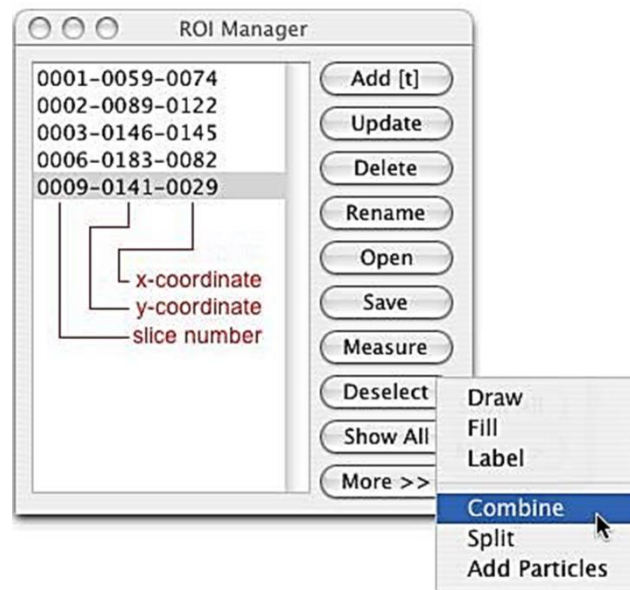
Figure 3-8 The Region of Interest (ROI) manager.
The ROI manager creates a three part label. The first part (image in stacks) is the slice number, the second is the y-coordinate of the selection and the third is the x-coordinate (Adapted from imagej.nih.gov).

The sequence of the analysis is:

1. Open the stack of images.
2. The ROIs were drawn manually slice-by-slice using the freehand selections adjacent to the endocortical surface, as described in Bouxsein et al. (2010).
3. The BoneJ plugin was run (Plugins>BoneJ>Fit Sphere), clearing the ROI manager of the point ROIs and adding the sphere ROIs (set of circles) to the ROI Manager.
4. Click Add to add the current selection to the list, or press't', the keyboard shortcut for the Edit>Selection>Add to Manager command.
5. The image threshold was adjusted (the pixels of interest are masked in 'red')
6. The plugin was run again (Plugins>BoneJ>Volume Fraction) by selecting the measurements to calculate the ROIs (i.e Thickness). The selection was restricted to ROIs.

1. *Interpolating ROIs*

A common segmentation approach is to draw ROIs on every slice in a stack, which put together define a 3D ROI. Interpolate ROIs (Plugins > Stacks > Interpolate ROIs) uses the signed integer transform to interpolate between ROIs. The selected trabecular bones were interpolated using 'Interpolate ROIs'. The trabecular region was first drawn as close to the endosteum as possible, a few voxels away from endocortical boundary. The selected region was then added into the ROI manager. These steps were repeated by advancing a few more slices (5-10 slices) depending on the details in the image. The steps were repeated until all image stacks were analysed.

2. *Thresholding*

The acquired μCT images consist of a range of phase contrasts corresponding to different levels of x-ray absorption (Figure 3-9). For subsequent computational analysis, ROI within the field of view can be segmented using a thresholding technique. This technique involved the process of replacing the voxel values of features of interest with a binary value of 1(solid) and 0 (non-solid). In ImageJ, the voxel values are replaced

with 0 (ignore black) and 255 (ignore white) grey levels. The white object will be set on black background. The thresholding technique can be implemented in two ways: local thresholding and global thresholding. Both plugins are able to automatically process binary images. Auto local thresholding can work with 8-bit images whilst auto global thresholding can work with both 8- and 16-bit images. The bit depth of an image provides information of the minimum and maximum values of a pixel and it directly corresponds to the resolution of each pixel. Global thresholding was applied in this study.
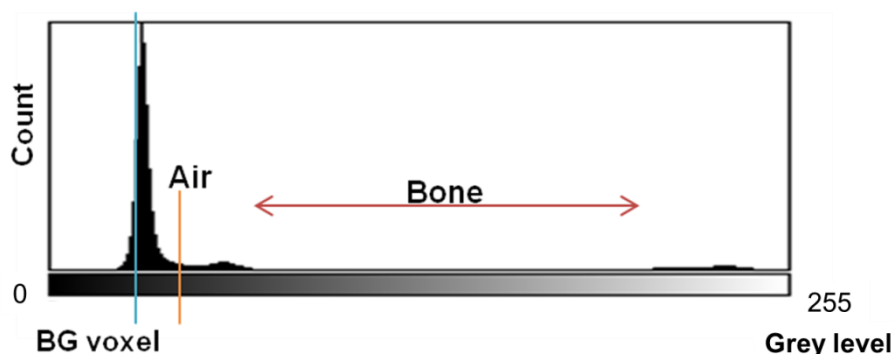
Figure 3-9 The histogram of a typical 8-bit 3D CT image of tibia.
The left peak represents background (BG) voxels, the middle peak represents air voxels, whereas the right peak represents bone voxels.

After identifying the features of interest, the images were thresholded using the stack histogram in which the histogram of all the slices will be computed. The images were thresholded based on the histogram and all the slices are binaries with a single value. There are 16 available methods listed in the thresholding option in ImageJ. In this study, the default method was chosen to segment the bone and non-bone regions as well as cortical and trabecular bone. This method is a variation of the IsoData algorithm (Ridler and Calvard, 1978; Doube et al., 2011), which works by choosing the optimum threshold automatically based on an iterative process.

Due to the absence of a well-defined valley between the histogram peaks, visual inspection was used to facilitate the thresholding and the segmentation (Stock, 2009).

3.4.3.2(a) Trabecular Thickness (Tb.Th) and Spacing (Tb.Sp)

Thickness plugin was used in the study where the plugin defines the thickness at a point of the strut, which is the diameter of the greatest sphere that fits within the structure which contains the point. Then it is calibrated by multiplying with pixel spacing. BoneJ is expected to work with isotropic pixel spacing. For trabecular bone, when the ROIs were selected and added in the ROI Manager, the trabecular thickness (Tb.Th) and trabecular spacing (Tb.Sp) were assessed. Trabecular spacing is the local thickness of the marrow space in between trabeculae. The Tb.Sp at a point in the structure is defined by the diameter of the largest sphere that fits within the marrow and that contains the point. BoneJ reports a mean Tb.Sp as an arithmetic mean of the pointwise Tb.Sp values. It is a similar process for Tb.Th.

3.4.3.2(b) Structural Model Index (SMI)

SMI is a standard measurement for the determination of plateness and rodness of trabecular structures. SMI was assessed using the binaries voxel images (input). In BoneJ, there are two methods to implement: surface mesh dilation (Hildebrand and Ruegsegger, 1997) and voxel dilation (Dilate 3D). Surface mesh dilation method is preferred whereas voxel dilation is implemented in CTAn (bonej.org/smi). However, preliminary analysis shows mostly positive values (convex, SMI+), which could not possibly be true. Recent findings from Salmon et al. (2015) showed that SMI does not measure the bone plateness and rodness accurately. Hence although the parameter was considered in the study, the result has been removed from reporting.

3.4.3.2(c) Connectivity

The number of connected structures in a network and its connectivity density (Conn.D) was calculated using the connectivity algorithm in BoneJ. It uses voxel neighbourhoods to calculate the Euler characteristic of the volume and adjusts this to give the contribution of the volume to the connectivity of the structure it was cut from. Essentially, Conn.D is a count of topological holes in the structure (Doube et al., 2010; Toriwaki and Yonekura, 2002). Prior to Connectivity calculation, Purify was selected in

BoneJ to remove any artefacts in the images with an assumption that there is only one particle in the foreground. Results are reported based on the standard report by Parfitt et al. (1987) and guidelines by Bouxsein (2010).

$$\beta_1 = 1 - \Delta\chi \tag{3-1}$$

$$\text{Conn.D} = \frac{\beta_1}{\text{Stack Volume}} \tag{3-2}$$

Where β_1 is the connectivity of the image (number of trabeculae) and $\Delta\chi$ is the bone sample's contribution to the Euler characteristic of the bone it was connected to. The connectivity density (Conn.D) is the connectivity per unit volume (number of trabeculae per unit volume).

Connectivity used a topological approach. Connectivity density (Conn.D) as in Equation 3-2 is better than Connectivity as the latter makes assumptions about the underlying geometry which may or may not be correct. Connectivity measures loops rather than branches. A tree would be seen by Connectivity as having only one 'trabeculae' because there are no loops. For trabecular bone, measurement of Connectivity is relevant because bone is a single continuum perforated by a continuous marrow space and so counting loops gives an indication of its trabecular number.

Connectivity is influenced by noise, so smoothing or using noise-reduction approaches (Gaussian blurring or 3D erode-dilate) the structure before running the analysis is necessary to reduce the spurious, small branches or loops.

3.5 Three-point bending test

The bending test (Hessle et al., 2013) was done in Mechanical Behaviour and Material Laboratory, University of Portsmouth, UK. The aim of the study was to analyse the biomechanical properties of bones in the three genotypes compared to the wild-type; in particular to examine the impact on bone strength in knockout mice compared with that of *mdx* mice.
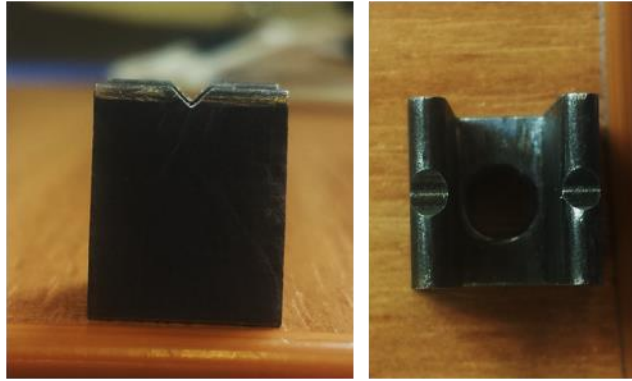
Figure 3-10 V-shaped end supports.
The lower supports were shaped in such a way to prevent movement of the specimens in all planes during loading.

Left tibias were mechanically tested under three-point bending using a Bose ElectroForce® 3200 until failure. The bending jig was custom-made, where both end support was cut in a v-shape to provide stability, as shown in Figure 3-10. The tibias were placed horizontally on the lower supports, at a span of 7 mm (Silva et al., 2004) with the anterior surface of the tibia was facing upwards. The load was applied on the midshaft of the tibia. The force was measured with a 225 N capacity load cell calibrated in the full load range according to ISO 7500-1:2004 class 0.5.

Each bone sample was compressed with a constant displacement rate of 0.155 mm/s until failure (Figure 3-11). The average time for the test was approximately 5 to 10s. The load and displacement curves were obtained and stored in a computer coupled to the testing machine. The peak load was recorded by measuring the maximum force that the bone was able to resist. Stiffness characterises how much the bone deforms when loaded. It was calculated by measuring the slope of the most linear portion of the elastic region of the load-displacement curve. Flexural modulus was determined from the slope of the stress-strain curve of a material under bending load. The work-to-fracture defined by the area under the load-displacement curve was calculated by using OriginPro 9 64-bit. Cross-sectional area and shape are assumed constant at the loading point.
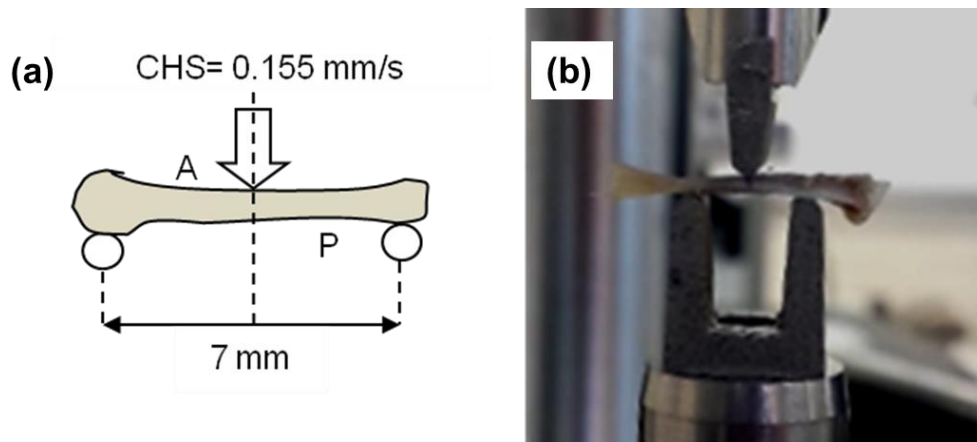
Figure 3-11 The three-point-bending test arrangements.
(a) Tibia was placed on the lower supports, with anterior surface facing up. Load was applied in the midplane until failure. (b) The force was measured with a 225 N capacity load cell calibrated in the full load range according to ISO 7500-1:2004 class 0.5.

3.5.1 Calculations of the Second Moment of Area

Cross-sectional second moment of area (SMA) is the morphological parameter that correlates strongly with bending stiffness. SMA reflects both the amount of mass and the spatial distribution of the mass. The SMA in the loading direction (anterior-posterior) was calculated using the algorithm in BoneJ, where the two orthogonal axes, anterior-posterior and medial-lateral, intersect at the centroid. An average value of SMA was obtained from the values calculated from 20 slices taken in an area close to the load application.

BoneJ protocols

The SMA was calculated from a digitised bone cross-section obtained from a μCT scan (Jepsen et al., 2015; Sharir et al., 2008). 'Slice geometry' plugin in BoneJ was used to calculate cross-sectional geometric properties of shapes including cross-sectional area,

centroid, and second moment of area (SMA), considering the cortex is approximately cylindrical and the cross-section is orthogonal to its long axis.

The pixels that contribute to the calculation of second moment of area are those pixels that lie within the ROIs. The minimum and maximum cortical bone pixel values were determined by the image threshold.

Orientation

This plugin was used to set the direction of the principal axis in a 2D image. Slice geometry uses orientation to calculate second moment of area. The orientations of the principal axes were set as in Figure 3-12.
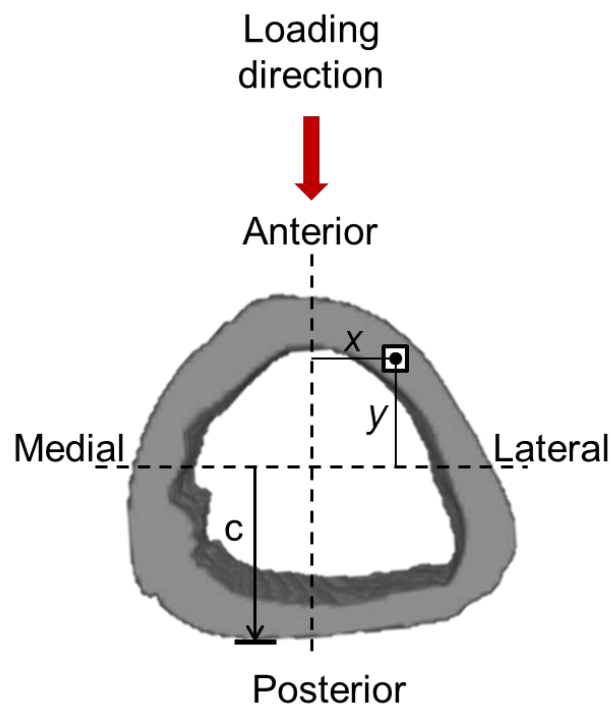
Figure 3-12 Schematic diagram of a cross section of bone.
The figure shows the loading direction anterior-posterior orthogonal to medial-lateral axes, with a pixel at a distance x and y. 'c' is the distance measured from the centroid to the edge of the cross-section in tension (Adapted from Jepsen et al. 2015).

Slice Geometry

Slice geometry was used for the analysis. This plugin returns the maximum chord distance from the centroid of the cross-section to the edge of the cross-section in tension for each slice. The algorithm can be used for every slice and slice-specific results obtained. The SMA (I) about the maximum I_{max} and minimum I_{min} were provided automatically in the BoneJ analysis output.

Validation of the method was carried out using a rectangular shape, as illustrated in Figure 3-13.

a)   b)
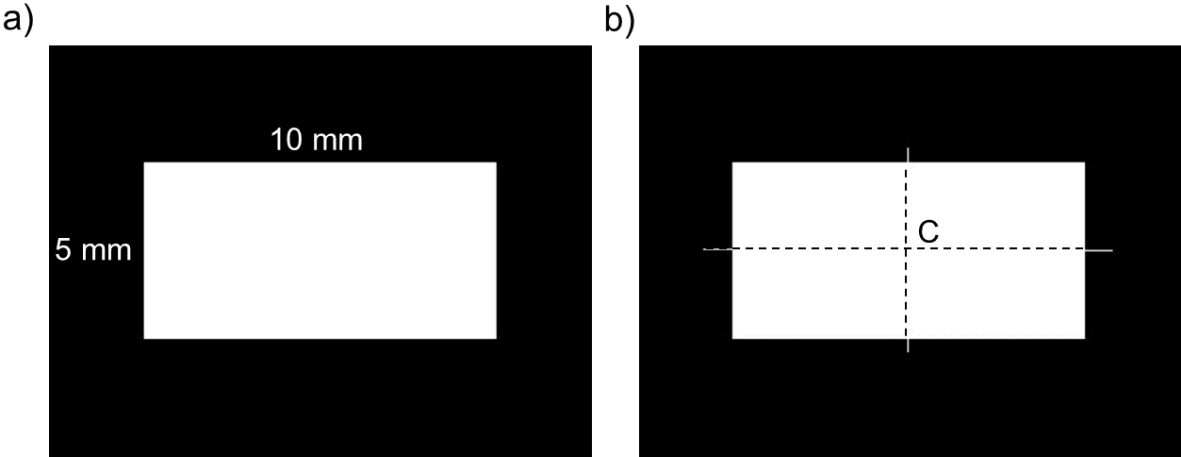
Figure 3-13 Validation test of a known shape.
(a) The image of an arbitray rectangular shape (b, width=10 mm; h, height=5 mm) was modelled to validate the SMA calculation by running the algorithm in ImageJ using Slice Geometry plugin. b) The annotated image showing the principal axes with centroid C marked.

The maximum I_{max} and minimum I_{min} were calculated using the Equation 3-3 and Equation 3-4. Both results from BoneJ and theory of elasticity for the case presented in Fig 3-13 are given in Table 3-4, showing good agreement.

$$I_{max}=\frac{b^3h}{12}$$ 3-3

$$I_{min} = \frac{h^3 b}{12}$$ 3-4

Table 3-4 A comparison of SMA calculations between the theory and BoneJ algorithm for the rectangular shape in Figure 3-13.

	Theory	BoneJ
I_{max} (mm^4)	416.67	419.601
I_{min} (mm^4)	104.17	104.900

3.5.2 Stress and strain

Stress and strain curves were obtained from the load-displacement curves, where the load was converted to stress and displacement was converted to strain using Equation 3-5 and Equation 3-6 (Jepsen et al., 2015; Nakagaki et al., 2011).

$$\sigma = F\left(\frac{Lc}{4I}\right)$$ 3-5

$$\varepsilon = d\left(\frac{12c}{L^2}\right)$$ 3-6

where σ is the stress, F is the load, L is the length of the span, c is the distance from the centroid of the cross-section to the edge of the cross-section in tension, I is the SMA in the loading direction, ε is the strain, and d is the displacement. The flexural strength and strain at failure were obtained from the stress-strain curves.

The parameter 'c' was measured using 'Slice Geometry' algorithm as the maximum distance from the centroid of the cross-section to the edge of the cross-section in tension for each slice. An average value was obtained from the data of 20 slices taken in an area close to the load application.

3.6 Scanning Electron Microscopy

The epiphyseal region of the left distal tibia (n=2) of the four genotypes was selected to examine the fracture surfaces post three-point bending testing using Scanning Electron Microscopy (SEM). The SEM was carried out with compatible digitiser at the Environmental Microbiology Laboratory, University of Portsmouth, UK (JSM-6060LV JEOL, Tokyo, Japan).

3.6.1 Sample preparation and methodology for SEM

The distal part of left tibia per bone per genotype was placed horizontally on the specimen support. The tibias were air-dried and gold-palladium-coated before scanning (Bozzola and Russel, 1999). Coating was carried out using a sputter coater (Quorum Model Q150R ES). The coated tibias were stored in a dust-free desiccator, before placed in the SEM chamber for observation. The SEM was operated at 15kV accelerating voltage. SEM images of the fracture surface were captured and compared at magnifications from 10 to 500 μm to enable the analysis at both macro and micro levels.

3.7 Nanoindentation

Nanoindentation was performed at the Forensic Laboratory, University of Cranfield, UK, using a CSM-Nano Hardness Tester System with Indentation v.3.83 software (CSM Instruments SA; 2034 Peseux, Switzerland) (Figure 3-14). A typical Berkovich (three-sided pyramid) triangular-based pyramid diamond indenter was utilised with optical microscope 5x,100x, Nikon (4000x CCD camera). The machine is operated at a load range 0.1-500nm. Geometrically, it has a tip with less than 20 nm tip radius, following the ISO4577-1:2015 standard. The bone preparation followed the procedures described in (Finnilä et al., 2010; Herlin et al., 2013; Zioupos and Rogers, 2006)

In this study, the transverse cortical bone tissue properties from the proximal and midtibia were measured. In the preliminary step, the hardness and elasticity of the bone structure of different locations, particularly the cortical regions (medial, lateral, anterior

and posterior), were investigated to evaluate the variation and to guide the selection of the location of the nanoindentation points.
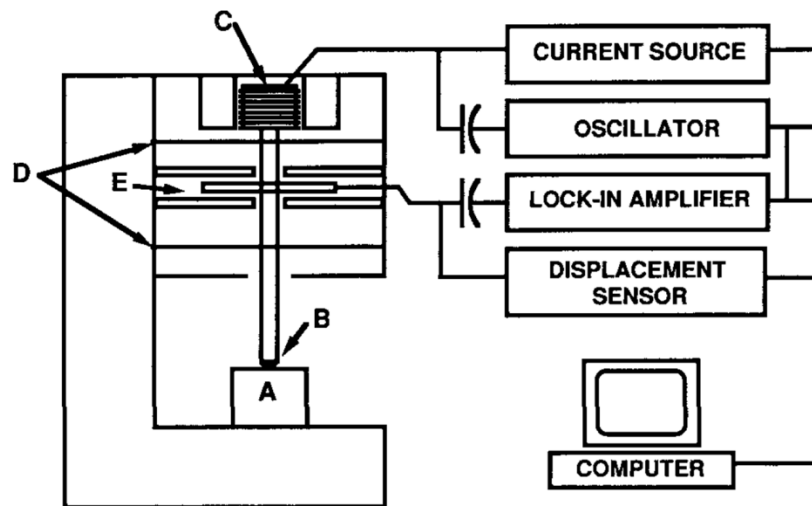
Figure 3-14 Schematic illustration of a nanoindentation.
A schematic representation of the experimental apparatus used to perform the indentation experiments: (A) sample, (B) indenter, (C) load application coil, (D) indentation column guide springs, (E) capacitive displacement sensor (Oliver and Pharr, 1992).

3.7.1 Sample preparation

The left tibia diaphysis from the mice was cut transversely at the midpoint of each tibia shaft using a diamond saw. They were stored in plastic vials and labelled. The fracture fragments from three-point bending test consist of both the top and bottom part of the tibia. Proximal midtibia sections were used for the nanoindentation test. The upper section consists of proximal metaphyseal tibia with trabecular bone in place while the bottom section, the midtibia part, consists mainly of cortical bone. The system used and the positions of the indenter and the sample were shown in Figure 3-15.
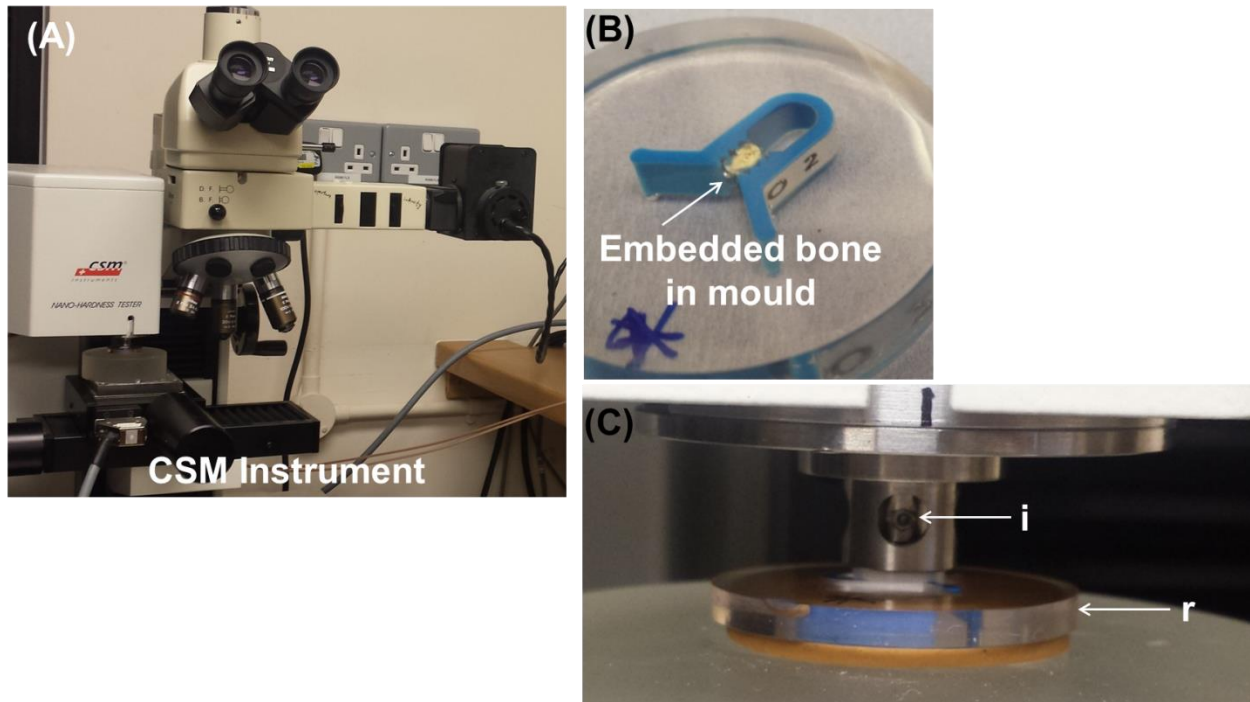
Figure 3-15 Nanoindentation test for advanced and sinus protocols.
(A) The nanoindentation setup showing (A) CSM Instrument Nano-Hardness Tester machine. (B) The bone tissue (white arrow) embedded in a resin with clipper in placed, (C) The resin (r) was placed under the nano-indenter (i) where a piece of clay was used to secure its place on the stage.

The bones were cleaned with distilled water, ultrasonicated and left air-dried in a desiccator at room temperature. The tibias were then embedded in low viscosity Kleer-Set resin (MetPrep, Conventry, UK). The moulds were then allowed to solidify at room temperature for 24 hours. The bone cross-section surface was subsequently ground using silicon carbide papers with decreasing grain size; midtibia (400, 500, 800, 1200 grit) and proximal metaphyseal tibia (2500 and 4000 grit) using running water as lubricant with semi-automatic grinder. The final step was polishing the bone surface using a 0.05 micron γ-alumina slurry (MetPrep Conventry, UK) (Zioupos and Rogers, 2006).

For trabecular samples, the proximal part of the tibia was cut before embedding to remove the condylar part with growth plate. To remove the bone marrow, the bone was ultrasonicated in Phosphate-Buffered Saline (PBS). To make sure the individual trabeculae was well supported, the medullar space was injected with low viscosity superglue into the pores in the trabecular network left unfilled by the Kleer-set resin.

The bone surface must be flat and clean as well as free of dust and adhesive particles that can contaminate the measurement and the indentation tip. The surface of the bone cross-section was examined closely for smoothness using the optical microscope. Subsequently, the bone surface was air-dried for 24 hours. The indentation targets were carefully selected in the centre of the intended bone tissue using an optical microscope (Zhang et al., 2015).

3.7.2 Machine preparation

3.7.2.1 Indenter-Microscope Distance Calibration

The machine was calibrated every morning before testing and in between measurements. In this study, the distance calibration was done between the indentation measurements taken for each of the trabecular bone sample. This would help to precisely locate the small trabeculae struts measured approximately less than 20 μm as compared to that of human which measured approximately 50 μm (Hamed et al., 2012).

3.7.2.2 Adjust Depth Offset (ADO)

ADO is an indent made prior to the experiment. The procedure was performed on the sample topology for each new measurement. The offset value set by the software will ensure a correct position of the depth sensor of the instrument due to vertical variation between the indenter and the reference, as well as to optimize measurement duration (Figure 3-16; Indentation software manual, DCOM 70050). It is a reference point to ensure all indents occur at a similar level.
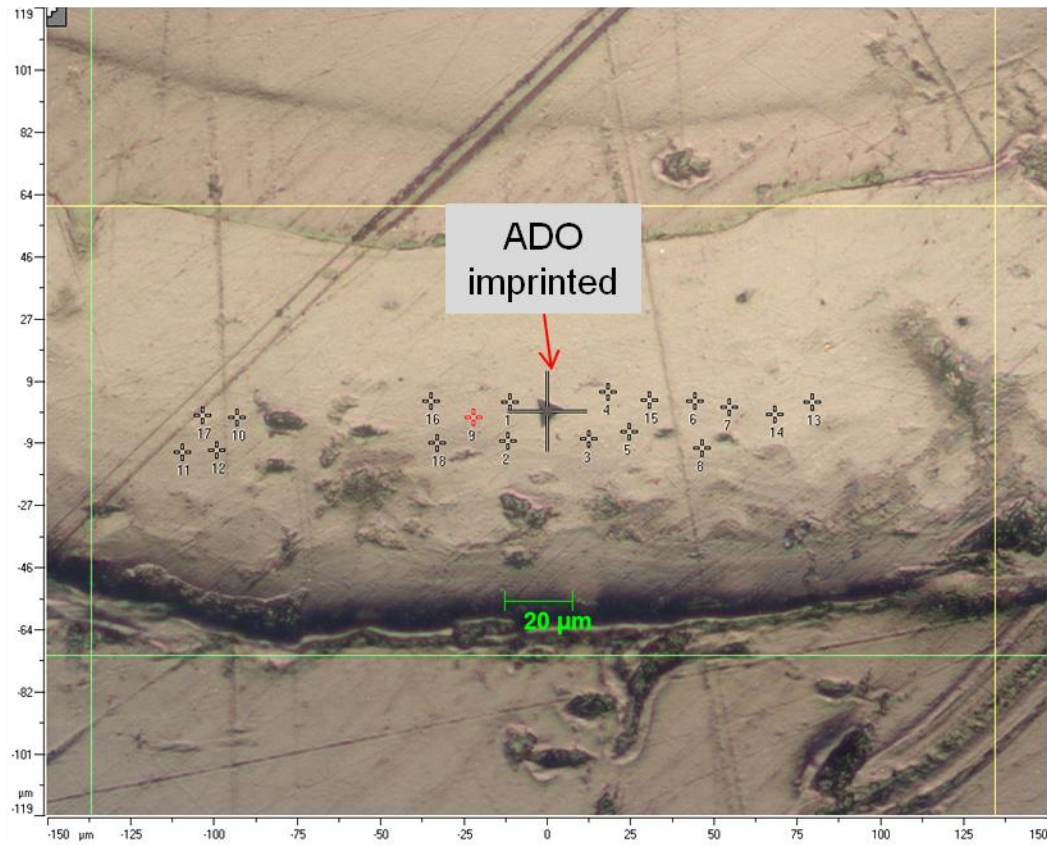
Figure 3-16 A micrograph of a cortical bone sample.
The figure shows ADO imprinted on the bone surface prior to the measurements (numbered indentation points). The cross hair was centered on the imprint point to bring the video camera in the center of the bone topology under measurement.

3.7.3 Nanoindentation Systems

Nanoindentation is capable of performing four operations: (1) apply load (or displacement), (2) measure displacement (or load) with very high accuracy, resolution and precision; (3) position and perform indentations at any desired location on a sample, and (4) interpret load and displacement data to obtain hardness, elastic modulus, adhesion force, fracture toughness, and other mechanical properties (Malshe et al., 2010).
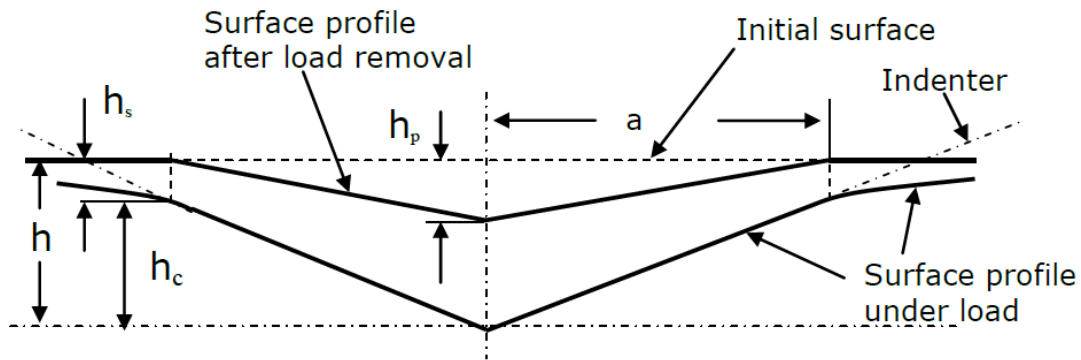
Figure 3-17 The schematic representation of the Berkovich indenter head and sample contact (Oliver and Pharr, 2004)**.** h_p is the permanent indentation depth; h_s is the amount of sink-in at contact periphery, where $h_s = \in \frac{F_{max}}{S}$; h_r is the tangent indentation depth, where $h_r = h_{max} - \frac{F_{max}}{S}$; h_c is the contact indentation depth, where $h_r = h_{max} - \varepsilon(h_{max} - h_r)$.

Figure 3-17 shows the indenter profile before and after removal of load from the object being tested. In a typical nanoindentation test, a tip or indenter, typically made of diamond, is pressed into the test sample with a known load followed by an intermediate holding period if necessary. After some time when the load is removed, the area of the projected residual indentation in the sample is measured (Malshe et al., 2010). Most experiments were performed using a load-displacement sequence like that shown in Figure 3-18.
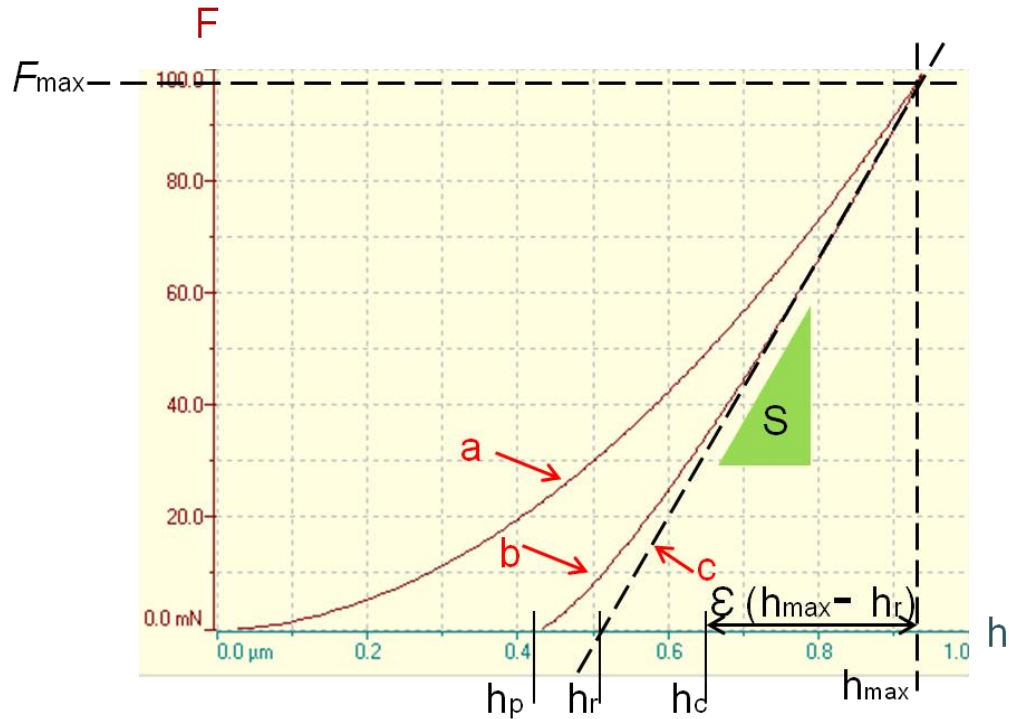
Figure 3-18 A typical nanoindentation curve with corresponding parameters presented in this study.
'a' is application of load phase, 'b' is removal of load, 'c' is tangent to curve 'b' at F_{max}(maximum load), h_p is permanent indentation depth, h_r is tangent indentation depth, h_c is contact indentation depth, h_{max} is maximum indentation depth at F_{max}, 'S' is stiffness, ε is geometric constant (Adapted from the DCOM 70050 Indentation manual).

The area function of the tip of the indenter was defined based on the calibrated diamond indenter by using a series of 110 indentations at different loads and was approximated by a polynomial function of the contact depth (Finnilä et al., 2010; Zioupos and Rogers, 2006) :

$$A_p(h_c) = 24.5h_c^2 + \sum_{n=0}^{5} C_n - h_c^{1/2^n} \qquad 3\text{-}7$$

where A_p is the projected contact area, h_c is the contact depth and C_n is the constant determined by the curve fitting. The hardness and indentation modulus were measured following Oliver and Pharr (1992). The hardness is determined at the end of the hold

phase (Equation 3-8). The contact stiffness is calculated from the unloading phase data as the near maximum load derivative of a power law fitted polynomial in between 98% and 40% of F_{max}. Further, the parameters measured from the curves are F_{max} (maximum load), h_m (maximum displacement), h_c (contact depth), A_p (projected contact area), and S (contact stiffness) (Figure 3-18). The reduced modulus defined in Equation 3-9 used contact stiffness, S, projected contact area, A_p and indenter geometric constant. E_r is used to calculate the indentation modulus, E_{IT} as in Equation 3-10.

$$H_{IT} = \frac{F_{max}}{A_p(h_c)}$$
3-8

where F_{max} is the maximum load imposed on the surface of the bone and $A_p(h_c)$ is the projected contact area between the indenter and the specimen. It was determined through indenter calibration using series of 110 indentations.

$$E_r = \frac{\sqrt{\pi}}{2\beta} \frac{S}{\sqrt{A_p(h_c)}}$$
3-9

Where β is the indenter geometric constant ($\beta=1.034$) and the contact stiffness, S (dF/dh) is calculated from the unloading phase.

$$E_{IT} = \left[\frac{1}{E_r} - \frac{1-v_i^2}{E_i}\right]^{-1} \cdot (1-v_s^2)$$
3-10

where E_{IT} is indentation modulus and E_r is reduced modulus while i and s subscripts corresponding to the indenter and the sample, respectively. While v is Poisson's ratio. The elastic modulus (E_i) and Poisson's ratio of the diamond indenting are 1141 GPa and 0.07, respectively.

Prior to each indentation, the bone surface topography was examined so that the indenter was accurately placed on the point of interest on the bone, as represented in Figure 3-19. Typically, the parameters that can be extracted from the load-displacement curves are Hardness (H_{IT}), Indentation Modulus (E_{IT}) and Creep (C_{IT}). Firstly, the hardness was computed as in Equation 3-8.
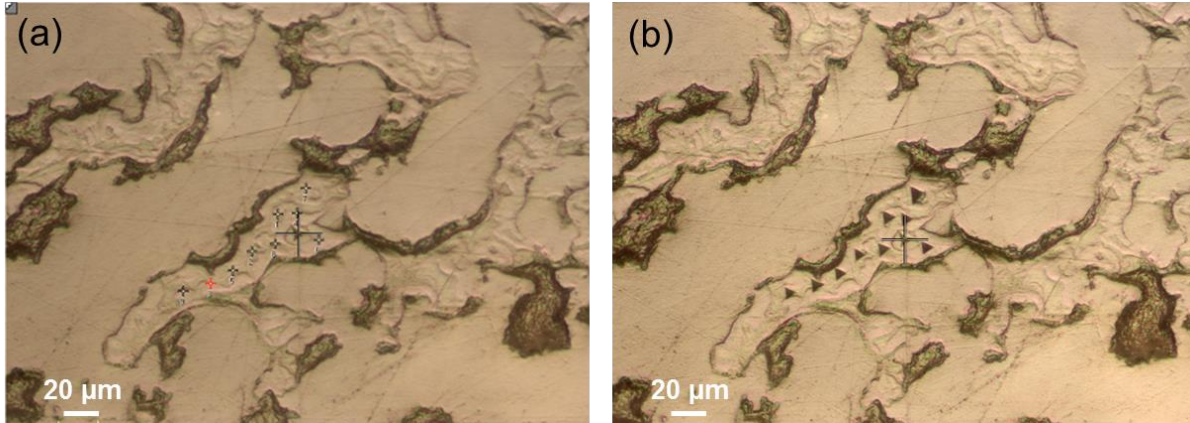
Figure 3-19 The micrographs showing indentations of a typical trabecular bone of a WT mouse.
(a) The indentation marks were placed prior to indentation to ensure that impression was accurately placed on the bone tissue. The cross hair is in the centre of the micrograph. (b) The impressions made on the bone tissue after the indentation procedure.

The Indentation Modulus (E_{IT}) was computed after the Reduced Indentation Modulus (E_r) was determined as in Equation 3-9. The E_r represents the elastic deformation that occurs in sample or in indenter tip.

Creep is an increase in depth at constant F as a function of time. It is a time-dependant deformation. To measure creep, the maximum load was hold for a given duration allowing sample relaxation, as in Equation 3-11.

$$C_{IT} = \frac{h_2 - h_1}{h_1} \cdot 100$$

3-11

where h_1 and h_2 are the indentation depths at t_1 and t_2, respectively (Figure 3-20). The protocols are defined in Table 3-5 and Table 3-6.
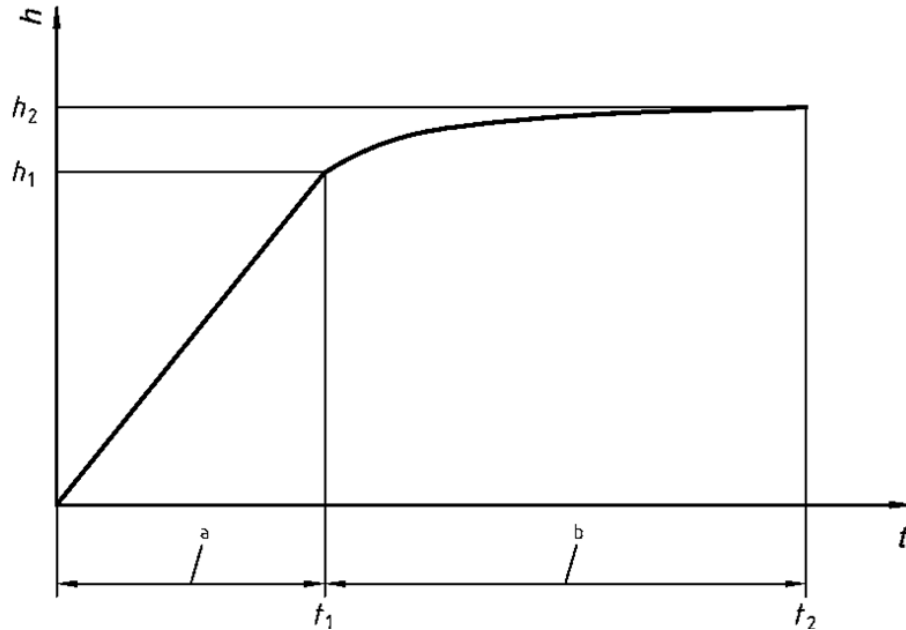
Figure 3-20 Expression of creep. Y-axis represents the indentation depth and X-axis represents the time, whilst 'a' is application of load phase and 'b' is removal of load.

Table 3-5 The advanced measurement parameters and settings.

Advanced Protocol	Cortical	Trabecular
Maximum load (mN)	10	10
Loading rate (mN/min)	20	20
Unloading rate (mN/min)	20	20
Pause (s)	30	30

Table 3-6 The sinus measurement parameters as well as sinus settings in the software.

Sinus Protocol	Cortical	Trabecular
Maximum load (mN)	10	10
Loading rate (mN/min)	10	10
Unloading rate (mN/min)	10	10
Sinus Frequency (Hz)	1.0	1.0
Sinus Amplitude (mN)	1.0	1.0

Advanced Protocol

For the advanced (standard) protocol, a trapezoidal loading waveform was applied with a loading/unloading rate of 20mN/min, plus a 30s hold at the maximum load 10mN (Figure 3-21).
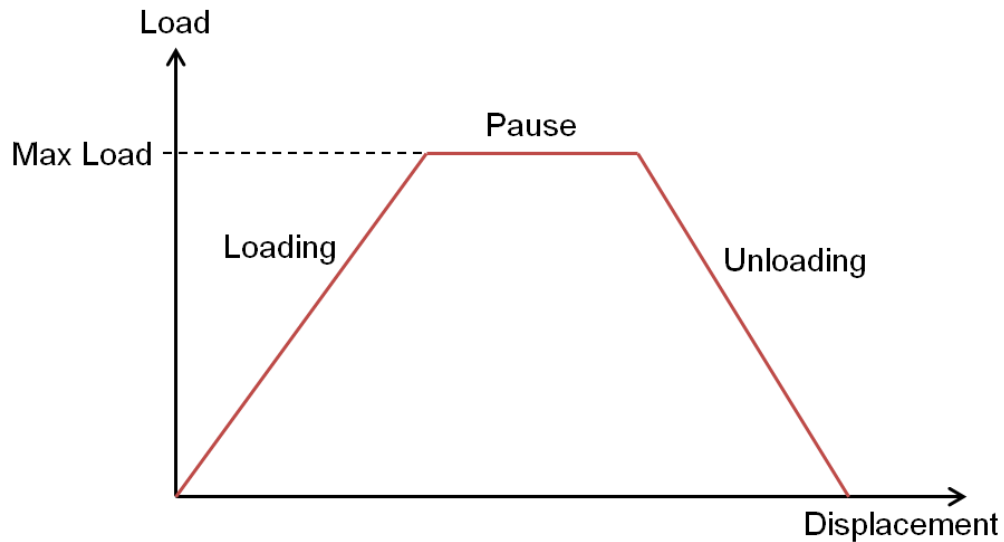
Figure 3-21 The description profile for the advanced indentation parameters.
These parameters need to be specified as the measurement automatically computes a linear loading and unloading to reach the maximum load at a preset time.

Cortical Bone

For the advanced protocol, 3 phases were employed. The hold phase was at 10 mN load and was used to produce creep parameters. The parameters are presented in Table 3-5. The load-penetration curve is shown in Figure 3-22. Two parameters were determined (Oliver and Pharr, 1992): hardness (H_{IT}) and indentation modulus (E_{IT}).
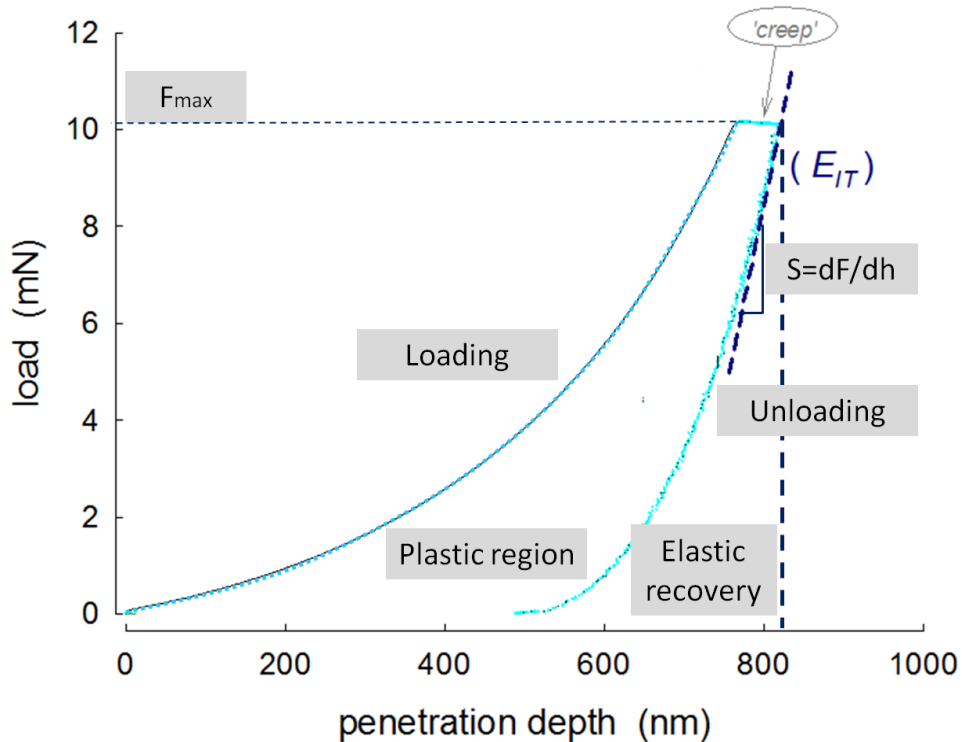
Figure 3-22 The standard indentation profile with associated parameters.
The loading-unloading cycle completed after approximately 3 minutes.

The stiffness from the unloading phase was defined using a power law curve fitted by the Oliver & Pharr method. The upper and lower bounds are defined as 98% and 40% of F_{max}. For indentation on the cortical bone, the locations of the indents were precisely defined under the visualization window and consistently positioned on the medial sector of the cortical bone cross-section. The indents were placed between the periosteal and endosteal of the bone at a space distance between the indent points. The average values of 8-10 indentations in cortical bone samples were taken in advanced and sinus loading protocols. The indentation sites were always checked after the indentation and the failed impressions were removed. For example poorly supported heads of sphere or cross-sections.

Trabecular bone

A similar protocol to that of cortical bone was applied for trabecular bone. However, careful attention was needed as the trabecular bone tissue was distributed and smaller

in size compared to cortical bone. All indents were conducted at the center of the bones based on the optical microscopy observation to include bone tissue as much as possible. The outer edge of the bone was set as a reference. Care should be taken to make sure the indentation sites far away from the edge to eliminate the effect of embedding. The average values of 3 to 5 indentations in trabecular bone samples were taken in advanced and sinus loading protocols.

Sinus Protocol

In the sinus protocol, a sinusoidal waveform was used with a frequency of 1.0Hz and a amplitude of 1.0mN. This protocol is a single indentation measurement with an added sine wave during the loading at a constant loading rate. This allows a depth-related analysis to be carried out in one cycle indentation. In addition to advanced parameters, minimum starting load with the constant strain rate, sinus amplitude and frequency and pause at maximum load if needed (0 second means no pause) were set prior to indentation.

The viscoelastic behaviour of the bones was analysed using the sinus protocol (Table 3-6) (Finnilä et al., 2010). Storage modulus (E') and loss modulus (E'') vary with the depth of the indentation and become stable after a penetration depth above 100 nm, and the values were calculated from the loading curve using Dynamic Mechanical Analysis (CSM V3.75).

Dynamic Mechanical Analysis (DMA) is used to calculate the dynamic stiffness (S) and damping ($D_i\omega$) that are used later in the calculation of E' (Equation 3-14) and E'' (Equation 3-15). S and $D_i\omega$ can be defined as in Equation 3-12 and Equation 3-13 with reference to Figure 3-23.

$$S = \frac{f_0}{h_0}\cos\phi \qquad\qquad 3\text{-}12$$

$$D_i\omega = \frac{f_0}{h_0}\sin\phi \qquad\qquad 3\text{-}13$$

where f_0 is the steady state modulated load amplitude; h_0 is the modulated displacement amplitude; ø is the angular phase shift between the applied force and measured displacement; ω is the frequency of the applied force; D_i is the damping coefficient. The loss (E'') and storage (E') modulus are calculated with,

$$E' = \frac{\pi}{2} \frac{S}{\sqrt{A_p}}$$ 3-14

$$E'' = \frac{\pi}{2} \frac{D_i \omega}{\sqrt{A_p}}$$ 3-15

E' is the material capacity to store energy in which the component in phase with applied load or displacement whilst E'' is the material's capacity to dissipate energy in which the component 90^0 out of phase with applied load or displacement.
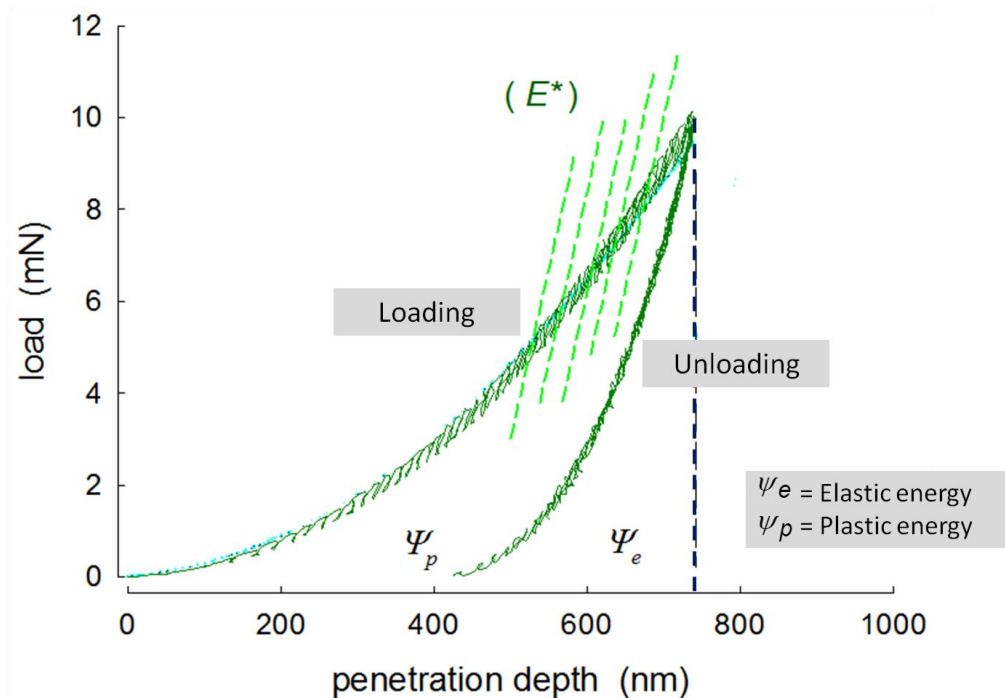
Figure 3-23 The load-penetration depth curve from a sinus indentation protocol. The loading curve consists of sinusoidal cycles in which the stiffness (E*) is calculated from each cycle, as indicated by the lines drawn. The elastic and plastic energy can be obtained also (Adapted from Finnila et al. (2010) and Zioupos & Roger (2006)).

Table 3-7 A summary of the parameters measured.

Advanced Protocol	Formula	Sinus Protocol	Formula
Indentation Hardness (H_{IT})	$\dfrac{F_{max}}{A_p(h_c)}$	Phase Difference ($\tan \partial$)	$\dfrac{E_{loss}}{E_{stor}}$
Reduced (effective) indentation modulus (E_r)	$\dfrac{\sqrt{\pi}}{2\beta}\dfrac{S}{\sqrt{A_p}}$	Storage Modulus (E_{stor})	$\dfrac{\pi}{2}\dfrac{S}{\sqrt{A_p}}$
Elastic Modulus	$\dfrac{\left(1-v_s^2\right)}{\dfrac{1}{E_r}-\dfrac{(1-v_i^2)}{E_i}}$	Loss Modulus (E_{loss})	$\dfrac{\pi}{2}\dfrac{D_i\omega}{\sqrt{A_p}}$
Creep (C_{IT})	$\dfrac{h_2-h_1}{h_1}\cdot 100$	Elasticity (η_{IT})	$\dfrac{W_{elast}}{W_{total}}\cdot 100$

3.8 Bone mineral density (BMD)

Bone mineral density (BMD) was standardised to the volumetric density of calcium hydroxyapatite (CaHA) in terms of $g\cdot cm^{-3}$. The technique used for characterising bone mineral provides information about the composition of the bone. BMD has been shown to have an impact on the bone mechanical strength measurements. It is hypothesised that the reduction in bone strength in *mdx* mice is due to alterations in bone structure and BMD levels. There are several techniques to determine the amount of mineral in the bone and relate this to the fracture behaviour.

3.8.1 Ash content

In the present study, the classic bone mineral composition techniques: ash content and Thermogravimetry Analysis (TGA) (Section 3.8.2), were considered. Ash content has been the standard method to determine the bone density of small animals (Keenan et al., 1997). An understanding of the composition of bone is essential for the proper interpretation of the process of its formation in the living organism. Ash percentage in

the tibia is a good indication of bone densitometry. With reference to the ash content method reported by Silva et al. (2002), the cortical fracture bone fragments post three-point bending test were used to calculate the ash content. The measurement was divided into two parts: 1) wet weight measurements and 2) dry weight measurements. These measurements were calculated based on Archimedes' principle (Equation 3-16 and Equation 3-17). For wet weight measurement, two bones from each genotype were placed in a fresh tube that has been filled with small amount of cotton. This allowed the marrow to be collected after centrifuge.

The bones were centrifuged at 13,200 rpm for 15 minutes using microcentrifuge 5415D (Appendorf, USA). The microcentrifuge works at 120 V and 60 Hz at a maximum rotational speed of 13,200 rpm and the acceleration time to maximum speed is 13s. The bone marrow tissue will be removed in centrifuged bones. The bones were then weighed using an analytical balance (Sartorius LA230 S Analytical Balance) and placed in porcelain crucibles (heat resistant to 1000ºC). Bone dry weight was determined by drying the bone at 90ºC for 24 hours. An environmental chamber Micro LTCL 350 (TAS Ltd, UK) was used. After 24 hours, the crucible was taken out before measuring the weight.

Ash weight was determined by heating the bone at 600ºC for 24 hours in a muffle furnace. To increase the reliability of the measurement, each bone was measured five times. The bone mineral content was determined by ash fraction, to obtain final ash content (Keene et al., 2004). The ash content can be expressed on either a dry or wet basis:

$$\text{Ash \% (dry basis)} = \frac{M_{ash}}{M_{dry}} \times 100 \qquad\qquad 3\text{-}16$$

$$\text{Ash \% (wet basis)} = \frac{M_{ash}}{M_{wet}} \times 100 \qquad\qquad 3\text{-}17$$

where M_{ash} refers to the mass (weight) of the ashed sample and M_{dry} and M_{wet} refer to the original masses (weights) of the dried and wet bone samples.

There are some limitations in the method. Firstly, the samples used in this technique were small in size and fragile to handle. Any errors during handling could contribute to inaccurate data. The error increases especially after the bone is heated at a high temperature. After heating the bone in the crucible, the crucible, bone, and lid should be allowed to cool to room temperature, preferably in a desiccator before weighing them on the analytical balance. This is to prevent the air current produced by the high temperature and environmental factors such as dust and humidity that can lead to inaccurate results. To overcome the limitations of this technique, TGA has been used to determine BMD of the tibia bone.

3.8.2 Thermogravimetric Analysis (TGA)

TGA measures the change in mass as a function of temperature. It consists of a sample pan that is supported by a precision balance. The properties and behaviour that can be measured by TGA include composition, purity, decomposition reactions, decomposition temperature and moisture content (loss of water). In this study, TGA was used for the purpose of determining weight percentage ash. The mass of the bone was measured as it was heated, cooled and held at constant temperature.

The TGA test was performed using a Perkin Elmer TG-7 equipped with a P.E 3700 Data Station. The analysis was done using NETZSCH Proteus-Thermal Analysis version 6.1.0. Heating rate was set at a rate of 5°/min up to 1000°C in an air flow of 20 cm^3/min. The bone was firstly ground with pestle and mortar agate before being weighed for the test. 100 mg ground bones were placed in the alumina crucible. The crucibles were pre-weighed accurately using analytical balance and accuracy was taken to be ± 0.0001g. The weight of the crucible and mass of the bones were recorded in a log book.

3.9 Statistical Analyses

The mean and the standard deviation were reported for all the morphometric, mechanical and tissue parameters. Comparisons were made between *mdx* and each of the other three genotypes, Wild-type (WT), P2X7$^{-/-}$ and *mdx*/P2X7$^{-/-}$. The non-parametric Kruskal-Wallis test was used to test the difference between each pair (i.e. WT vs *mdx*; P2X7$^{-/-}$ vs *mdx* and *mdx*/P2X7$^{-/-}$ vs *mdx*) and significant differences were indicated when p-value<0.05. All test assumptions were verified and analyses were carried out using SPSS (PASW version 18.0). SPSS (Statistical Package for the Social Science) is one of the most popular statistical packages which can perform highly complex data manipulation and analysis with simple instructions.

Chapter 4

Investigation of bone morphometric properties and microarchitecture due to P2RX7 receptor ablation and murine model of Duchenne muscular dystrophy using microCT.

4.1 Introduction

The objective of the study was to explore the structural alterations due to P2RX7 receptor ablation in mouse bones. The morphometric properties of cortical and trabecular bones of the four genotypes: WT, *mdx*, P2X7$^{-/-}$ and *mdx*/P2X7$^{-/-}$, were examined and compared, and the results are reported here. µCT and image processing analysis revealed considerable differences in cortical bone parameters while several trends were noteworthy in the trabecular bone.

4.2 Results

All data are given as mean ± standard deviation (SD) for each group of samples (n=6 per genotype). Significance was assessed by non-parametric Kruskal–Wallis tests for gross tibial and morphometric measurements. A statistically significant difference is indicated by $p < 0.05$. A comparison of *mdx*/P2X7$^{-/-}$ is made between WT= a, *mdx*= b and P2X7$^{-/-}$= c. The comparison of genotypes will be discussed based on WT (control); *mdx*, P2X7$^{-/-}$ (P2RX7 single knockout) and *mdx*/P2X7$^{-/-}$ (P2RX7 and *mdx* double knockout).

Gross geometric measurements were obtained to determine any changes in skeletal geometry (Figure 4-1). The measurements, summarised in Table 4-1, reveal significant differences in the average bone length and diameter of some of the genotypes. Measured lengths of the tibias showed no significant difference in *mdx* and P2X7$^{-/-}$

compared to those of WT mice. P2X7$^{-/-}$ showed a significant knockout effect, with significantly greater length compared to *mdx* mice (p = 0.036). However, *mdx*/P2X7$^{-/-}$ mice were observed to have shorter length compared to those of WT (p = 0.004), *mdx* (p = 0.010) and P2X7$^{-/-}$ (p = 0.004).

A significantly lower average value of midtibia diameter was found in *mdx* mice than that in WT mice (p = 0.048). A similar trend of reduction in midtibia diameter was observed in P2X7$^{-/-}$ (p= 0.025) and *mdx*/P2X7$^{-/-}$ (p= 0.025) mice, which showed *mdx*/P2X7$^{-/-}$ mice to have the lowest average midtibia diameter of the comparison groups. Metaphyseal diameter of WT mice seems higher in average value compared to those of *mdx*, although it was not statistically significant. A significant higher metaphyseal diameter was observed in P2X7$^{-/-}$ (p= 0.048) mice compared with mdx. However, *mdx*/P2X7$^{-/-}$ mice was observed to have significantly lower metaphyseal diameter compared to those of WT (p= 0.032) and P2X7$^{-/-}$ (p= 0.004) mice.

No differences in distal tibia diameters were observed between the genotypes except for in the *mdx*/P2X7$^{-/-}$ mice, which were observed to have lowest distal diameter. Although it was not statistically significant, WT and P2X7$^{-/-}$ mice have shown higher average distal diameters when compared with the *mdx*.
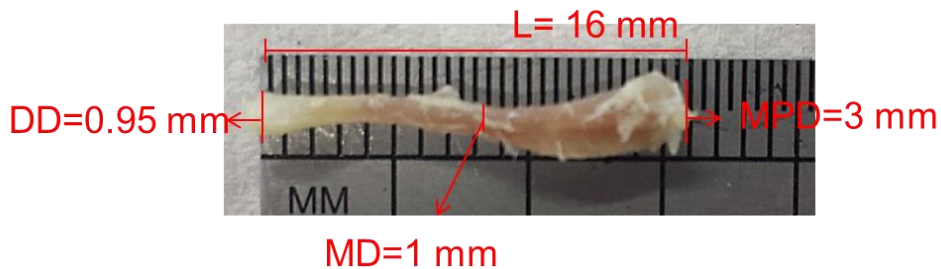
Figure 4- 1 Morphometric length measurements of tibia.
Tibial gross length (L) measurement was taken from proximal anatomical point of centre of the condyles to the distal anatomical point of medial malleolus. Midtibia diameter (MD) measurement was taken at the midtibia, metaphyseal diameter diameter (MPD) measurement was taken from proximal anatomical point of centre of the condyles and

distal diameter (DD) measurement was taken from the distal anatomical point of medial malleolus.

Table 4-1 Summary of the bone geometries of the tibias for all genotypes.

Bone properties (mm)	WT	*mdx*	P2X7^{-/-}	*mdx*/P2X7^{-/-}
Length	14.65±0.62	14.10±0.64	**15.02 ±0.46[b]**	**13.05±0.38[a,b,c]**
Midtibia diameter	1.10±0.06	**0.97±0.12[a]**	**1.00±0.06 [a]**	**0.82±0.04[a,b,c]**
Metaphyseal diameter	2.70±0.21	2.65±0.22	**2.88±0.13[b]**	**2.47±0.15[a,c]**
Distal diameter	0.93±0.08	0.90±0.11	0.95±0.08	**0.73±0.05[a,b,c]**

[a,b,c] and **bold text** indicate $p<0.05$ (Kruskal-Wallis)
[a]statistically significant difference (<0.05) with WT.
[b]statistically significant difference (<0.05) with *mdx*.
[c]statistically significant difference (<0.05) with P2RX7^{-/-}.

Comparisons of the morphometric properties between the four genotypes in both cortical bone at midtibia and trabecular bone at proximal tibial metaphyseal bones are presented in Table 4-2. The results for the morphometric properties of the long bones demonstrate that many properties of long *mdx* dystrophic bones were substantially affected at four weeks in an early stage of life. At this point, the functional muscle impairment is not yet thought to be significant.

4.2.1 Comparison of cortical bone morphometric properties in *mdx* and WT mice.

One of the major findings in the current study is the reduction found in cortical bone parameters in the *mdx* mice. Lower values of cortical bone parameters in *mdx* mice were observed in the total cross-sectional area inside the periosteal envelope (Tt.Ar, 10%), cortical bone area (Ct.Ar, 19%), cortical area fraction (Ct.Ar/Tt.Ar, 11%) and cortical thickness (Ct.Th, 18%), compared to those of WT mice (Table 4-2). Specifically, significantly lower values of cortical bone parameters in *mdx* mice were found in Ct.Ar (p= 0.006) and Cr.Th (p= 0.020). These results are consistent with data reported by Nakagaki et al. (2011). These results are consistent with the findings regarding reduced

biomechanical strength in *mdx* bones (Chapter 5); and also consistent with the reduced bone strength in DMD patients.

Table 4-2 Morphometric properties of the cortical bones of the genotypes studied.

Properties	WT	*mdx*	P2RX7$^{-/-}$	*mdx*/P2RX7$^{-/-}$
(Midtibia)				
Tt.Ar (mm^2)	1.344±0.263	1.216±0.114	1.089±0.139	**0.722±0.123^{a,b,c}**
Ct.Ar (mm^2)	0.160±0.017	**0.130±0.018^a**	**0.161±0.030^b**	**0.172±0.01^b**
Ct.Ar/Tt.Ar (%)	0.405±0.038	0.360±0.015	**0.419±0.026^b**	**0.411±0.031^b**
Cr.Th (mm)	0.150±0.017	**0.123±0.010^a**	0.137±0.014	**0.115±0.009^{a,c}**

[a,b,c] and **bold text** indicate p<0.05 (Kruskal–Wallis)
[a]statistically significant difference (<0.05) with WT.
[b]statistically significant difference (<0.05) with *mdx*.
[c]statistically significant difference (<0.05) with P2RX7$^{-/-}$.

4.2.2 Alterations in cortical bone morphometric properties of *mdx*/P2X7$^{-/-}$ mice.

Another important structural finding of the study is the alterations found with respect to the cortical bone parameters for the *mdx*/P2X7$^{-/-}$ mice.

Statistically significant differences were found between Tt.Ar, Ct.Ar and Ct.Ar/Tt.Ar of *mdx*/P2X7$^{-/-}$ and those of the other three genotypes. The *mdx*/P2X7$^{-/-}$ mice had a significantly lower total cross-sectional area inside the periosteal envelope (Tt.Ar) compared to those of the other three genotypes (WT (p=0.004); P2X7$^{-/-}$ (p=0.004) and *mdx* (p=0.004)). The *mdx*/P2X7$^{-/-}$ mice had a 41% lower Tt.Ar than that of the *mdx* mice. By contrast, however, the *mdx*/P2X7$^{-/-}$ mice had a substantially higher Ct.Ar (by 32%, p=0.004) and cortical bone area fraction (by 14%, p=0.010) compared with those of *mdx*, although a slightly lower (by 7%) cortical thickness was noted.

The morphometric properties of WT and P2X7$^{-/-}$ bones at four weeks were not significantly different in any of the parameters measured. The cortical bone property values for the P2X7$^{-/-}$ mice remained significantly higher (Ct.Ar, p = 0.036; Ct.Ar/Tt.Ar, p = 0.005) than those of the *mdx* mice, except the total cross-sectional area. The mean

values for the P2X7$^{-/-}$ mice cortical bone parameters are between those of WT and *mdx* mice.

Figure 4-2 shows bar graphs depicting the quantitative analysis of cortical bone parameters. Note that the majority of the data seem to indicate a clear trend of increased cortical area and cortical bone area fraction in *mdx*/P2X7$^{-/-}$ mice over *mdx* mice (p<0.05), but reduced total cross-sectional area and cortical thickness in the midtibia region.
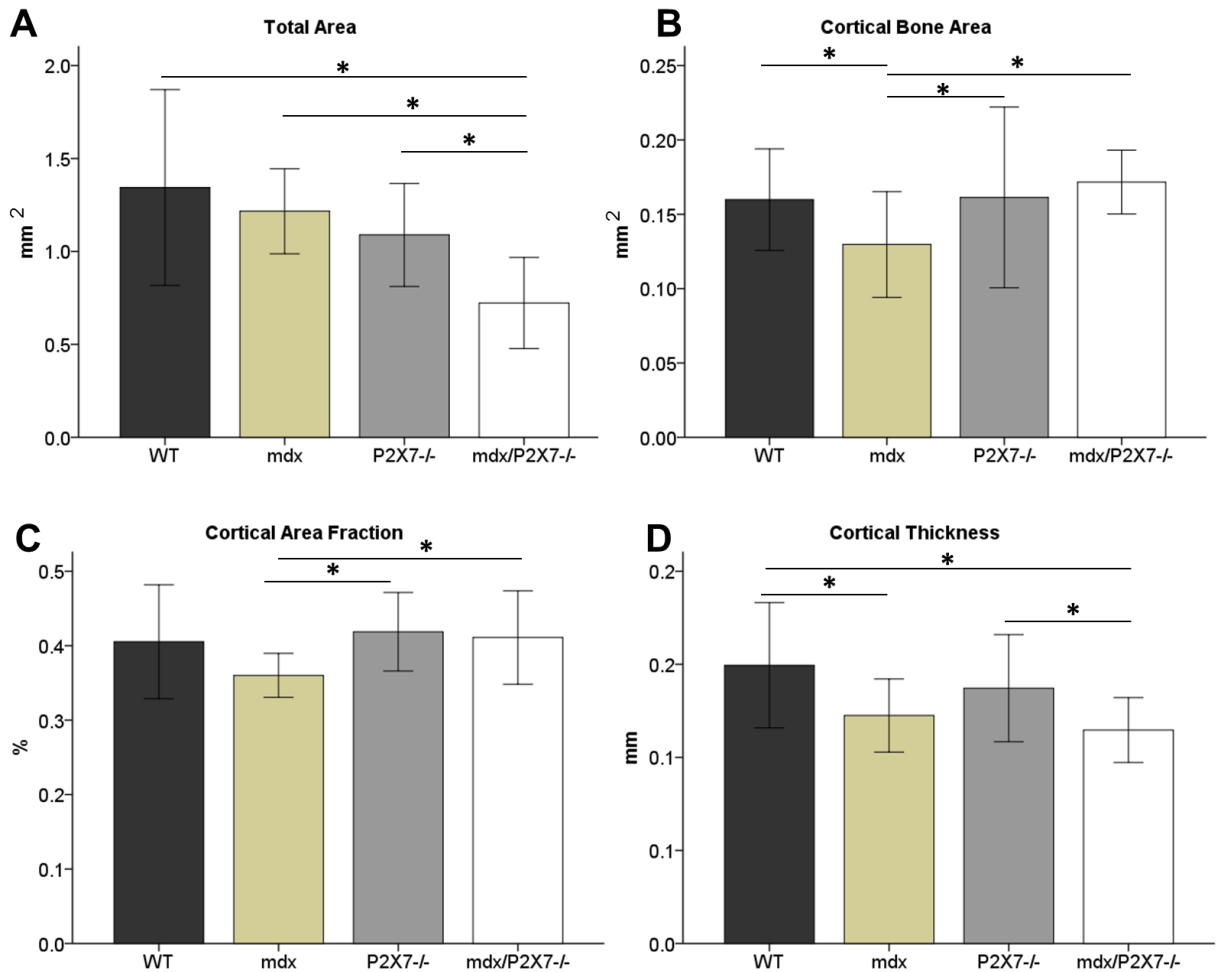
Figure 4-2 Comparison of relative changes in morphological parameters of the cortical bone at midtibia level of the genotypes.
(A) Total area (Tt.Ar); (B) cortical bone area (Ct.Ar); (C) cortical area fraction (Cr.Ar/Tt.Ar); and (D) cortical thickness (Ct.Th). Bars correspond to mean ± SD. Abbreviation: *p<0.05.

4.2.3 Trabecular bone volume fraction and trabecular bone thickness of *mdx* vs. WT mice

Comparisons between the four genotypes revealed that reduced values of trabecular bone volume fraction (BV/TV) and trabecular thickness (Tb.Th) were found in *mdx* proximal tibia metaphyseal bones compared with those of WT. Specifically, the mean

bone volume fraction in the proximal tibia metaphyseal region in *mdx* mice was 35% lower (p=0.030), whilst the trabecular thickness was 19% lower (p=0.006), compared to those of WT mice. No significant difference was observed in trabecular spacing and connectivity density between the results of WT and *mdx* mice, although the *mdx* had lower values in trabecular spacing and higher values in connectivity density. Both BV/TV and Tb.Th in *mdx* mice were the lowest amongst all the genotypes studied. These results are consistent with the data reported by Nakagaki et al. (2011).

Figure 4-3 shows the distributions of data for the trabecular bones, including the medians, the 25th and 75th percentiles, and the outliers. With respect to trabecular bones (Fig 4-2A), the BV/TV in the *mdx* mice were lowest. There were improvements in BV/TV and trabecular thickness (Fig 4-2B) in the WT over those of the *mdx*; however, again, no significant changes were noted in either trabecular spacing or connectivity.

4.2.4 Trabecular bone volume fraction in *mdx*/P2X7^{-/-} mice.

A significant increase of BV/TV in *mdx*/P2X7$^{-/-}$ mice was found compared with that of the *mdx* (p = 0.016), although the other parameters, including trabecular thickness (+2%), spacing (-8%) and connectivity density (-22%) were not statistically different compared to those of the *mdx* mice. There may have been some influence from P2RX7 ablation on these properties, although this was not statistically significant. Connectivity density in the *mdx*/P2X7$^{-/-}$ mice was lower than that of the *mdx* and closer to that of the WT mice. Significant improvements in trabecular bone volume fraction and lower quantitative values for trabecular bone spacing suggested a significant treatment effect in the *mdx*/P2X7$^{-/-}$ mice.

In the P2X7$^{-/-}$ mice, the results showed a significant increase (+53%, p=0.004) in trabecular bone volume fraction and a significant reduction (-21%, p=0.043) in trabecular spacing compared to the *mdx* mice, suggesting a significant knockout effect. (Findings are summarised in Figure 4-3 and Figure 4-4.)

Table 4-3 Morphometric properties of trabecular bones of the genotypes studied.

Properties	WT	*mdx*	P2RX7$^{-/-}$	*mdx*/P2RX7$^{-/-}$
(Proximal tibial metaphyseal)				
BV/TV (%)	0.193±0.066	**0.125±0.027^{a}**	**0.265±0.125^{b}**	**0.180±0.036^{b}**
Trab.Th (mm)	0.052±0.004	**0.042±0.004^{a}**	0.053±0.015	**0.043±0.005^{a}**
Trab.Sp (mm)	0.258±0.055	0.242±0.040	**0.190±0.028^{a,b}**	0.223±0.059
Conn.D (1/mm^{3})	113.92±73.05	162.41±90.16	140.79±76.86	125.98±93.19

[a,b,c] and **bold text** indicate p<0.05 (Kruskal–Wallis)
[a]statistically significant difference (<0.05) with WT.
[b]statistically significant difference (<0.05) with *mdx*.
[c]statistically significant difference (<0.05) with P2RX7$^{-/-}$.

Figure 4-3 shows the distributions of data for the trabecular bones. It seems that the data regarding bone volume fraction from the knockout bones are more scattered, although the majority of the data seem to indicate a clear trend of higher bone volume fraction in the *mdx*/P2X7$^{-/-}$ mice over that of the *mdx* mice in the midtibia region.
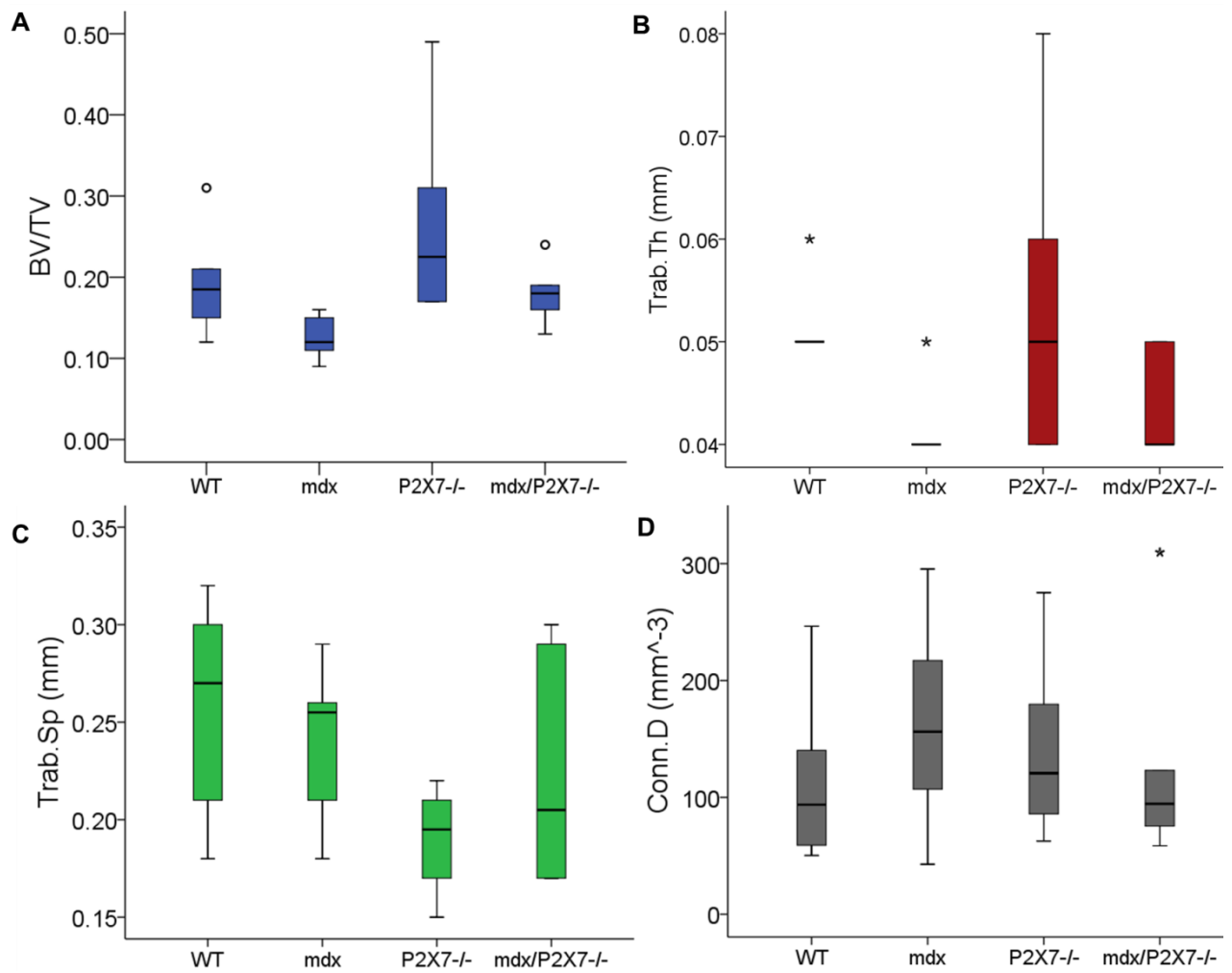
Figure 4-3 Comparison of the morphometric properties of the WT, *mdx*, P2X7^{-/-}, and *mdx*/P2X7^{-/-} of the trabecular bones at proximal tibial metaphyseal.
(A) BV/TV, (B) trabecular thickness (Trab.Th), (C) trabecular space (Trab.Sp), and (D) connectivity density (Conn.D). Bars correspond to the median (50th percentile) at 25th and 75th percentiles with some outliers (°) and far outliers (*).

Figure 4-4 shows the representative 3D μCT scans of trabecular bones for all the genotypes studied. The metaphyseal regions in the *mdx* mice revealed a more porous trabecular bone structure compared to those of the WT, P2X7^{-/-} and *mdx*/P2X7^{-/-} mice. In contrast, a more robust trabecular structure, with an increased network of rods and plates, was found in knockout bones and WT. The porosity was less evident in these bones compared to those of *mdx* mice.
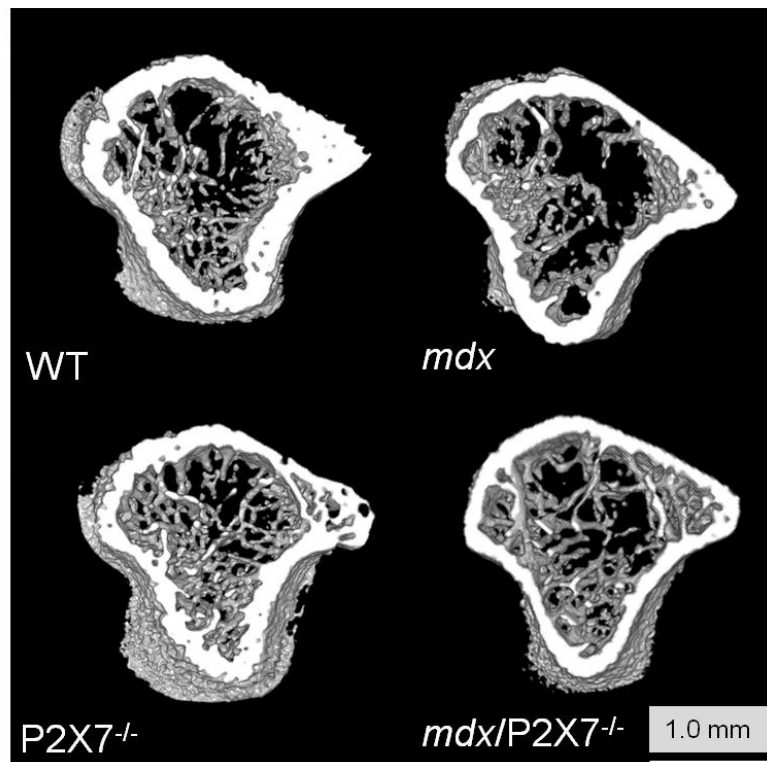
Figure 4-4 3D μCT images.
The figure shows representative trabecular samples from WT, *mdx*, P2X7^{-/-} and *mdx*/P2X7^{-/-}.

4.3 Discussion

The morphometric studies show that genetic ablation of the P2RX7 receptor knockout in *mdx* mice bone results in significant changes in the bone both at the macro and microstructural level. The results seem to suggest that most microstructural properties in *mdx* dystrophic bone are already significantly affected at four weeks, which is an early stage when, despite histological changes, the functional muscle impairment in this DMD mouse model is not yet thought to be significant (Nakagaki et al. 2011). The alternations in cortical and trabecular bone parameters in the structure found could account for the biomechanical results reported in the subsequent results.

In *mdx* mice, muscle degeneration associated with inflammatory cell infiltrations is thought to start at about three weeks, and at four weeks it closely resembles the human pathology (Grounds et al., 2008). Spinal cord injury or sciatic neurectomy leading to rapid, profound and permanent loss of muscle mass produces significant bone loss within 10–14 days (Gross et al., 2010). The degeneration in *mdx* muscles at four weeks does not cause a comparable functional impairment. It seems unlikely that muscle strength and associated mechanical loads are as significantly affected one week into the pathology, and so the bone abnormality is considered less likely to be caused by the decreased osteogenic stimulation. Moreover, Anderson et al. (1993) showed that, in contrast to other disuse osteopenia studies, bone parameters remained significantly affected despite muscle mass and strength recovery in 18-week-old *mdx*.

The cortical bone parameter analysis of *mdx*/P2RX7$^{-/-}$ mice revealed a 32% increase in cortical bone area, 14% increase in cortical bone fraction, 41% reduction in total cross-sectional area and 7% reduction in cortical bone thickness over those *mdx* (Figure 4-2). The results revealed that the *mdx*/P2RX7$^{-/-}$ mice had smaller bones than the other three types. However, the cortical bone fraction was relatively higher in the *mdx*/P2RX7$^{-/-}$ mice bones. Hence, this might have been responsible for the similar strength achieved in this to the other three types. The preliminary studies involving thermogravimetric analysis were carried out on two samples per genotype. The inorganic phase content of the samples was determined from the results of the analysis. The TGA test provides information on the loss in mass as temperature

changes. The information includes water content, organic matrix content and residual mass (hydroxyapetite-HA) (Figure 4- 5).
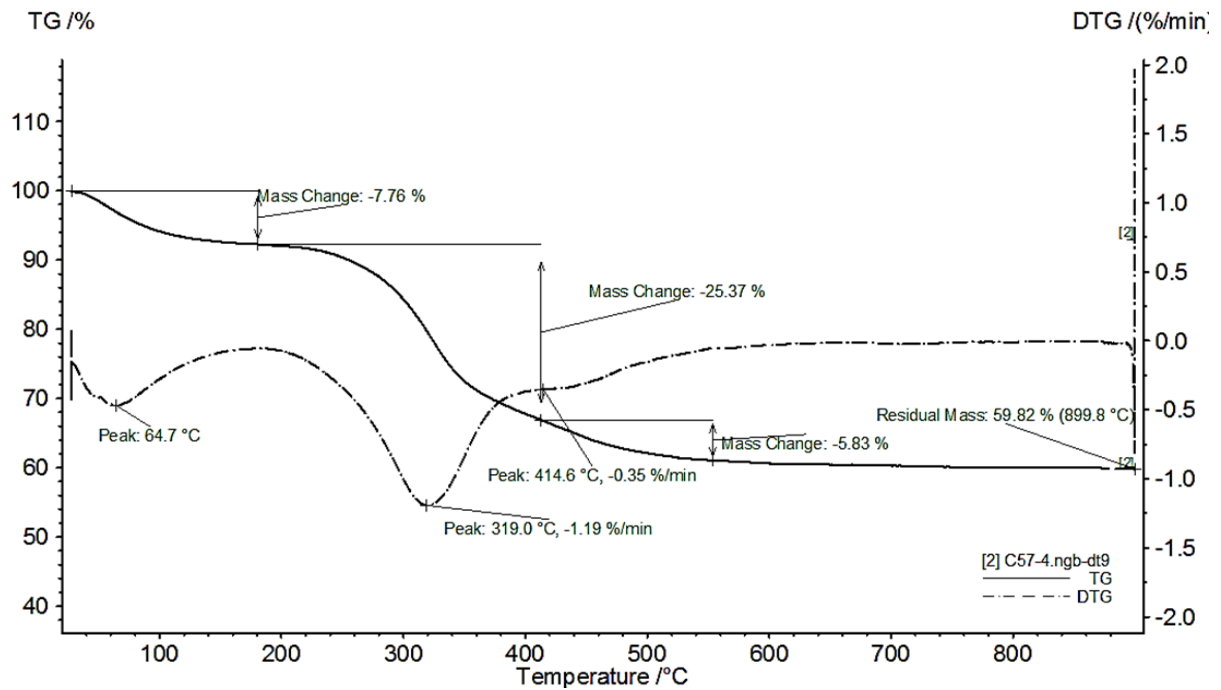
Figure 4- 5 A TG-DTG curve shows plot from a mouse bone.

The TG-DTG plots recorded from bone samples display three thermal processes which are identified as follows: loss of water up to 200°C, organic content from 200 to 600°C and carbonate content above 600°C (Florez et al., 2014).

The preliminary studies revealed that there was significantly higher organic content than those of *mdx* mice (Table 4-4). The changes suggest that the higher organic content in *mdx*/P2RX7$^{-/-}$ mice might contribute to the bone ductility. It was also presented in the mechanical test results (Chapter 5).

Table 4-4 The bone mineral composition obtained from TG-DTG curves of the studied bone samples.

Bone properties	WT	*mdx*	P2X7$^{-/-}$	*mdx*/P2X7$^{-/-}$
Water (%)	7.97±0.29	7.69±0.199	8.19±0.29	7.53±0.21
Organic (%)	**24.99±0.54**[b]	21.06±0.24	23.51±0.85	**25.79±1.52**[b]
Mineral (%)	8.31±3.50	9.53±0.43	11.45±0.07	10.82±1.17
Carbonate (%)	57.51±3.27	60.19±0.23	55.56±0.60	54.96±2.86

[a,b,c] and **bold text** indicate p<0.05 (ANOVA)
[a] statistically significant difference (<0.05) with WT.
[b] statistically significant difference (<0.05) with *mdx*.
[c] statistically significant difference (<0.05) with P2RX7$^{-/-}$.

The findings regarding the cortical and trabecular bone parameters seem consistent with those reported in *mdx* mice bone by Nakagaki and colleagues (2011). They reported a reduced trabecular area fraction of 41% and thickness of 40% in the distal epiphysis of *mdx* femur, along with a significantly lower cortical cross-sectional area of 24%, diaphyseal cortical area of 44%, and cortical bone thickness of 43% in the diaphyseal of the *mdx* femur (Nakagaki et al., 2011). In the current study, trabecular bone of the *mdx* tibia showed a reduction of 35% in the trabecular bone volume fraction and 19% in trabecular thickness. At the cortical bone level, only a 10% reduction in total cross-sectional area was noted in *mdx* compared with WT mice, which was not statistically significant.

The trends of reduction in cortical and trabecular bone parameters are consistent with the subsequent biomechanical test results (Chapter 5), and the micro-structural arrangement may be a possible mechanism for the reduced bone strength seen in *mdx* mice. The findings regarding the cortical bone parameters are also consistent with Rufo's (Rufo et al. 2010) analysis of *mdx* mouse bone, in which they showed a

similar reduction of 11.3% in cortical thickness and 13% in cortical area, but modest reduction in cortical thickness of 6%, as compared to the WT mouse model. For trabecular bone parameters, they showed a reduction of bone volume fraction of 38%, bone thickness of 22%, and trabecular number of 15%. The bone thickness in WT and *mdx* were not found to be different, which is in line with the current findings. Although the trend is similar between the two studies, the quantitative difference between the current study and Rufo's analysis may be due to the high variance found in the statistical analysis of the mouse models, or differences in the age and strain type between the mouse models (Rufo et al., 2011). With respect to the age difference, Rufo's *mdx* mouse was much older (six months) than the current *mdx* mouse (four weeks). Hence, the reduction of the cortical bone parameter in the *mdx* mice may be worsened with age. This is consistent with the fact that bone phenotype (reduction in all cortical and trabecular bone parameters) in DMD patients has been reported to deteriorate with age (McDonald et al., 2002; Bianchi and Morandi, 2008; Morgenroth et al., 2012).

It is not known whether the bone abnormality is due to the lack of dystrophin in specific bone cells. This is because expression of the DMD gene in osteoblasts and osteoclasts has not been studied. Given that bone abnormalities in *mdx* mice have been linked to chronic inflammation (Abou-Khalil et al., 2013), and, in general, inflammation can cause bone loss (Redlich and Smolen, 2012), this is the most likely mechanism behind dystrophic bone abnormalities. Importantly, if this is the case, the current data indicate that sterile inflammation may exert very rapid (within one week) and profound effects on the bone physiology.

The P2RX7 receptor was identified as a powerful activator of the "danger mode" of the native immune response through release of pro-inflammatory cytokines (Di Virgilio, 2007). Based on the observation that ablation of this receptor alleviates muscle symptoms (Sinadinos et al., 2015), it was hypothesised that ablation of the P2RX7 receptor could improve the morphometric and mechanical properties of dystrophic bones. The present results show that its ablation in *mdx* mice produced an overall decrease in the muscle inflammatory signature of dystrophic muscles (Sinadinos et al., 2015), and this reduced inflammatory signature in *mdx*/P2X7$^{-/-}$ muscles may therefore have translated into reduced bone loss in these mice.

The influence of P2RX7 inhibition, which is known to have therapeutic effects on skeletal muscles, seems significant on the morphological properties of bones. Importantly, the significantly higher cortical bone area and fraction, as well as bone volume fraction, in both cortical and trabecular *mdx*/P2X7$^{-/-}$ bones, respectively, would seem to suggest that the overall effect of the ablation is bone formation for the models studied. The longer-term effects of P2RX7 receptor ablation have also been tested, and a significant improvement in bones of six-month-old *mdx*/P2RX7$^{-/-}$ mice found (Sinadinos et al., 2015). As bone abnormalities in *mdx* mice have been linked to chronic inflammation (Abou-Khalil et al., 2013), the reduced inflammatory signature in *mdx*/P2X7$^{-/-}$ muscles may also translate into reduced bone loss in these mice. However, at this stage it is difficult to ascertain whether the mechanism is secondary to the improvements in muscle morphology observed in the later phases of *mdx* pathology.

One of the unique features of the current study is the use of an *mdx*/P2X7$^{-/-}$ mouse model for the structural analysis of bone. This is the first time that this mouse model has been used to explore the micro-structural effect in P2RX7 receptor ablation of *mdx* mice. The *mdx*/P2X7$^{-/-}$ mice did show a significant improvement in cortical and trabecular bone structural parameters. These findings highlight the need to further explore the possible alterations in bone mechanical properties at both macro and micro levels, these results are presented in Chapters 5 and 6.

Chapter 5

Evaluation of bone biomechanical properties across the genotypes using three-point bending test

5.1 Introduction

Bones play unique roles in the body, maintaining its shape, protecting internal organs and withstanding force. However, bones can only sustain loads up to a certain limit, beyond which they fail. Understanding the fracture behaviour of bone is necessary for the prevention and diagnosis of trauma. This can be achieved by studying the mechanical properties of bone (Li et al., 2013). Given that DMD patients have a demonstrated increased risk of fracture and reduced bone strength, the aim of this study is to analyse the biomechanical properties of bones in mdx/P2X7$^{-/-}$ mouse model compared to WT, mdx and P2X7$^{-/-}$ mice. It was aim to explore the potential genotype-related deficiencies in mechanical properties of bones and it was hypothesised that improved bone strength in mdx/P2X7$^{-/-}$ mice may be obtained with improved functional integrity following P2RX7 receptor inhibition.

In DMD patients, fracture often occurs in long bones, which consists mainly of cortical bone. In the current study, the left tibias from each comparison genotype were subjected to a three-point bending test after they were scanned using μCT. Generally, biomechanical test revealed that the mdx/P2X7$^{-/-}$ bones have relatively higher average flexural strength, work-to-fracture and significantly higher strain to failure compared with those of mdx, suggesting greater resistance to fracture.

5.2 Results

5.2.1 Mechanical properties of mdx vs WT mice.

Following the morphometric analysis, mechanical tests were applied in order to explore possible differences in the biomechanical properties of the mice bones under study. Figure 5-1 shows the individual stress-strain curves for the four genotypes,
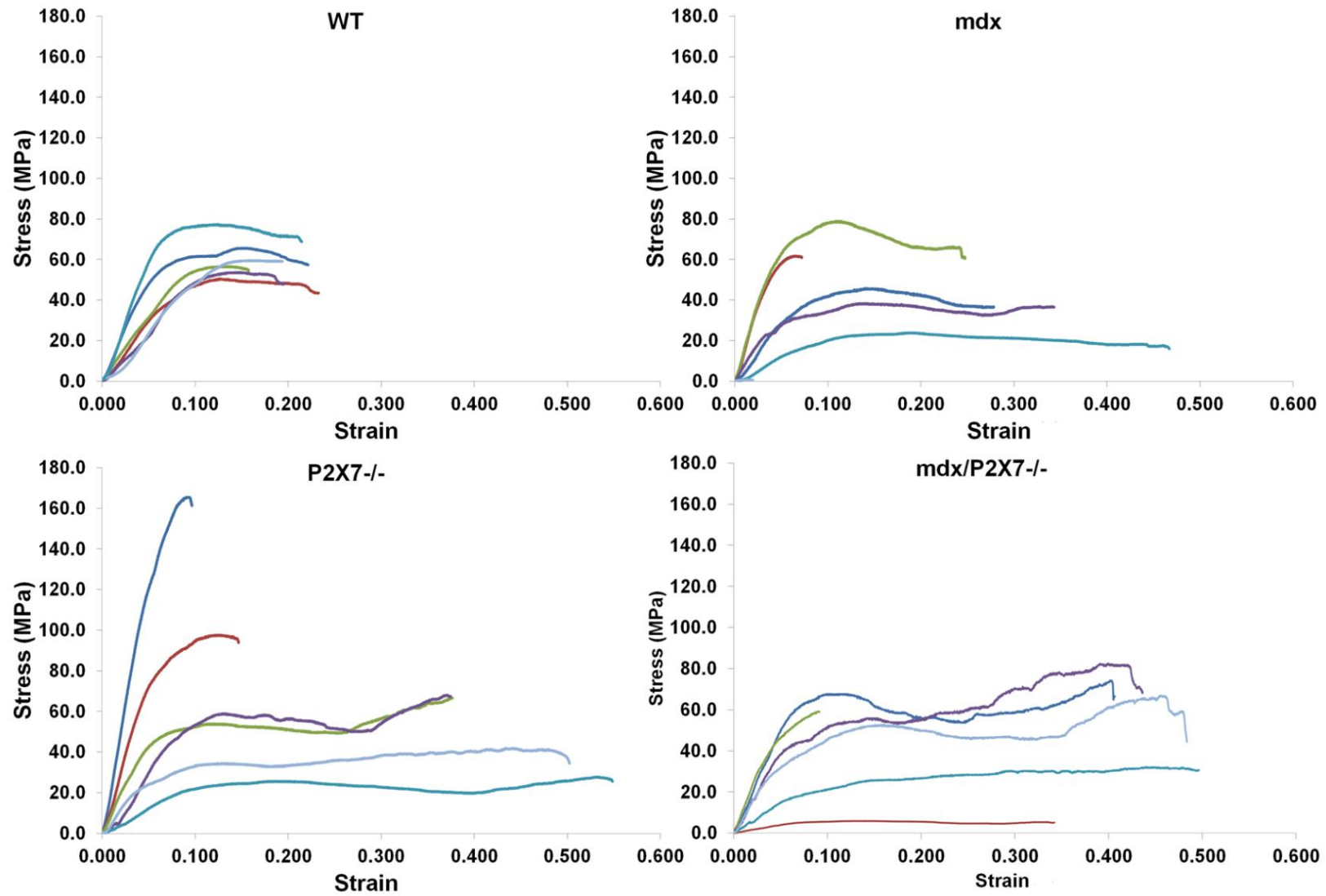
Figure 5-1 Stress-strain curves for the four genotypes.

from which the load is converted into stress and deformation is converted into strain. The stiffness, maximum load, and work-to-fracture were determined from the load-displacement curves, whilst the flexural strength and strain at failure were calculated using Eq. 3-3 and Eq. 3-4, as described in Chapter 3. Post-yield stress-strain curves show a greater strain at failure in *mdx* than in WT mice; however, two *mdx* tibias (n=2) had the lowest strain to failure and fractured at less than 0.1 (Figure 5-1). In contrast, the stress or flexural strength of *mdx* mice was observed to be lower compared to that of WT mice, although this difference was not statistically significant (Table 5-1). Table 5-1 shows the mean and the standard deviation of the mechanical properties for the four genotypes, indicating the statistically significant differences. Abbreviations: $p<0.05$ with symbol: A comparison of *mdx*/P2X7$^{-/-}$ is made between WT= a, *mdx*= b and P2X7$^{-/-}$= c. The comparison of genotypes will be discussed based on WT (control); *mdx*, P2X7$^{-/-}$ (P2RX7 single knockout) and *mdx*/P2X7$^{-/-}$ (P2RX7 and *mdx* double knockout). Tibias from P2X7$^{-/-}$ revealed that the post-yield stress-strain curve measures were close to those of *mdx*/P2X7$^{-/-}$, indicating greater strain at failure for the knockout models.

Table 5-1. The mechanical properties of the genotype bones.

Bone properties	WT	*mdx*	P2X7$^{-/-}$	*mdx*/P2X7$^{-/-}$
Maximum load (N)	4.99±0.89	**3.10±0.90**[a]	4.32±1.63	**2.43±0.45**[a,c]
Stiffness (N/mm)	12.16±2.12	**7.19±2.58**[a]	**8.64±2.73**[a]	**3.38±1.51**[a,b,c]
Work-to-fracture (N·mm)	4.01±1.00	3.31±1.36	5.79±2.02	4.59±2.06
SMA (mm^4)	0.11±0.03	0.09±0.03	0.08±0.03	**0.04±0.01**[a,b,c]
Flexural strength (MPa)	60.49±9.74	49.65±19.09	73.36±48.27	62.97±17.39
Strain at failure	**0.15±0.02**[c]	0.14±0.04	**0.37±0.15**[b]	**0.39±0.12**[a,b]

[a,b,c] and **bold text** indicate $p<0.05$ (Kruskal-wallis)
[a]statistically significant difference (<0.05) with WT.
[b]statistically significant difference (<0.05) with *mdx*.
[c]statistically significant difference (<0.05) with P2RX7$^{-/-}$.

Results revealed that *mdx* mice have a reduced maximum load (38%, p=0.016), stiffness (41%, p=0.037), work-to-fracture (17%, p>0.05), flexural strength (18%, p>0.05) and second moment of area (SMA) (18%, p>0.05) compared to WT mice. Strain at failure was the only aspect that showed a similar value to that of WT mice (WT=0.15±0.02 vs *mdx*=0.14±0.04). Tibias from P2X7$^{-/-}$ (p=0.037) showed significantly increased strain at failure compared to those of *mdx* mice. Moreover, P2X7$^{-/-}$ mice did not differ significantly when compared with *mdx* for work-to-fracture (P2X7$^{-/-}$=5.79±2.02 vs *mdx*=3.31±1.36) and flexural strength (P2X7$^{-/-}$=73.36±48.27 vs *mdx*=49.65±19.09), although P2X7$^{-/-}$ mice clearly showed the values were increased. No significant difference was noted between P2X7$^{-/-}$ and WT mice indicative of a knockout effect, except for stiffness. P2X7$^{-/-}$ mice revealed significantly reduced stiffness (29%, p=0.025) when compared with WT.

Figure 5-2 and Figure 5-3 show the measured mean, the standard deviation and the spread of the mechanical properties, including the medians, the 25th and 75th percentiles and the outliers, in boxplots for the four genotypes. It seems that the mechanical properties of P2X7$^{-/-}$ bones have a greater average distribution than the other comparison groups. This is followed by WT and *mdx*/P2X7$^{-/-}$ bones. Again, knockout mice showed a significant effect and measures were not found to be significantly different from those of WT bones.
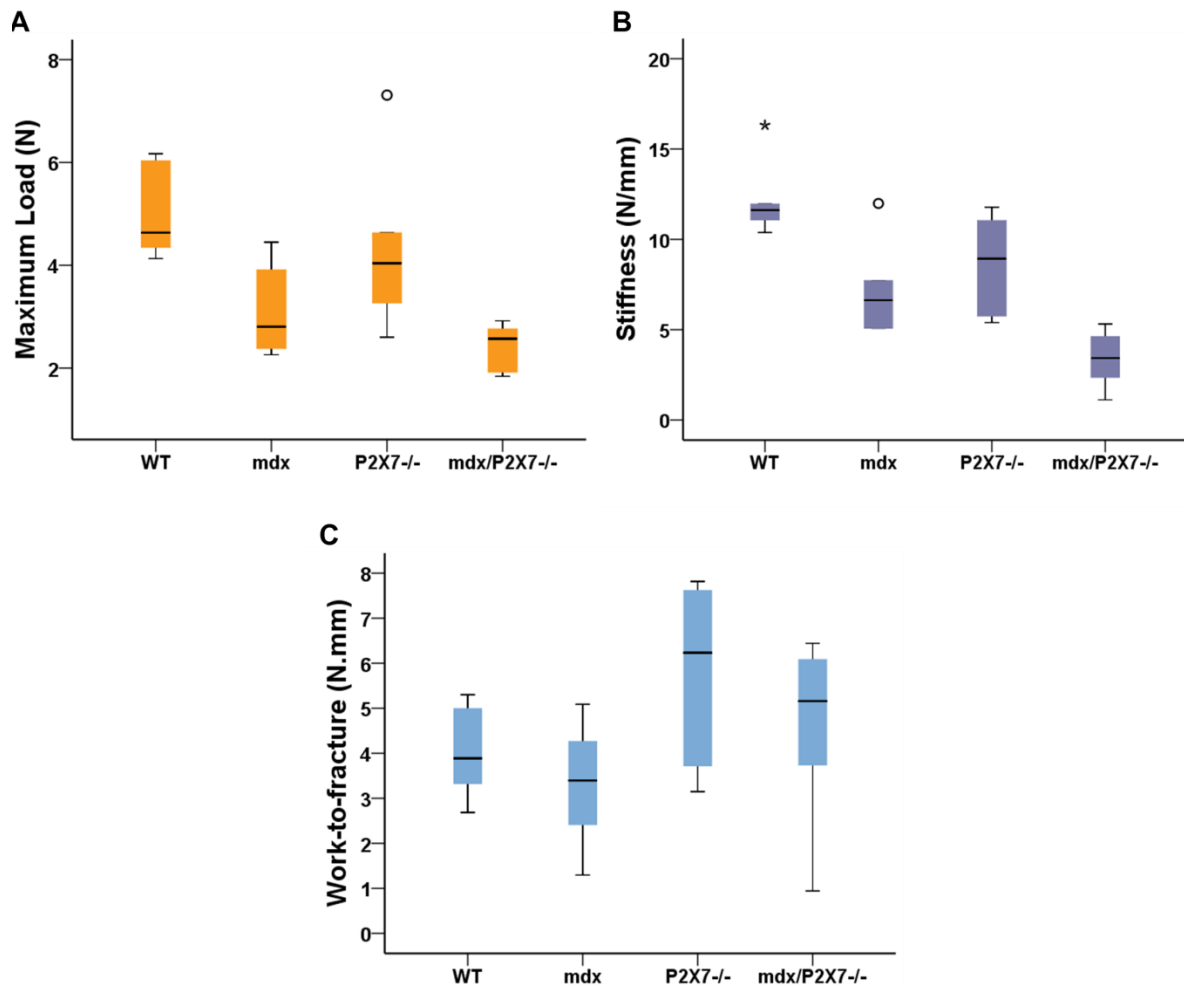
Figure 5-2 A comparison of the mechanical properties of bones obtained from the three-point bending tests.

(A) Maximum load; (B) flexural modulus; and (C) work-to-fracture. The boxplots for the four genotypes include the medians, the 25th and 75th percentiles and the outliers.
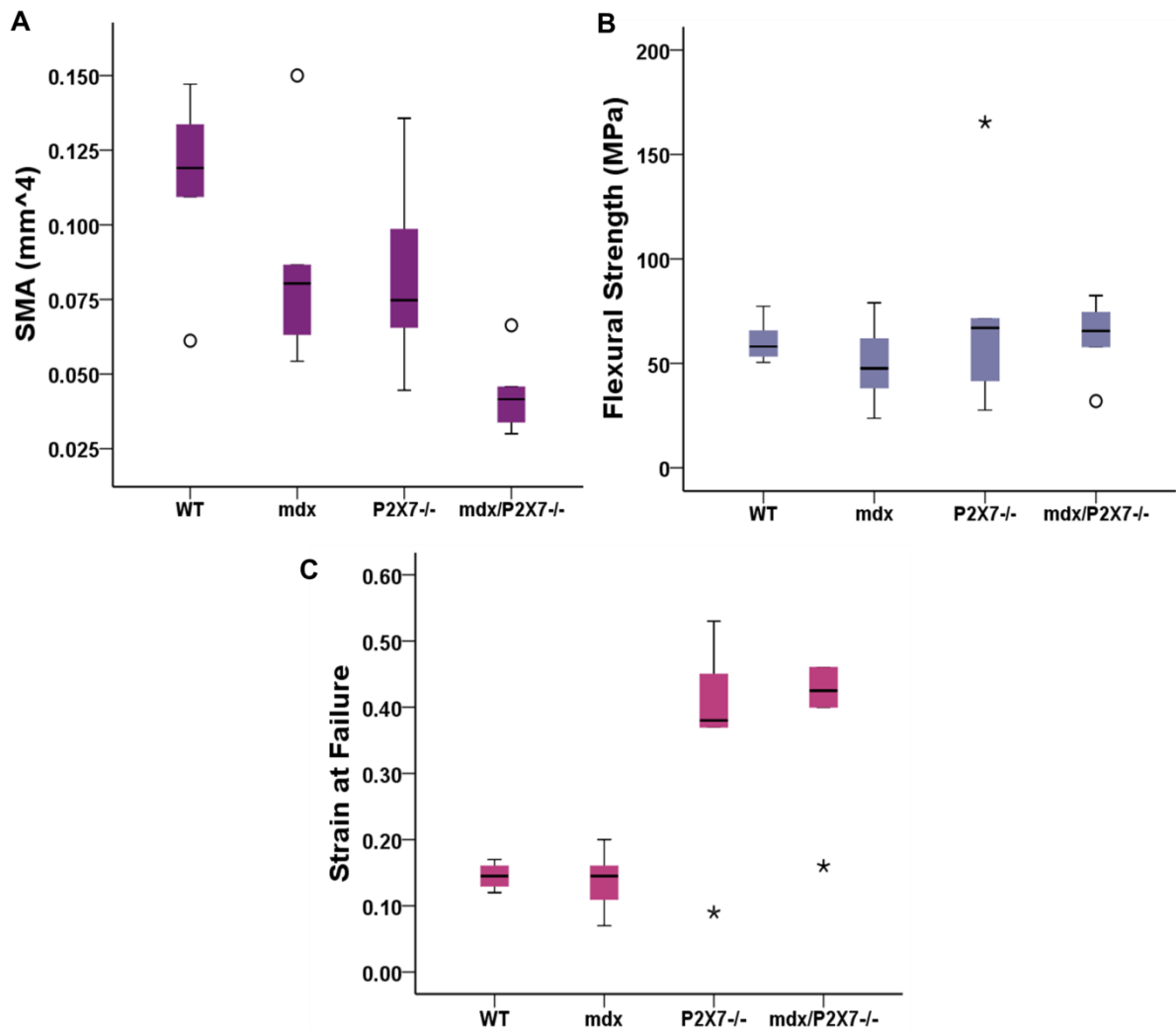
Figure 5-3 A comparison of the mechanical properties of bones obtained from the three-point bending tests.

(A) SMA; (B) flexural strength and (C) strain at failure. The boxplots for the four genotypes include the medians, the 25th and 75th percentiles and the outliers.

5.2.2 Alterations in mechanical properties of *mdx*/P2X7$^{-/-}$ mice.

Post-yield stress-strain curves (Figure 5-1) clearly show that the *mdx*/P2X7$^{-/-}$ mice had a greater strain to failure than most of the other types, including *mdx*. Greater strain to failure is inversely related to the brittleness of the bone. Hence, the *mdx*/P2X7$^{-/-}$ mice showed ductile behaviour compared with the other genotypes. Significantly lower stiffness was found in *mdx*/P2X7$^{-/-}$ compared to *mdx* (by 53%, p=0.010), WT (72%, p=0.004) and P2X7$^{-/-}$ (61%, p=0.004) mice (Table 5-1).

126

Although the average maximum load achieved in *mdx*/P2X7$^{-/-}$ was relatively lower than that of *mdx* (mdx/P2X7$^{-/-}$=2.43±0.45 vs mdx=3.10±0.90) and WT mice (mdx/P2X7$^{-/-}$=2.43±0.45 vs WT=4.99±0.89), the average flexural strength in *mdx*/P2X7$^{-/-}$ mice was relatively higher than that of *mdx* (62.97±17.39 vs 49.65±19.09), due mainly to the significantly lower SMA in the former (p=0.010) (Figure 5-4). A significant deficit in SMA was observed in *mdx*/P2X7$^{-/-}$ mice compared to those of WT (p=0.010), *mdx* (p=0.010) and P2X7$^{-/-}$ (p=0.016). Significantly higher strain at failure was obtained in the *mdx*/P2X7$^{-/-}$ mice compared with those of both WT (by 60%, p=0.008) and *mdx* mice (by 79%, p=0.008), indicating greater ductility and resistance to fracture.
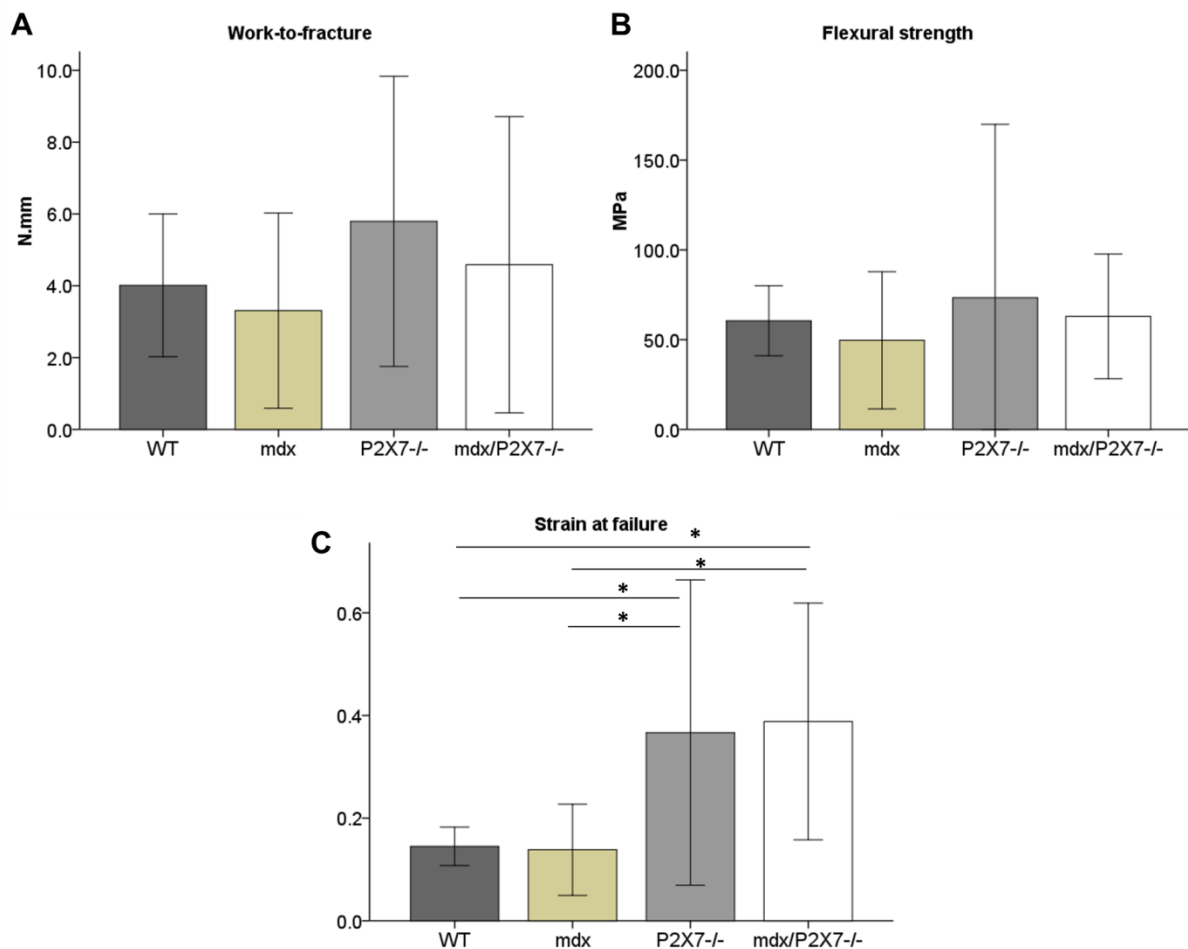
Figure 5-4 Three-point bending results in *mdx*/P2X7$^{-/-}$ mice measures of (A) Work-to-Fracture, (B) Flexural Strength; (C) Strain at Failure.
The *mdx*/P2X7$^{-/-}$ mice displayed significantly greater strain at failure, indicative of ductile bone; however, they did not display significantly greater work-to-fracture and flexural strength.

It seems that the measured low maximum load and stiffness in the *mdx*/P2X7$^{-/-}$ mice did not translate into low material properties (Figure 5-2). In fact, relatively higher average flexural strength and work-to-fracture were found in the *mdx*/P2X7$^{-/-}$ mice compared with those of *mdx*, possibly due to the high cortical bone area and fraction (Table 4-2 and Table 4-3), as well as the low SMA, found in the knockout bones (Table 5-1).

5.2.3 Analysis of fracture paths and modes post testing.

Qualitative analysis using scanning electron microscopy (SEM) of the distal tibia post three-point bending test (n=2 per genotype) are shown in Figure 5-5 and Figure 5-6 for typical fracture surfaces in WT, *mdx,* P2X7$^{-/-}$,and *mdx*/P2X7$^{-/-}$ mice.
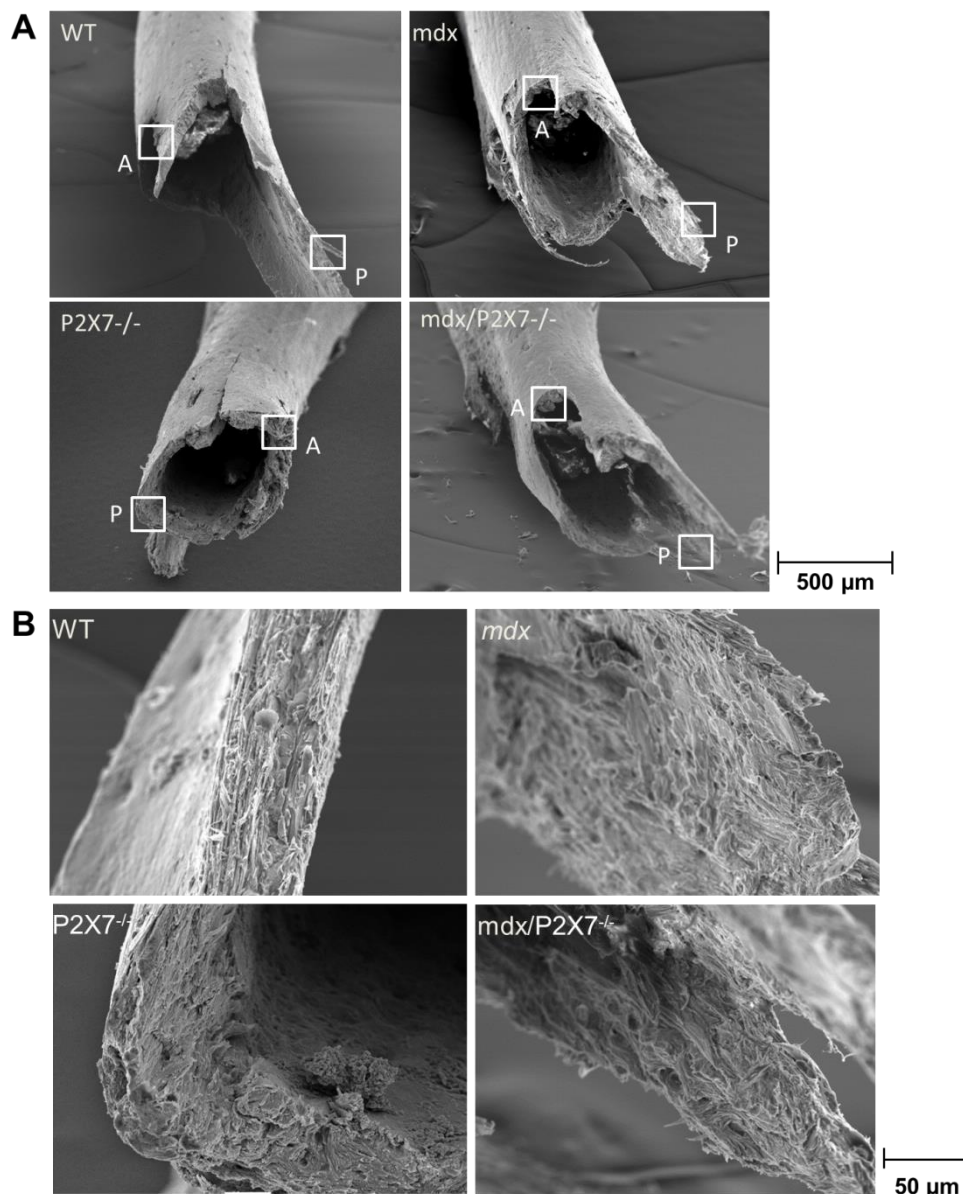
Figure 5-5 Scanning electron micrograph of the fracture surfaces of distal tibias post-three-point bending testing in WT, *mdx*, P2X7$^{-/-}$ and *mdx/*P2X7$^{-/-}$ mice.

(A) Compression and tension were experienced in anterior (A) and posterior (P), respectively. (B) Higher-powered images of the posterior cortex of the bones showing fibrous fracture surfaces in WT and double mutant bones, as opposed to brittle fracture surfaces in *mdx* bone.

The more brittle type of fracture found in *mdx* mice stands in contrast to the more ductile fracture found in the *mdx*/P2X7$^{-/-}$ bones, as well as in the WT bones. The paths of the fracture are indicated in Figure 5-5(A), where instantaneous brittle fracture along the weak planes (posterior surface experienced tension) appears in the *mdx* sample, as opposed to the fibrous fracture surfaces found in the WT and knockout bones, with the latter indicating a gradual separation of the bones as a result of competition between cracking and fibre bridging. Figure 5-5(B) shows the cross-sections of the failed samples, where the posterior surface was in tension and the anterior surface was in compression.

High magnification images at selected resolutions are shown in Figure 5-6 to reveal the micro-fracture mechanisms in the posterior area, where maximum tension led to the initiation of cracks. It seems that rougher fracture surfaces characterise the samples of WT, P2X7$^{-/-}$ and *mdx*/P2X7$^{-/-}$, as opposed to relatively smoother fracture surfaces in the *mdx* bones. Pulling out of collagen fibrils can be observed in all genotypes, but particularly in P2X7$^{-/-}$ and mdx/P2X7$^{-/-}$, which also show twisted collagen fibrils. The twisted collagen fibrils are attributed to the presence of interface areas or empty spaces that may interrupt the propagation of cracks. Whilst pull-out collagen fibrils were a reaction towards large traction force produced during crack growth. The observation seems to be consistent with the results presented in Table 5-1, Figure 5-1 and Figure 5-4 where higher values of strain at failure and work-to-fracture are obtained from the *mdx*/P2X7$^{-/-}$ bones compared with those from the *mdx* bones.
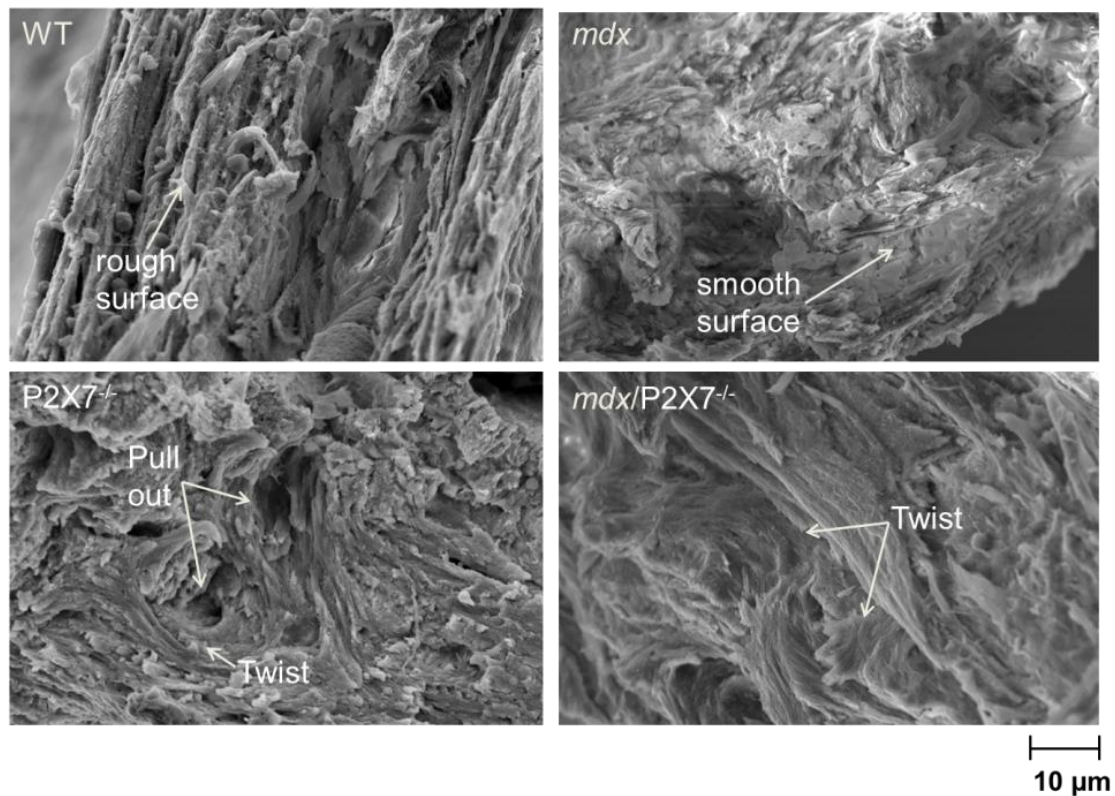
Figure 5-6 Representative SEM images show microarchitecture features of fractured surfaces.
Magnified images of the cortical regions reveal a smooth surface and looser microarchitecture features in *mdx* mice when compared with WT mice. Apparent fibrous texture was clearly observed in WT and knockout mice, where pull-out and twist bone tissues were indicated.

5.3 Discussion

Bone health remains a substantial concern in DMD. Approximately 20% of ambulant males and 27% of those using orthoses have been found to lose mobility permanently as a result of fracture (McDonald et al., 2002). The lower-limb long bones were found to be the most commonly affected bones in significantly young DMD patients in terms of increased rate of fracture (Morgenroth et al., 2012). Therefore, the tibia was used in the current study for morphometric and biomechanical analysis. This is the first time that P2RX7 receptor knockout mice have been used for modelling the DMD bone phenotype.

A major finding of the current study is the significant deficit in mechanical properties of bone seen in the *mdx* mice. The mechanical test has been performed on a four-week-old P2RX7 receptor knockout mouse model. Anderson et al. (1993) studied the WT and *mdx* mouse model at different ages (4 weeks, 12 weeks and 18 weeks). The deficiencies in mechanical properties noted in *mdx* mice were profound (38% reduction in maximum load and 41% in stiffness) compared with those of WT. This could explain the occurrence of low-energy fractures reported in DMD patients (Vestergaard et al.; 2001, Chan et al., 2011; Pouwels et al., 2013).

Most significantly, the mechanical properties of the *mdx*/P2X7$^{-/-}$ bones also changed, and the knockout bones are found to be more ductile compared with those of *mdx*. A 28% increase in work-to-failure, 21% increase in flexural strength and 64% increase in strain at failure are found in the *mdx*/P2X7$^{-/-}$ mice compared with those of *mdx* (Figure 5-4). Moreover, *mdx*/P2X7$^{-/-}$ bones are found to have higher values for the above properties when compared with that of WT and have approximately close values to P2X7$^{-/-}$ bones. These findings are encouraging in supporting our original hypothesis of the role of P2RX7 receptor. These changes might be attributed to the substantially higher cortical bone area and cortical area fraction of the *mdx*/P2X7$^{-/-}$ bones. These results suggest that the *mdx*/P2X7$^{-/-}$ bones are stronger and more resistant and therefore less susceptible to fracture. Although the strength of the double mutant bones did not improve significantly compared with that of the *mdx*, the improvement in strain to failure in these bones is quite remarkable. The *mdx*/P2X7$^{-/-}$ mice showed a lower maximum load values of 22% and stiffness values of 53% (p=0.010) compared to age-matched WT mice, while the P2X7$^{-/-}$ mice showed improvement in all mechanical parameters compared to *mdx*, but no improvement in SMA values. However, none of these measures are statistically significant (Table 5-1).

Mechanically, the average flexural strength in *mdx*/P2X7$^{-/-}$ mouse bones improved due to the reduced moment of inertia of smaller bones compared to that of *mdx*, despite an apparent reduction in the measured maximum load (Table 5-1). More importantly, the improved work-to-fracture and the significantly increased strain to failure indicate a marked improvement in ductility for the *mdx*/P2X7$^{-/-}$ mouse bones over that *mdx*. On the other hand, the slightly different bone phenotypes in P2X7$^{-/-}$

and *mdx*/P2X7^{-/-} may indicate some interplay between this receptor and the dystrophin absence. Further studies are needed to explore the expression of dystrophin in bone cells and its possible impact on the functions of P2RX7 receptors in this tissue.

This study has several limitations. Specifically, the complex bone geometry (i.e non-uniform cross-section of the bone) may be a factor that limits the accuracy of the results. However, several assumptions underlie the use of beam theory. They are (a) the beam should be made from a homogeneous, linear-elastic, material, (b) the beam should have a uniform cross-section, and (c) it should be long in proportion to its depth (Young and Budynas, 2002). These assumptions are well known and have been identified as potential errors in the three-point bending test as it is clear that they are not met for the mouse bone (van Lenthe et al., 2008). Indeed, it is also noted greater variance in this test than in the other biomechanical tests, which may limit our ability to resolve subtle changes in mechanical parameters. Nevertheless, this test has been used in similar mouse models to show deficits in tibia integrity (Nakagaki et al., 2011; Novotny et al., 2011). Furthermore, in this work the specimens were fixed in phosphate buffered formal saline (PBFS) solution for long term storage with limited tissue shrinkage for CT scanning and mechanical testing. Although fixing bone samples in formalin is one of the common fixation methods for microscopic studies, there have been reports on the variation of the strength measured in embalmed samples, possibly due to an increase in collagen cross-linking. Nevertheless, as the same fixation method was used for all the samples examined here, the relative values of mechanical properties obtained should be useful for comparison purposes.

An important finding of the current study is the improvements in cortical bone mechanical properties due to the ablation of the P2RX7 receptor in dystrophic mice. This finding mirrors the improvements seen in dystrophic muscle and non-muscle symptoms (Sinadinos et al., 2015).

Quantitative assessments of the strength and toughness of small animal bones may be carried out using a number of approaches (Jepsen et al., 2015; Ritchie et al., 2008). In terms of toughness, both work-to-fracture and fracture toughness may be used. Work-to-fracture has the advantage of measuring both strength and toughness

using the same un-notched specimen at the same time, although the measured properties are usually size-dependent. Fracture toughness measurements require a pre-crack or sharp notch, which is considered best suited for controlled fracture tests (Ritchie et al., 2008) for characterising the inherent resistance of a material to fracture. In this work, we adopted the former due to the similar sizes of the samples across phenotypes; for convenience; and to ensure a lack of ambiguity of the measured mechanical properties in terms of strength, stiffness and work-to-fracture. Our approach follows the guidelines of Jepsen et al. (2015) with respect to assessing the mechanical properties of mouse bones.

A variety of toughening mechanisms (Li et al., 2013), such as bridging, might be at work, giving rise to the ductile behaviour observed particularly in *mdx*/P2X7$^{-/-}$ bones. A twisting and pulling-out of collagen fibrils in response to the external force were observed. This may interrupt the propagation of cracks, resulting in higher resistance to fracture and greater strain to failure. These findings are quite encouraging and potentiate our hypothesis regarding P2RX7 receptor knockout of the DMD bone phenotype.

These results suggest that the bone abnormalities present in DMD mouse model might be reversible by the ablation of the P2RX7 receptor. It has also been found that significant amelioration of the symptoms of DMD can be achieved from the blockade of the P2RX7 receptor in the DMD mouse model (Sinadinos et al., 2015).

The primary organic component of the bone matrix is type 1 collagen. An alteration in the type 1 collagen may affect the mechanical behaviour of the bone structure (Vashishth, 2007). The reduction in mechanical properties of the *mdx* mice bone might be attributed primarily to poorer organization of collagen fibers and reduced collagen content. A similar bone condition in the *oim* model of osteogenesis imperfecta and bone fragility (SAMP6) has mutated collagen leading to reduction in bone strength. Lower collagen content might be a feature of the lower stiffness and flexural strength in mdx mice bone at microstructural level (Silva et al., 2006).

The results obtained from the mechanical test study are quite encouraging, in terms of the improvement in certain mechanical properties in *mdx*/P2X7$^{-/-}$ mice. These, together with improved bone volume, would suggest improved bone integrity when

the P2RX7 receptor is switched off. Further exploration is needed with respect to the mechanism by which the P2RX7 receptor causes the improvements. A further experiment to explore the tissue properties of the genotypes under study will be discussed in the next chapter.

Chapter 6

Analysis of bone tissue properties across the genotypes using nanoindentation

6.1 Introduction

Nanoindentation is a tool to characterise bone material tissue properties in the sub-micron range. In addition to measuring the basic hardness values, depth-sensing indentation has been routinely used to extract the elastic properties of bone, with known indenter geometry and material properties.

The results from the previous chapters suggest that there are likely to be alterations in bone material properties in mdx/P2X7$^{-/-}$ mice. In the current experiments, it was hypothesised that alterations in material tissue properties may explain the changes in the morphological and mechanical properties observed in the mdx mouse model and P2RX7 ablation. Thus, the specific aim of the experiment reported in this chapter was to determine the tissue properties of bones in P2RX7 knockout in mdx mice, mdx/P2X7$^{-/-}$, compared to those of WT, mdx and single knockout mice (P2X7$^{-/-}$). The objective is to explore potential receptor-related deficiencies in material properties of bone at the bone matrix level. It is also aim to establish whether compared with possibly altered and deteriorated properties of mdx mice, the properties of mdx/P2X7$^{-/-}$ are somewhat reversed as far as the elastic and viscoelastic behaviour is concerned.

6.2 Results

Following the morphometric and three-point bending analysis, nanoindentation was conducted and the results are presented as the mean ± standard deviation (SD) for each group of samples (n=6 per genotype). Significant difference was assessed by a non-parametric Kruskal–Wallis test for advanced (standard) and sinus (dynamic) indentations. A statistically significant difference was indicated by $p < 0.05$. A comparison of the properties is made between mdx/P2X7$^{-/-}$ and WT=a, mdx=b, P2X7$^{-/-}$=c. The comparison of genotypes will be discussed based on WT (control),

135

mdx, P2X7$^{-/-}$ (P2RX7 single knockout) and *mdx*/P2X7$^{-/-}$ (P2RX7 and *mdx* double knockout) mice.

6.2.1 Cortical bone tissue properties in WT and *mdx* mice from the advanced loading protocol.

Table 6-1 shows the mean and the SD of nanoindentation parameters from the advanced protocols. For cortical bones, statistically significant differences in the hardness (p=0.028), indentation modulus (p=0.007), elasticity (p=0.000) and creep (p=0.000) were observed between the *mdx* and WT mice. Significantly lower hardness (by 4.3%) and elasticity (the elastic part of the indentation work, by 11.1%), but higher creep (by 15.6%) and modulus (by 6%) were found in the *mdx* mice compared to in the WT mice.

6.2.2 Trabecular bone tissue properties in WT and *mdx* mice from the advanced loading protocol.

For trabecular bones, there seemed to be no significant differences between the properties of WT and *mdx* mice. Approximately similar values in elasticity and creep were obtained across the genotypes, although differences were found between hardness and modulus between the knockout and WT bones. The average values for the latter two properties were higher in knockout mice compared to those of *mdx*, although not statistically significant. Compared with the *mdx* mice, WT mice have lower advanced nanoindentation property values, except for elasticity, which is slightly higher in WT than that in *mdx* mice (24.58±2.86 vs. 24.40±3.56, %).

Table 6-1 Nanoindentation results produced by using the 'advanced' loading protocol for the tissue properties of the mouse bones.

Material properties	WT	*mdx*	P2X7$^{-/-}$	*mdx*/P2X7$^{-/-}$
Cortical Advanced				
Hardness (MPa)	643.65±66.62	**616.27±57.42^a**	628.36±57.36	**637.89±49.58^b**
Ind. Modulus (GPa)	17.28±1.91	**18.31±1.52^a**	**16.87±1.22^b**	**17.44±1.28^{b,c}**
Elasticity (%)	22.88±2.25	**20.34±2.12^a**	**22.76±2.75^b**	**22.63±2.59^b**
Creep (%)	5.89±1.05	**6.81±1.15^a**	**6.02±1.23^b**	**5.92±0.91^b**
Trabecular Advanced				
Hardness (MPa)	437.14±104.63	475.65±97.37	**523.46±98.60^a**	**505.79±102.47^a**
Ind. Modulus (GPa)	10.97±1.87	11.77±2.18	**12.56±1.98^a**	**12.48±2.07^a**
Elasticity (%)	24.58±2.86	24.40±3.56	24.93±4.80	24.40±3.60
Creep (%)	6.53±1.08	6.77±1.90	6.18±2.17	6.55±1.58

^{a,b,c} and **bold text** indicate p<0.05 (Kruskal–Wallis).
^{a} Statistically significant difference (<0.05) with WT.
^{b} Statistically significant difference (<0.05) with *mdx*.
^{c} Statistically significant difference (<0.05) with P2RX7$^{-/-}$.

6.2.2 Cortical bone tissue properties in *mdx*/P2X7$^{-/-}$ mice from the advanced loading protocol.

For cortical bones, statistically significant differences in the hardness, indentation modulus, elasticity and creep were observed between the *mdx*/P2X7$^{-/-}$ and the *mdx* mice. Lower modulus (p=0.003, by 4.8%) and creep (p=0.000, by 13%), but higher hardness (p=0.040, by 3.5%) and elasticity (p=0.000, by 11.3%), were found in the *mdx*/P2X7$^{-/-}$ compared to those in the *mdx* mice; hence, the double-mutant mice showed properties closer to those of WT than those of *mdx*. For example, the

elasticity in *mdx*/P2X7$^{-/-}$ mice was significantly higher than that of *mdx* mice, but close to that of WT and P2X7$^{-/-}$.
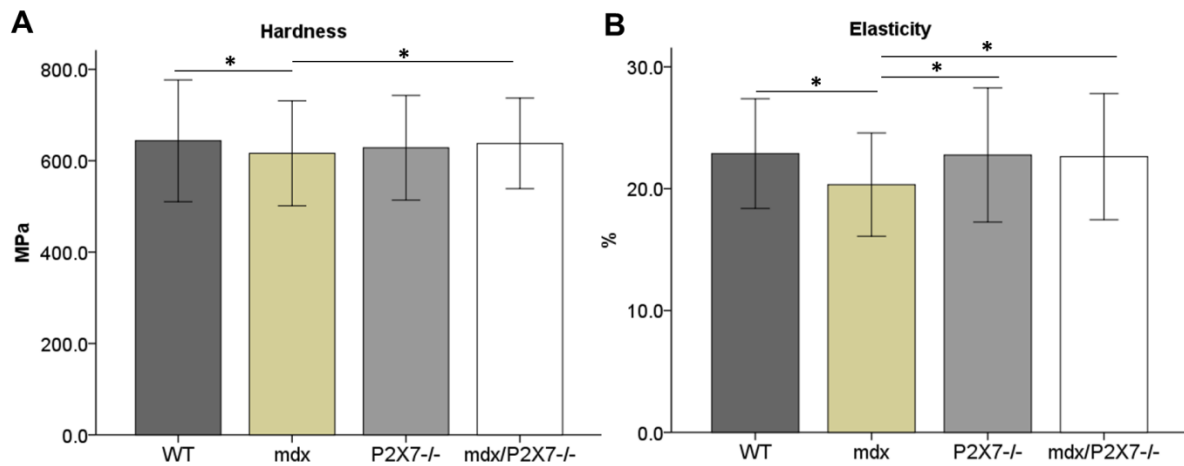
Figure 6-1 Comparison of hardness (A) and elasticity (B)**.**
Bar charts show hardness (A) and elasticity (B) across the genotypes. Star (*) shows statistically significant difference.

For P2X7$^{-/-}$ cortical bones, statistically significant differences were observed in all advanced properties except for hardness (p>0.05). The advanced loading properties were found to have no difference with those of WT whilst there were differences between P2X7$^{-/-}$ and *mdx* mice. P2X7$^{-/-}$ mice were observed to have a similar trend to the mdx/P2X7$^{-/-}$ in contrast with the *mdx*. Significantly lower indentation modulus (p=0.000) and creep (p=0.005) were found in the P2X7$^{-/-}$ mice compared to those of the *mdx* mice, whilst significantly higher elasticity (p=0.000) was observed in the former.

6.2.3 Trabecular bone tissue properties in *mdx*/P2X7$^{-/-}$ mice from advanced loading protocol.

For trabecular bones, there seemed to be no significant differences between the properties of *mdx*/P2X7$^{-/-}$ and *mdx* mice. Quantitatively, the *mdx*/P2X7$^{-/-}$ trabecular bones show higher average hardness and indentation modulus compared to those of the *mdx* bones whilst elasticity (% of elastic to total work) seemed to be of similar value. Lower creep was found in the *mdx*/P2X7$^{-/-}$ mice (6.55±1.58 vs 6.77±1.90, %) than that of *mdx*. The *mdx*/P2X7$^{-/-}$ bones show significantly higher hardness (p=

0.006, 505.79±102.47 vs. 437.14±104.63) and indentation modulus (p= 0.014, 12.48±2.07 vs. 10.97±1.87) than those of the WT mice. No significant differences were observed for elasticity (n_{IT}) and creep (C_{IT}) between those of *mdx*/P2X7$^{-/-}$, WT or *mdx* mice.

A Pearson's correlation analysis was conducted to investigate the relationship between creep and elasticity, as shown in Figure 6-2 and Figure 6-5. They show that creep decreases with the increase in elasticity for all WT, *mdx* and *mdx*/P2X7$^{-/-}$ bones. The negative correlations between creep and elasticity are shown in Figure 6-2 for cortical bones, and Figure 6-3 for trabecular bones. Figure 6-2 (Cortical bone) shows WT (R2= 0.590) and *mdx*/P2X7$^{-/-}$ (R2= 0.530) bones produced lower R2 value than that of *mdx* (R2= 0.652). The variability of the data around the two regression lines was approximately identical for (a) and (b). The results seem to suggest that P2RX7$^{-/-}$ ablation reverses, to a large extent, the effects of the dystrophic abnormality; thus, the tissue response of *mdx*/P2X7$^{-/-}$ bones is close to that of WT bones.
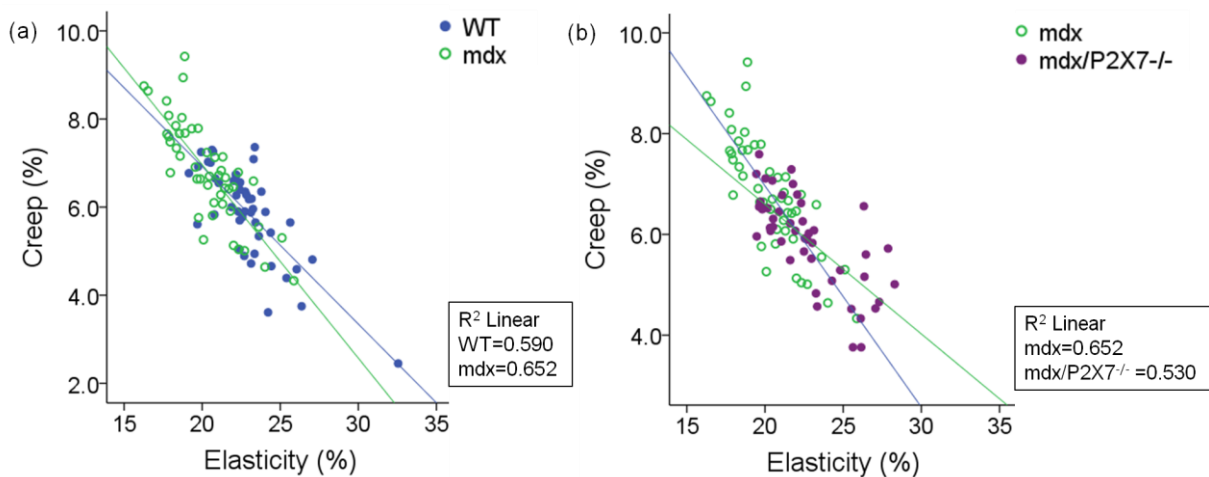
Figure 6-2 The correlation between creep and elasticity.
The linear regression graphs show the cortical bones of (a) WT and *mdx* and (b) *mdx* and *mdx*/P2X7$^{-/-}$ from the advanced nanoindentation.

For cortical bone, indentation hardness, modulus and creep are broadly correlated with the elasticity, although in some cases weakly (WT). The elasticity is positively correlated with the hardness, but negatively correlated with the indentation modulus

and creep. Highly significant negative correlations are found between elasticity and creep.

Further correlation analyses were used to analyse relationships as shown in Table 6-2. A similar trend exists for the *mdx* and the *mdx*/P2X7$^{-/-}$ mice (p<0.01). Figure 6-3 (Trabecular bone) shows that there are strong negative correlations between the creep and the elasticity in *mdx* (R=-0.720, p=0.000) and *mdx*/P2X7$^{-/-}$ (R=-0.843, p=0.000), as opposed to WT (R=0.173, p=0.388) trabecular bones. The relationships between creep and elasticity of the *mdx* (R=-0.720, p=0.000) and *mdx*/P2X7$^{-/-}$ bones are almost identical.

Table 6-2 Correlations between some of the advanced nanoindentation parameters.

Advanced			Hardness (MPa)	Indentation Modulus (GPa)	Creep (%)
Cortical					
Elasticity (%)	WT	**R**	0.317*	-0.436**	-0.768**
		p	0.028	0.002	0.000
	mdx	**R**	0.646**	-0.309*	-0.808**
		p	0.000	0.033	0.000
	P2X7$^{-/-}$	**R**	0.671**	-0.526**	-0.852**
		p	0.000	0.000	0.000
	mdx/P2X7$^{-/-}$	**R**	0.641**	-0.668**	-0.728**
		p	0.000	0.000	0.000
Trabecular					
Elasticity (%)	WT	**R**	0.064	-0.390*	0.173
		p	0.750	0.045	0.388
	mdx	**R**	0.242	-0.384*	-0.720**
		p	0.224	0.048	0.000
	P2X7$^{-/-}$	**R**	0.810**	-0.360	-0.896
		p	0.000	0.065	0.000
	mdx/P2X7$^{-/-}$	**R**	0.563**	-0.255	-0.843**
		p	0.002	0.200	0.000

** Correlation is highly significant at the level 0.01 level (2-tailed)
* Correlation is significant at the level 0.05 level (2-tailed)
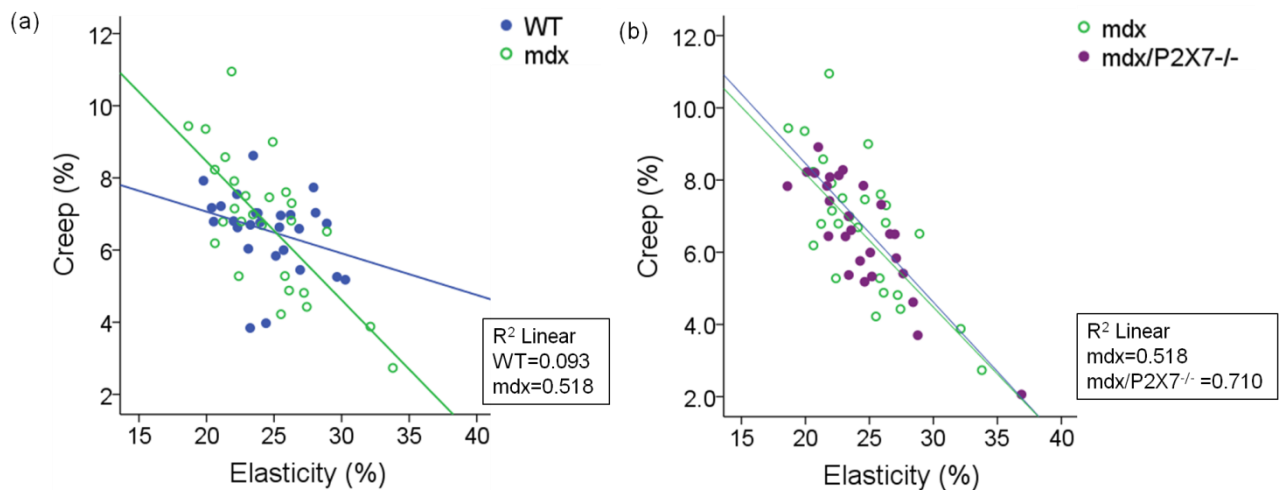
Figure 6-3 Linear regressions between creep and elasticity of trabecular bone of (a) WT and *mdx* and (b) *mdx* and *mdx*/P2X7$^{-/-}$.

6.2.4 Cortical bone tissue properties in *mdx* and WT mice from the sinus loading protocol.

Table 6-3 shows the mean and the SD of nanoindentation parameters from the sinus protocols. For sinus indentation, there were no significant differences between the properties of WT and *mdx* mice except for elasticity. The elasticity in the cortical bones of the *mdx* mice was found to be significantly lower than that of the WT mice (p=0.007). Figure 6-4 also shows that the elasticity in *mdx* mice is significantly lower than that of the P2X7$^{-/-}$ mice (p=0.040).

Table 6-3 Nanoindentation results produced by using the sinus loading protocol for the tissue properties of the mouse bones.

Material properties	WT	*mdx*	P2X7^{-/-}	*mdx*/P2X7^{-/-}
Cortical sinus				
Phase Difference (∂)	3.50±0.61	3.72±1.01	4.14±1.04	**4.13±0.91[a]**
Storage Modulus (GPa)	20.63±2.29	20.13±2.05	19.33±2.19	**21.31±1.86[c]**
Loss Modulus (GPa)	1.28±0.27	1.32±0.32	1.43±0.44	**1.56±0.33[a,b]**
Elasticity (%)	21.36±2.04	**19.36±1.78[a]**	**20.85±2.08[b]**	20.56±2.29
Trabecular sinus				
Phase Difference (∂)	4.75±1.58	4.95±2.42	4.08±1.67	4.23±1.18
Storage Modulus (GPa)	13.61±2.47	**16.92±2.74[a]**	**17.43±2.08[a]**	**15.45±2.42[a,c]**
Loss Modulus (GPa)	1.07±0.46	1.50±0.74	1.24±0.45	1.17±0.41
Elasticity (%)	23.10±3.01	22.53±3.22	24.25±5.09	21.62±3.27

[a,b,c] and **bold text** indicate $p<0.05$ (Kruskal–Wallis).
[a] Statistically significant difference (<0.05) with WT.
[b] Statistically significant difference (<0.05) with *mdx*.
[c] Statistically significant difference (<0.05) with P2RX7^{-/-}.
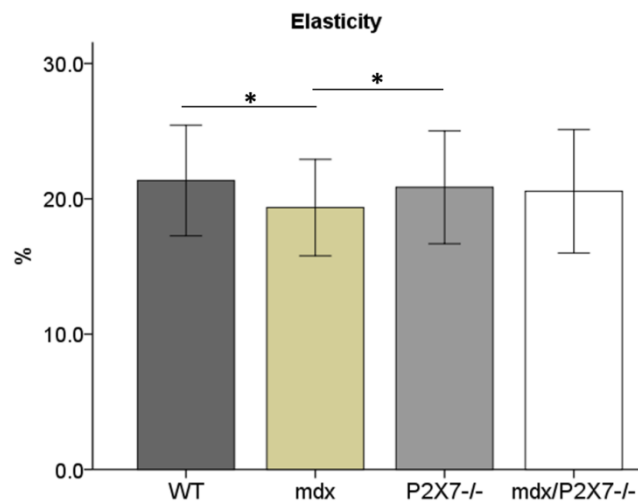
Figure 6-4 Comparison of elasticity for cortical bones from sinus indentation. The percentage elasticity in *mdx* mice is lower compared to that of the WT mice ($p<0.05$), as well as compared to the P2X7^{-/-} mice ($p<0.05$). Star (*) shows statistically significant difference.

6.2.5 Cortical bone tissue properties in *mdx*/P2X7$^{-/-}$ mice from the sinus loading protocol.

Statistically significant differences were found in loss modulus between the *mdx*/P2X7$^{-/-}$ and the *mdx* (p=0.025) and the WT (p=0.014) mice in the cortical bone (Figure 6-5). Otherwise, the average values of elasticity in the *mdx*/P2X7$^{-/-}$ bones appear to be closer to those of the WT and P2X7$^{-/-}$ mice. Although there were no significant differences across the genotypes.
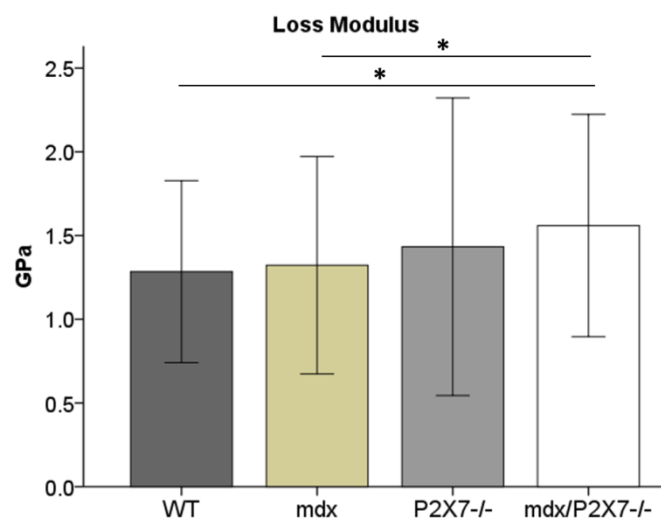
Figure 6-5 Comparison of loss modulus for cortical bones from sinus indentation. Star (*) shows statistically significant difference.

Significant differences were seen in loss modulus between the four comparison genotypes (WT=1.28 ± 0.27, *mdx*=1.32 ± 0.32, P2RX7$^{-/-}$=1.43 ± 0.44, *mdx*/P2RX7$^{-/-}$=1.56 ± 0.33). For P2X7$^{-/-}$ cortical bones, a statistically significant increase in elasticity (p= 0.040, by 8%) was observed compared to that of *mdx*. The average value of sinus indentation properties for most sinus loading protocols were higher for both knockout mice bones compared to that of *mdx*.

6.2.6 Trabecular bone material properties in *mdx* and WT mice from the sinus loading protocol.

A higher storage modulus is found in *mdx* trabecular bones compared to WT bones (p=0.001) (Figure 6-6), whilst no significant difference is observed in other sinus properties. Similar to cortical bones, the elasticity in trabecular bones is positively correlated with the hardness, but negatively correlated with the indentation modulus and creep (except in WT) (Table 6-3).
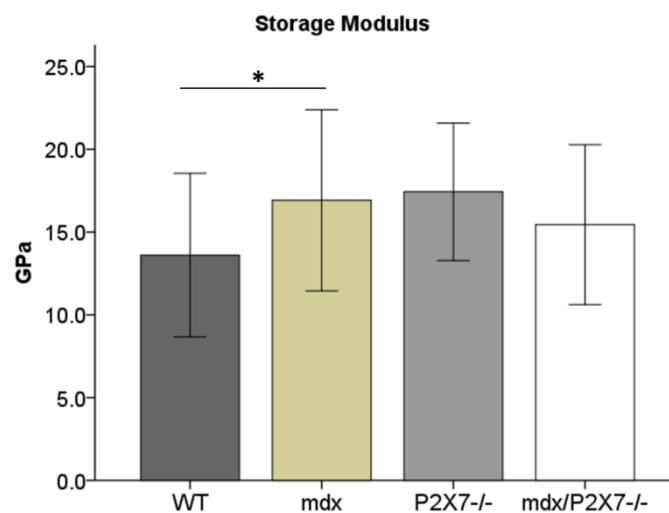
Figure 6-6 Comparison of storage modulus for all genotypes.
The comparison between WT and *mdx* revealed a significant difference, where the *mdx* mice showed a higher storage modulus. Star (*) shows statistically significant difference.

6.2.7 Trabecular bone material properties in *mdx*/P2X7$^{-/-}$ mice from the sinus loading protocol

No significant difference was observed in *mdx*/P2X7$^{-/-}$ trabecular bones as compared to that of *mdx* from sinus indentation. Although a higher storage modulus (p=0.029) was found when compared with that of the WT mice, a lower value (p=0.016) was noted when compared to the P2X7$^{-/-}$ mice. The storage and loss modulus values in *mdx*/P2X7$^{-/-}$ trabecular bones appear to be closer to those of the WT mice.

Significant positive correlations are found between elasticity and hardness in the knockout mice (P2X7$^{-/-}$, R=0.810, p=0.000; *mdx*/P2X7$^{-/-}$, R=0.563, p=0.002), whilst significant negative correlations are found between elasticity and creep in the *mdx* and *mdx*/P2X7$^{-/-}$ models.

The results seem to suggest that P2RX7$^{-/-}$ ablation reverses, to a large extent, the effects of the dystrophic abnormality, thus the tissue responses of *mdx*/P2X7$^{-/-}$ are close to those of WT bones.

6.3 Discussion

A major finding of the current study is the significantly deficient tissue properties of *mdx* mice as compared to other genotypes, as well as an improvement in morphometric and mechanical properties of *mdx*/P2X7$^{-/-}$ mice, indicating the effect of ablation. This is the first time that nanoindentation tests have been performed on *mdx* and P2RX7 ablation mice.

Nanoindentation has made it possible to characterise the quality of bone matrix. The matrix properties, as a result of the composition and organisation of mineralised collagen fibres, together with anatomy, define the mechanical behaviour of the whole bone. In this study, the indents were consistently positioned in the medial surface of the midtibia to obtain the cortical. Due to the heterogeneity of the bone microstructure, the method reduces the measurement variation within the sample (Hengsberger et al., 2002; Zysset et al., 1999). Precise and selective positioning of the indentor in the heterogeneous bone microstructure (i.e. on thick or thin lamellae; on interstitial or osteonal matrix) might help in some cases to reduce data variation (Finnila et al., 2010).

The nanoindentation was carried out in dry conditions, which is a common practice adopted for easy comparison with the published work, and to reduce the influence of factors such as noise and hydration state of the bones. Although the modulus measured in the wet condition is known to be about 10–20% lower than that in dry, this is not considered an issue for comparison purposes.

The deficiencies in the *mdx* cortical bone matrix are evident (4.3% lower hardness, 11.1% lower elasticity and 15.6% higher creep than those of the WT mice), and these could explain the occurrence of low energy fractures reported in DMD patients. Nanoindentation data showed, for the first time, the tibias of *mdx* mice to be more brittle and less able to store energy compared to the WT bones (Table 6-3). There is evidence that the bone tissue is also significantly affected in DMD at an early stage of the disease before the muscle fibers are fully developed. These results are consistent with the report by Nakagaki et al. (2010) who demonstrated biochemical and mechanical properties alteration at 21 days of age. Overall the properties of the *mdx*/P2X7$^{-/-}$ cortical bone matrix are significantly better than those of the *mdx* bones (3.5% hardness, 11.3% elasticity, 11% phase difference, 6% indentation modulus and 18% loss modulus). The *mdx*/P2X7$^{-/-}$ trabecular bone matrix seems to follow a similar trend, although no statistically significant difference is observed.

The *mdx*/P2X7$^{-/-}$ mice, in which P2RX7 is switched off, revealed a significant increase in cortical bone mechanical properties (strain at failure, flexural strength and work-to-fracture) as compared to *mdx* mice. Furthermore, the tissue properties revealed significant increases in hardness, elasticity, phase difference, storage and loss modulus (cortical bone), and hardness and indentation modulus (trabecular bone).

An extensive analysis of osteogenic markers reported by Rufo et al. (2010) suggests the overall downregulation of many transcripts in DMD has reduced the ability of osteoblasts to mineralise. In the thesis, the influence of bone mineralisation, where an increase in the mineral content of the matrix increases both the indentation modulus and hardness, is observed in both knockout mice bones (*mdx*/P2X7$^{-/-}$: 10.82±1.17, % and P2X7$^{-/-}$: 11.45±0.07, %) as compared to those of the *mdx* mice (9.53±0.43,%). Additionally, an increase in the mineral content reduced the plasticity of the bone, the viscoelasticity (i.e., increased storage modulus/decreased loss modulus) and the overall creep strain magnitude. The increase in mineralization resulted in a stiffer material with improved matrix strength. The increased storage modulus (cortical bone) increased the viscoelasticity, while high collagen concentrations were related to a decreased loss modulus.

The loss modulus is significantly higher in the cortical bone of the *mdx*/P2X7$^{-/-}$ mice, and slightly higher, though not significantly so, in P2X7$^{-/-}$ mice when compared with those of *mdx* mice, suggesting a relatively higher collagen–mineral ratio in P2RX7 knockout bones, most likely as a consequence of increased mineralisation. The trabecular bone architecture seems to be unaffected, except the significantly reduced storage modulus compared to those of the WT and P2X7$^{-/-}$ mice.

The current data demonstrate that the relationship between bone matrix material properties and mineralisation across the genotypes principally follow the same general pattern. Our results suggest that P2RX7 ablation has improved the tissue properties of the *mdx* mice bones. The macroscopic changes in bone morphometric and biomechanical properties had a significant adverse effect on the mechanical outcome. At the micromechanical level, the data show severity in bone changes for the *mdx* mice, and a positive effect on the P2RX7 knockout mice.

As a composite material, the fracture toughness and strength of bone are related. A decrease in mineral content, or an increase in porosity and disorganisation (isotropy in micro-architecture and layout of fibrils) is associated with the decrease in hardness and the modulus of elasticity.

Bone remodelling involves replacing old bone tissues with new ones. A high remodelling rate results in undermineralisation, which makes the bone less stiff, while low remodelling results in a higher mineralization level, causing bones to be more brittle (Seeman, 2008).

Taken together, for the first time, this study demonstrates tissue properties of DMD bone and P2RX7 knockout models as evaluated by nanoindentation at the bone matrix level. The ablation of P2RX7 has resulted in a mechanically stronger bone matrix that is able to store more energy than *mdx* mice.

Chapter 7

Conclusions

The effects of P2RX7 ablation on bone morphometric, mechanical and tissue properties have been studied using imaging, biomechanical and nanoindentation techniques. Four genotypes have been examined, including WT, *mdx*, P2X7$^{-/-}$ and *mdx*/P2X7$^{-/-}$ mice. The objective of the experiments was to examine if the ablation of P2RX7 in dystrophic mice will result in improving bone phenotypes. Male *mdx* mice are considered the most appropriate pre-clinical model to test treatment efficacy for DMD, as this dystrophin-mutant mimics the pathology seen in human DMD.

The study has provided some important information for future genetic therapeutic interventions that are likely to impact on bone phenotypes. In this chapter, the major findings are summarised, together with limitations and possible future work.

7.1. Major findings of the study

Morphometric properties

- In cortical bones, *mdx* mice have lower values of total cross-sectional area inside the periosteal envelope (Tt.Ar), cortical bone area (Ct.Ar), cortical area fraction (Ct.Ar/Tt.Ar) and cortical thickness (Ct.Th) compared to those of WT mice, although the difference was only statistically significant in Ct.Ar and Ct.Th. The findings are in a good agreement with published literature (Anderson et al., 1993; Nakagaki et al., 2011).

- In cortical bones, the morphometric properties of WT and P2X7$^{-/-}$ bones at four weeks are not significantly different.

- In cortical bones, significantly more bone per area/per volume is found in *mdx*/P2X7$^{-/-}$ mice than in all other types, as indicated by the significantly higher cortical bone area (Ct.Ar) and cortical bone area ratio (Ct.Ar/Tt.Ar). However, the ablation of P2RX7 led to smaller bones, with significantly lower cross-sectional area (Tt.Ar) and SMA in *mdx*/P2X7$^{-/-}$ mice than the other types.

- In trabecular bones, the *mdx* mice are found to have significantly lower bone volume fraction (BV/TV) and trabecular thickness (Tb.Th) compared to those of

WT. These results are similar to those reported in the literature (Nakagaki et al., 2011).

- In trabecular bones, no significant difference between P2X7$^{-/-}$ and WT is noted except for the trabecular space, which is found lower in P2X7$^{-/-}$ bones.
- In trabecular bones, significantly higher BV/TV is found in *mdx*/P2X7$^{-/-}$ mice. The ablation of P2XR7 does not seem to affect the trabecular bone architecture, as indicated by the similar values of Tb.Th, trabecular spacing (Tb.Sp) and connectivity (Conn.D).

Mechanical properties

- Mechanical analysis has revealed a low maximum load, stiffness, work-to-fracture, flexural strength and second moment of area (SMA) in *mdx* mice compared to those of WT mice. These findings suggest that the *mdx* bones are weaker and prone to fracture, consistent with increased incidence of fracture in DMD patients.
- No significant difference between P2X7$^{-/-}$ and WT mice is noted in mechanical properties, except for stiffness, which is significantly lower in P2X7$^{-/-}$ compared to that in WT.
- The significant improvement in strain at failure in *mdx*/P2X7$^{-/-}$ over *mdx* mice (by 64%) seemed to suggest greater ductility in *mdx*/P2X7$^{-/-}$ mice; whilst higher average values of work-to-failure and flexural strength are found than those of *mdx* (by 28% and 21%, respectively), although not statistically significant.

Tissue properties

- In cortical bones, significantly lower hardness and elasticity, but higher creep and modulus are found in the *mdx* mice compared to those of the WT mice in both nanoindentation loading protocols.
- In cortical bones, the advanced and sinus loading properties in P2X7$^{-/-}$ mice are found to have no difference from those of WT.
- The hardness and elasticity in cortical bones of *mdx*/P2X7$^{-/-}$ mice are significantly higher whilst indentation modulus and creep significantly lower than those of *mdx* bones. Thus overall the ablation seems to have improved the bone tissue properties.

- In trabecular bones, no differences are found between the properties of WT and *mdx* mice. However, a higher storage modulus is found in *mdx* compared to that in WT bones. The trabecular bone tissue properties seem to be not affected by the disease at tissue level.

- A similar trend is observed in *mdx*/P2X7$^{-/-}$ and P2X7$^{-/-}$ bones. where no differences are found between the trabecular tissue properties of *mdx*/P2X7$^{-/-}$ and *mdx* mice. Specifically, the average values for hardness and modulus are relatively higher in the knockouts mice compared to those of *mdx*, although not statistically significant. The two properties are also found to be higher in *mdx*/P2X7$^{-/-}$ than in WT trabecular bones. In sinus indentations, the storage and loss modulus in *mdx*/P2X7$^{-/-}$ trabecular bones appear to be closer to those of the WT mice.

Overall

The main finding of the current study and one with therapeutic significance is that the bone anomalies observed in *mdx* mice in terms of cortical bone material and biomechanical properties seem to be rescued by the inactivation of P2RX7, the receptor that is expressed in both osteoblast and osteoclasts. It is noted that the receptor appears to have different roles in bone physiology and in disease states, although the overall effect appears to be positive.

7.2 Limitations

In the current study, µCT was mainly used to obtain 3D images of the bone microstructure facilitating in bone morphometric analysis. Although µCT is considered the gold standard for assessing bone mass (bone mineral density), due to the absence of phantom material of known bone density, a calibration could not be conducted in the laboratory to allow bone mineral density to be measured from the µCT images.

- Another finding is the absence of significant difference in bone mineral density (TGA test). The test was conducted on only two bones per genotype (n=2). Based on the sample size, the measurements were analyzed by conducting

ANOVA tests to compare means of more than two groups. More tests and a power test should be performed to verify the preliminary results obtained here. The preliminary TGA test was conducted to explore the bone tissue composition in these animal models. The bone compositions in mdx/P2X7$^{-/-}$ and P2X7$^{-/-}$ mice seem to be higher in organic, mineral, and water content values than mdx. These findings indicate a need to further explore other possible factors (cellular function and alteration in extracellular matrix) that might be involved in the robust increase of bone strength and structural parameters seen in mdx/P2X7$^{-/-}$ mice.

- In this work the specimens were fixed in phosphate buffered formal saline (PBFS) solution for long term storage with limited tissue shrinkage for CT scanning and mechanical testing.   Although fixing bone samples in formalin is one of the common fixation methods for microscopic studies, there have been reports on the variation of the strength measured in embalmed samples, possibly due to increase in collagen cross-linking. Nevertheless, as the same fixation method was used for all the samples examined here, the relative values of mechanical properties obtained should be useful for comparison purposes.

7.3 Future studies

The aim of this project was to explore the consequence of inactivation of P2RX7 receptor on bone properties in an animal model of DMD. This represents a logical path in reaching the ultimate goal of examining the impact of P2RX7 ablation on the bone properties during the acute disease phase in human, before muscle wasting is fully developed.

- The role of P2RX7 receptor on bone cells (osteoblasts and osteoclasts) has been studied but the results are unclear. To investigate whether ablation affects bone formation or bone resorption would require extensive experimental work in future studies, for example analysis of biochemical markers of bone formation and resorption e.g. tartrate-resistant acid phosphatase (TRAP) staining for osteoclasts.
- Further substantial experimentation to investigate the effects of ablation on mineralization, collagen crosslinking or cortical porosity. Future experimental work may include, for example, testing mineralisation of osteoblasts in culture,

151

- Tibia was a suitable bone for the current study. It was used in order to extend our analysis in the 4 week assessment period of previous studies. Testing either femur or radius would have been a better choice for future studies because they are more uniform in shape.

- In the current study, 4 week old mouse model was used. In future, animal studies may be done to explore the possible effects of P2RX7 on bone mass formation and later on ossification of the bone, using the embryonic and postnatal murine models. These experiments will give a better understanding on the exact time in which the deleterious effects of P2RX7 start impacting bone properties. This will also help in the development of therapeutic strategies and the exact time at which they should be implemented.

- The study serves a potential treatment strategy at the very early phase of disease before the muscle wasting has fully developed. The mechanisms that led to the changes in the bones due to the loss of P2RX7 may be complex and require further studies.

Based on the findings of the study, the altered structural parameters, increased mechanical properties as well as tissue properties in *mdx*/P2X7$^{-/-}$ mice points toward the fact that targeting P2RX7 can attenuate DMD symptoms affecting bone structure in addition to the therapeutic effects in the muscle. Improved knowledge on how P2RX7 is involved in bone metabolism is important to assist directions for prevention and treatment in order to improve bone health in DMD patients.

References

Abel, R., Prime, M., Jin, A, Cobb, J., Bhattacharya, R., 2013. 3D Imaging Bone Quality : Bench to Bedside. Hard Tissue 2, 42.

Abou-Khalil, R., Yang, F., Mortreux, M., Lieu, S., Yu, Y.Y., Wurmser, M., Pereira, C., Relaix, F., Miclau, T., Marcucio, R.S., Colnot, C., 2013. Delayed bone regeneration is linked to chronic inflammation in murine muscular dystrophy. J. Bone Miner. Res. 29, 304–315. doi:10.1002/jbmr.2038

Agrawal, A., Gartland, A., 2015. P2X7 receptors: role in bone cell formation and function. J. Mol. Endocrinol. 54, R75–R88. doi:10.1530/JME-14-0226

Agrawal, A., Gartland, A., Ke, H.Z., Qi, H., Weidema, A F., Zhang, Q., Panupinthu, N., Crawford, D.T., Grasser, W. a, Paralkar, V.M., Li, M., Audoly, L.P., Gabel, C. a, Jee, W.S.S., Dixon, S.J., Sims, S.M., Thompson, D.D., Gartland, A., Agrawal, A., Gartland, A., 2003. Deletion of the P2X7 nucleotide receptor reveals its regulatory roles in bone formation and resorption. Mol. Endocrinol. 17, 1356–67. doi:10.1210/me.2003-0021

Akhter, M.P., Wells, D.J., Short, S.J., Cullen, D.M., Johnson, M.L., Haynatzki, G.R., Babij, P., Allen, K.M., Yaworsky, P.J., Bex, F., Recker, R.R., 2004. Bone biomechanical properties in LRP5 mutant mice. Bone 35, 162–9. doi:10.1016/j.bone.2004.02.018

Alexander, J.M., Bab, I., Fish, S., Muller, R., Uchiyama, T., Gronowicz, G., Nahounou, M., Zhao, Q., White, D.W., Chorev, M., Gazit, D., Rosenblatt, M., 2001. Human Parathyroid Hormone 1–34 Reverses Bone Loss in Ovariectomized Mice. J. Bone Miner. Res. 16, 1665–1673.

Allamand, V., Campbell, K.P., 2000. Animal models for muscular dystrophy: valuable tools for the development of therapies. Hum. Mol. Genet. 9, 2459–2467.

Ammann, P., Rizzoli, R., 2003. Bone strength and its determinants. Osteoporos. Int. 14 Suppl 3, S13–8. doi:10.1007/s00198-002-1345-4

Ammann, P., Rizzoli, R., Bonjour, J.P., Bourrin, S., Meyer, J.M., Vassalli, P., Garcia, I., 1997. Transgenic mice expressing soluble tumor necrosis factor-receptor are protected against bone loss caused by estrogen deficiency. J. Clin. Invest. 99, 1699–1703. doi:10.1172/JCI119333

Amoroso, F., Falzoni, S., Adinolfi, E., Ferrari, D., Di Virgilio, F., 2012. The P2X7 receptor is a key modulator of aerobic glycolysis. Cell Death Dis. 3, e370. doi:10.1038/cddis.2012.105

Analysis of bone by micro-CT General information, n.d.

AnalyzeDirect, 2014. Bone Microarchitecture Analysis Manual Analyze 12.0.

Anderson, J.E., Lentz, D.L., Johnson, R.B., 1993. Recovery from disuse osteopenia coincident to restoration of muscle strength in mdx mice. Bone 14, 625–634.

Ay, M., Kuntzer, T., Pike, M., Av, S., 2009. Glucocorticoid corticosteroids for Duchenne muscular dystrophy. Cochrane Collab.

Bachrach, L.K., 2005. Taking steps towards reducing osteoporosis in Duchenne muscular dystrophy. Neuromuscul. Disord. 15, 86–7. doi:10.1016/j.nmd.2004.10.011

Baiker, M., Snoeks, T.J. A, Kaijzel, E.L., Que, I., Dijkstra, J., Lelieveldt, B.P.F., Löwik, C.W.G.M., 2012. Automated bone volume and thickness measurements in small animal whole-body MicroCT data. Mol. Imaging Biol. 14, 420–30. doi:10.1007/s11307-011-0522-2

Banse, X., Devogelaer, J.P., Holmyard, D., Grynpas, M., 2005. Vertebral cancellous bone turn-over: Microcallus and bridges in backscatter electron microscopy. Micron 36, 710–714. doi:10.1016/j.micron.2005.07.012

Bartling, S., Stiller, W., Semmler, W., Kiessling, F., 2007. Small Animal Computed Tomography Imaging. Curr. Med. Imaging Rev. 3, 45–59. doi:10.2174/157340507779940327

Bassett, D., Currie, P.D., 2010. Identification of a zebrafish model of muscular dystrophy. Clin. Exp. Pharmacol. Physiol. 31, 537–540.

Bayat, S., Apostol, L., Boller, E., Brochard, T., Peyrin, F., 2005. In vivo imaging of bone micro-architecture in mice with 3D synchrotron radiation micro-tomography. Nucl. Instruments Methods Phys. Res. Sect. A Accel. Spectrometers, Detect. Assoc. Equip. 548, 247–252. doi:10.1016/j.nima.2005.03.097

Beaupied, H., Lespessailles, E., Benhamou, C.-L., 2007. Evaluation of macrostructural bone biomechanics. Joint. Bone. Spine 74, 233–9. doi:10.1016/j.jbspin.2007.01.019

Bianchi, M.L., Mazzanti, A., Galbiati, E., Saraifoger, S., Dubini, A., Cornelio, F., Morandi, L., 2003. Bone mineral density and bone metabolism in Duchenne muscular dystrophy. Osteoporos. Int. 14, 761–7. doi:10.1007/s00198-003-1443-y

Bianchi, M.L., Morandi, L., 2008. Duchenne Muscular Dystrophy Evaluating Bone and Mineral Metabolism in Patients with Duchenne Muscular Dystrophy. Eur. Musculoskelet. Rev. 80–83.

Bischoff, D.S., Sakamoto, T., Ishida, K., Makhijani, N.S., Gruber, H.E., Yamaguchi, D.T., 2011. CXC receptor knockout mice: characterization of skeletal features and membranous bone healing in the adult mouse. Bone 48, 267–74. doi:10.1016/j.bone.2010.09.026

Blake, D.J., Weir, A., Newey, S.E., Davies, K.E., 2002. Function and genetics of dystrophin and dystrophin-related proteins in muscle. Physiol. Rev. 82, 291–329. doi:10.1152/physrev.00028.2001

Blank, R.D., 2001. Breaking down bone strength: a perspective on the future of skeletal genetics. J. Bone Miner. Res. 16, 1207–1211. doi:10.1359/jbmr.2001.16.7.1207

Bonifati, M.D., Ruzza, G., Bonometto, P., Berardinelli, A., 2000. A Multicenter Double-Blind Randomized Trial of Deflazacort Versus Prednisone in Duchenne Muscular Dystrophy:Analysis after 2 Years. Muscle Nerve 10, 171–175.

Bonnet, N., Laroche, N., Vico, L., Dolleans, E., Courteix, D., Benhamou, C.L., 2009. Assessment of trabecular bone microarchitecture by two different x-ray microcomputed tomographs: a comparative study of the rat distal tibia using Skyscan and Scanco devices. Med. Phys. 36, 1286–1297. doi:10.1118/1.3096605

Boskey, A.L., 2001. Bone Mineralization, in: Bone Mechanics Handbook. CRC Press LLC Boca Raton, Fluorida, USA, pp. 5–1–5–33.

Boutroy, S., Bouxsein, M.L., Munoz, F., Delmas, P.D., 2005. In vivo assessment of trabecular bone microarchitecture by high-resolution peripheral quantitative computed tomography. J. Clin. Endocrinol. Metab. 90, 6508–15. doi:10.1210/jc.2005-1258

Bouxsein, M.L., Boyd, S.K., Christiansen, B. a, Guldberg, R.E., Jepsen, K.J., Müller, R., 2010. Guidelines for assessment of bone microstructure in rodents using micro-computed tomography. J. Bone Miner. Res. 25, 1468–86. doi:10.1002/jbmr.141

Bozzola, J.J., Russel, L.D., 1999. Electron Microscopy: Principles and Techniques for Biologist. Jones and Bartlett Publishers.

Brandi, M.L., 2009. Microarchitecture, the key to bone quality. Rheumatol. (United Kingdom) 48. doi:10.1093/rheumatology/kep273

Brassey, C. a, Margetts, L., Kitchener, A.C., Withers, P.J., Manning, P.L., Sellers, W.I., 2012. Finite element modelling versus classic beam theory: comparing methods for stress estimation in a morphologically diverse sample of vertebrate long bones. J. R. Soc. Interface 10, 20120823. doi:10.1098/rsif.2012.0823

Bruker microCT, n.d. Analysis of bone by micro-CT General information.

Buie, H.R., Campbell, G.M., Klinck, R.J., MacNeil, J. a, Boyd, S.K., 2007. Automatic segmentation of cortical and trabecular compartments based on a dual threshold technique for in vivo micro-CT bone analysis. Bone 41, 505–15. doi:10.1016/j.bone.2007.07.007

Bulfield, G., Siller, W.G., Wight, P. a, Moore, K.J., 1984. X chromosome-linked muscular dystrophy (mdx) in the mouse. Proc. Natl. Acad. Sci. U. S. A. 81, 1189–1192. doi:10.1073/pnas.81.4.1189

Cervinka, T., Sievänen, H., Lala, D., Cheung, A.M., Giangregorio, L., Hyttinen, J., 2015. Cortical bone detection is comparable between pQCT and HR-pQCT. Bone. doi:10.1016/j.bone.2015.09.015

Chamberlain, J.S., Metzger, J., Reyes, M., Townsend, D., Faulkner, J. a, 2007. Dystrophin-deficient mdx mice display a reduced life span and are susceptible to spontaneous rhabdomyosarcoma. Faseb J 21, 2195–2204. doi:10.1096/fj.06-7353com

Chan, A.L., Juarez, M.M., Shelton, D.K., MacDonald, T., Li, C.-S., Lin, T.-C., Albertson, T.E., 2011. Novel computed tomographic chest metrics to detect pulmonary hypertension. BMC Med. Imaging 11, 7. doi:10.1186/1471-2342-11-7

Chappard, D., Blouin, S., Libouban, H., Baslé, M.F., Audran, M., 2005. The visualization and evaluation of bone architecture in the rat using three-dimensional X-ray microcomputed tomography. Microsc. Anal. 19, 19–21.

Chen, H., Yao, X.F., Emura, S., Shoumura, S., 2006. Morphological changes of skeletal muscle, tendon and periosteum in the senescence-accelerated mouse (SAMP6): A murine model for senile osteoporosis. Tissue Cell 38, 325–335. doi:10.1016/j.tice.2006.08.001

Chen, S., Feng, J., Bao, Q., Li, A., Zhang, B., Shen, Y., Zhao, Y., Guo, Q., Jing, J., Lin, S., Zong, Z., 2015. Adverse effects of osteocytic constitutive activation of ß-catenin on bone strength and bone growth. J. Bone Miner. Res. 30, 1184–1194. doi:10.1002/jbmr.2453

Clarke, B., 2008. Normal Bone Anatomy and Physiology. Clin. J. Am. Soc. Nephrol. 3, S131–S139. doi:10.2215/CJN.04151206

Cohen, S.R., Kalfon-Cohen, E., 2013. Dynamic nanoindentation by instrumented nanoindentation and force microscopy: a comparative review. Beilstein J. Nanotechnol. 4, 815–33. doi:10.3762/bjnano.4.93

Collins, C.J., Vivanco, J.F., Sokn, S. a., Williams, B.O., Burgers, T. a., Ploeg, H.-L., 2015. Fracture healing in mice lacking Pten in osteoblasts: a micro-computed tomography image-based analysis of the mechanical properties of the femur. J. Biomech. 48, 310–317. doi:10.1016/j.jbiomech.2014.11.028

Currey, J., 2004. Incompatible mechanical properties in compact bone. J. Theor. Biol. 231, 569–580. doi:10.1016/j.jtbi.2004.07.013

Currey, J.D., 2002. Bones: Structure and Mechanics. Princeton University Press.

Dalla, A., Bankoff, P., 2012. Biomechanical Characteristics of the Bone, in: Human Musculoskeletal Biomechanics. InTech, p. 244.

Dalle Carbonare, L., Valenti, M.T., Bertoldo, F., Zanatta, M., Zenari, S., Realdi, G., Lo Cascio, V., Giannini, S., 2005. Bone microarchitecture evaluated by histomorphometry. Micron 36, 609–616. doi:10.1016/j.micron.2005.07.007

Davies, K.E., Nowak, K.J., 2006. Molecular mechanisms of muscular dystrophies: old and new players. Nat. Rev. Mol. Cell Biol. 7, 762–773. doi:10.1038/nrm2024

Davis, G.R., Wong, F.S., 1996. X-ray microtomography of bones and teeth. Physiol. Meas. 17, 121–46.

Deconinck, N., Dan, B., 2007. Pathophysiology of Duchenne Muscular Dystrophy: Current Hypotheses. Pediatr. Neurol. 36, 1–7. doi:10.1016/j.pediatrneurol.2006.09.016

Di Masso, R.J., Silva, P.S., Font, M.T., 2004. Muscle-bone relationships in mice selected for different body conformations. J. Musculoskelet. Neuronal Interact. 4, 41–7.

Di Virgilio, F., 2007. Liaisons dangereuses: P2X7 and the inflammasome. Trends Pharmacol. Sci. 28, 465–472. doi:10.1016/j.tips.2007.07.002

Donnelly, E., Chen, D.X., Boskey, A.L., Baker, S.P., C., M., Meulen, H. van der, 2010. Contribution of mineral to bone structural behavior and tissue mechanical properties. Calcif. Tissue Int. 87, 450–460. doi:10.1007/s00223-010-9404-x.Contribution

Doube, M., 2015. The ellipsoid factor for quantification of rods, plates, and intermediate forms in 3D geometries. Front. Endocrinol. (Lausanne). 6, 1–5. doi:10.3389/fendo.2015.00015

Doube, M., Conroy, A.W., Christiansen, P., Hutchinson, J.R., Shefelbine, S., 2009. Three-dimensional geometric analysis of felid limb bone allometry. PLoS One 4. doi:10.1371/journal.pone.0004742

Doube, M., Kłosowski, M.M., Arganda-carreras, I., Fabrice, P., 2010. BoneJ : free and extensible bone image analysis in ImageJ. Bone 47, 1076–1079. doi:10.1016/j.bone.2010.08.023.BoneJ

Doube, M., Klosowski, M.M., Wiktorowicz-Conroy, A.M., Hutchinson, J.R., Shefelbine, S.J., 2011. Trabecular bone scales allometrically in mammals and birds. Proc. Biol. Sci. 278, 3067–3073. doi:10.1098/rspb.2011.0069

Ervasti, J.M., 2007. Dystrophin, its interactions with other proteins, and implications for muscular dystrophy. Biochim. Biophys. Acta 1772, 108–17. doi:10.1016/j.bbadis.2006.05.010

Fan, Z., Swadener, J.G., Rho, J.Y., Roy, M.E., Pharr, G.M., 2002. Anisotropic properties of human tibial cortical bone as measured by nanoindentation. J. Orthop. Res. 20, 806–10. doi:10.1016/S0736-0266(01)00186-3

Ferrari, D., Munerati, M., Melchiorri, L., Hanau, S., di Virgilio, F., Baricordi, O.R., 1994. Responses to extracellular ATP of lymphoblastoid cell lines from Duchenne muscular dystrophy patients. Am. J. Physiol. 267, C886–C892.

Ferretti, J.L., Cointry, G.R., Capozza, R.F., Capiglioni, R., Chiappe, M. a, 2001. Analysis of biomechanical effects on bone and on the muscle-bone interactions in small animal models. J. Musculoskelet. Neuronal Interact. 1, 263–274.

Finnilä, M.A.J., Zioupos, P., Herlin, M., Miettinen, H.M., Simanainen, U., Håkansson, H., Tuukkanen, J., Viluksela, M., Jämsä, T., 2010. Effects of 2,3,7,8-tetrachlorodibenzo-p-dioxin exposure on bone material properties. J. Biomech. 43, 1097–103. doi:10.1016/j.jbiomech.2009.12.011

Frajacomo, F.T.T., Falcai, M.J., Fernandes, C.R., Shimano, A.C., Garcia, S.B., 2013. Biomechanical adaptations of mice cortical bone submitted to three different exercise modalities. Acta Ortop. Bras. 21, 328–32. doi:10.1590/S1413-78522013000600006

Fritton, J.C., Myers, E.R., Wright, T.M., van der Meulen, M.C.H., 2005. Loading induces site-specific increases in mineral content assessed by microcomputed tomography of the mouse tibia. Bone 36, 1030–8. doi:10.1016/j.bone.2005.02.013

Frost, H.M., 1987. Bone "Mass" and the "Mechanostat": A Proposal. Anat. Rec. 9.

Gartland, A., 2012. P2X receptors in bone 1, 221–227. doi:10.1002/wmts.26

Giordano, C., Mojumdar, K., Liang, F., Lemaire, C., Li, T., Richardson, J., Divangahi, M., Qureshi, S., Petrof, B.J., 2015. Toll-like receptor 4 ablation in mdx mice reveals innate immunity as a therapeutic target in Duchenne muscular dystrophy. Hum. Mol. Genet. 24, 2147–62. doi:10.1093/hmg/ddu735

Graeff, C., Timm, W., Nickelsen, T.N., Farrerons, J., Marín, F., Barker, C., Glüer, C.C., 2007. Monitoring teriparatide-associated changes in vertebral microstructure by high-resolution CT in vivo: results from the EUROFORS study. J. Bone Miner. Res. 22, 1426–1433. doi:10.1359/jbmr.070603

Gross, T.S., Poliachik, S.L., Prasad, J., Bain, S.D., 2010. The effect of muscle dysfunction on bone mass and morphology. J. Musculoskelet. Neuronal Interact. 10, 25–34.

Grounds, M.D., Radley, H.G., Lynch, G.S., Nagaraju, K., De Luca, A., 2008. Towards developing standard operating procedures for pre-clinical testing in the mdx mouse model of Duchenne muscular dystrophy. Neurobiol. Dis. 31, 1–19. doi:10.1016/j.nbd.2008.03.008

Gussoni, E., Soneoka, Y., Strickland, C.D., Buzney, E. a, Khan, M.K., Flint, a F., Kunkel, L.M., Mulligan, R.C., 1999. Dystrophin expression in the mdx mouse restored by stem cell transplantation. Nature 401, 390–394. doi:10.1038/43919

Habelitz, S., Marshall, S.J., Marshall, G.W., Balooch, M., 2001. Mechanical properties of human dental enamel on the nanometre scale. Arch. Oral Biol. 46, 173–83.

Hadjidakis, D.J., Androulakis, I.I., 2006. Bone remodeling. Ann. N. Y. Acad. Sci. 1092, 385–396. doi:10.1196/annals.1365.035

Hamed, E., Jasiuk, I., Yoo, A., Lee, Y., Liszka, T., 2012. Multi-scale modelling of elastic moduli of trabecular bone. J. R. Soc. Interface 9, 1654–73. doi:10.1098/rsif.2011.0814

Hengsberger, S., Kulik, a., Zysset, P.H., 2002. Nanoindentation discriminates the elastic properties of individual human bone lamellae under dry and physiological conditions. Bone 30, 178–184. doi:10.1016/S8756-3282(01)00624-X

Herlin, M., Finnilä, M. a J., Zioupos, P., Aula, A., Risteli, J., Miettinen, H.M., Jämsä, T., Tuukkanen, J., Korkalainen, M., Håkansson, H., Viluksela, M., 2013. New insights to the role of aryl hydrocarbon receptor in bone phenotype and in dioxin-induced modulation of bone microarchitecture and material properties. Toxicol. Appl. Pharmacol. 273, 219–26. doi:10.1016/j.taap.2013.09.002

Hessle, L., Stordalen, G. a., Wengl??n, C., Petzold, C., Tanner, E.K., Brorson, S.H., Baekkevold, E.S., ??Nnerfjord, P., Reinholt, F.P., Heineg??rd, D., 2013. The Skeletal Phenotype of Chondroadherin Deficient Mice. PLoS One 8, 1–11. doi:10.1371/journal.pone.0063080

Hildebrand, T., Rüegsegger, P., 1997. A new method for the model-independent assessment of thickness in three-dimensional images. J. Microsc. 185, 67–75. doi:10.1046/j.1365-2818.1997.1340694.x

Hoffler, C.E., 2005. An Application of Nanoindentation Technique to Measure Bone Tissue Lamellae Properties. J. Biomech. Eng. 127, 1046. doi:10.1115/1.2073671

Holdsworth, D.W., Thornton, M.M., 2002. Micro-CT in small animal and specimen imaging. Trends Biotechnol. 20, S34–S39. doi:10.1016/S0167-7799(02)02004-8

Hsu, P.-Y., Tsai, M.-T., Wang, S.-P., Chen, Y.-J., Wu, J., Hsu, J.-T., 2016. Cortical Bone Morphological and Trabecular Bone Microarchitectural Changes in the Mandible and Femoral Neck of Ovariectomized Rats. PLoS One 11, e0154367. doi:10.1371/journal.pone.0154367

Isaksson, H., Nagao, S., Małkiewicz, M., Julkunen, P., Nowak, R., Jurvelin, J.S., 2010. Precision of nanoindentation protocols for measurement of viscoelasticity in cortical and trabecular bone. J. Biomech. 43, 2410–7. doi:10.1016/j.jbiomech.2010.04.017

Ito, K., Kimura, S., Ozasa, S., Matsukura, M., Ikezawa, M., Yoshioka, K., Ueno, H., Suzuki, M., Araki, K., Yamamura, K.I., Miwa, T., Dickson, G., Thomas, G.D., Miike, T., 2006. Smooth muscle-specific dystrophin expression improves aberrant vasoregulation in mdx mice. Hum. Mol. Genet. 15, 2266–2275. doi:10.1093/hmg/ddl151

Jämsä, T., Rho, J.-Y., Fan, Z., MacKay, C. a, Marks, S.C., Tuukkanen, J., 2002. Mechanical properties in long bones of rat osteopetrotic mutations. J. Biomech. 35, 161–5.

Janc, K., Tarasiuk, J., Bonnet, A.S., Lipinski, P., 2013. Genetic algorithms as a useful tool for trabecular and cortical bone segmentation. Comput. Methods Programs Biomed. 111, 72–83. doi:10.1016/j.cmpb.2013.03.012

Jepsen, K.J., Silva, M.J., Vashishth, D., Guo, X.E., van der Meulen, M.C.H., 2015. Establishing Biomechanical Mechanisms in Mouse Models: Practical Guidelines for Systematically Evaluating Phenotypic Changes in the Diaphyses of Long Bones. J. Bone Miner. Res. n/a–n/a. doi:10.1002/jbmr.2539

Jiang, T., Yeung, D., Lien, C.F., Górecki, D.C., 2005. Localized expression of specific P2X receptors in dystrophin-deficient DMD and mdx muscle. Neuromuscul. Disord. 15, 225–36. doi:10.1016/j.nmd.2004.11.008

Jiang, Y., Zhao, J., White, D.L., Genant, H.K., 2000. Micro CT and Micro MR imaging of 3D architecture of animal skeleton. J. Musculoskelet. Neuronal Interact. 1, 45–51.

Jilka, R.L., 2013. The Relevance of Mouse Models for Investigating Age-Related Bone Loss in Humans. Journals Gerontol. Ser. A Biol. Sci. Med. Sci. 68, 1209–1217. doi:10.1093/gerona/glt046

Joan S. Weszka; Azriel Rosenfeld, 1978. Threshold Evaluation Techniques. IEEE Trans. Syst. Man , Cybernatics 8, 622–629.

Kapsa, R., Kornberg, A.J., Byrne, E., 2003. Novel therapies for Duchenne muscular dystrophy. Lancet Neurol. 2, 299–310. doi:10.1016/S1474-4422(03)00382-X

Kawahara, G., Gasperini, M.J., Myers, J.A., Widrick, J.J., Eran, A., Serafini, P.R., Alexander, M.S., Pletcher, M.T., Morris, C.A., Kunkel, L.M., 2014. Dystrophic muscle improvement in zebrafish via increased heme oxygenase signaling. Hum. Mol. Genet. 23, 1869–1878. doi:10.1093/hmg/ddt579

Keenan, M.J., Hegsted, M., Jones, K.L., Delany, J.P., Kime, J.C., Melancon, L.E., Tulley, R.T., Hong, K.D., 1997. Comparison of bone density measurement techniques: DXA and Archimedes' principle. J Bone Min. Res 12, 1903–1907. doi:10.1359/jbmr.1997.12.11.1903

Keene, B.E., Knowlton, K.F., McGilliard, M.L., Lawrence, L. a., Nickols-Richardson, S.M., Wilson, J.H., Rutledge, a. M., McDowell, L.R., Van Amburgh, M.E., 2004.

Measures of Bone Mineral Content in Mature Dairy Cows. J. Dairy Sci. 87, 3816–3825. doi:10.3168/jds.S0022-0302(04)73521-3

Klingler, W., Jurkat-Rott, K., Lehmann-Horn, F., Schleip, R., 2012. The role of fibrosis in Duchenne muscular dystrophy. Acta Myol. 31, 184–195.

Knuesel, I., Bornhauser, B.C., Zuellig, R. a., Heller, F., Schaub, M.C., Fritschy, J.M., 2000. Differential expression of utrophin and dystrophin in CNS neurons: An in situ hybridization and immunohistochemical study. J. Comp. Neurol. 422, 594–611. doi:10.1002/1096-9861(20000710)422:4<594::AID-CNE8>3.0.CO;2-Q

Kohler, T., Beyeler, M., Webster, D., Müller, R., 2005. Compartmental bone morphometry in the mouse femur: reproducibility and resolution dependence of microtomographic measurements. Calcif. Tissue Int. 77, 281–90. doi:10.1007/s00223-005-0039-2

Kornegay, J., Bogan, J., Bogan, D., Childers, M., Li, J., Nghiem, P., Detwiler, D., Larsen, C., Grange, R., Bhavaraju-Sanka, R., Tou, S., Keene, B., Jr, H.J., Wang, J., Fan, Z., Schatzberg, S., Styner, M., Flanigan, K., Xiao, X., Hoffman, E., 2012. Canine models of Duchenne muscular dystrophy and their use in therapeutic strategies. Mamm. Genome 23, 85–108. doi:10.1007/s00335-011-9382-y.Canine

Krasowska, E., Zab??ocki, K., G??recki, D.C., Swinny, J.D., 2014. Aberrant location of inhibitory synaptic marker proteins in the hippocampus of dystrophin-deficient mice: Implications for cognitive impairment in Duchenne muscular dystrophy. PLoS One 9. doi:10.1371/journal.pone.0108364

Kvist, T.M., Schwarz, P., Jørgensen, N.R., 2014. The P2X7 receptor: A key player in immune-mediated bone loss? Sci. World J. 2014. doi:10.1155/2014/954530

Lewis, G., Nyman, J.S., 2008. The use of nanoindentation for characterizing the properties of mineralized hard tissues: state-of-the art review. J. Biomed. Mater. Res. B. Appl. Biomater. 87, 286–301. doi:10.1002/jbm.b.31092

Li, S., Abdel-Wahab, A., Silberschmidt, V. V., 2013. Analysis of fracture processes in cortical bone tissue. Eng. Fract. Mech. 110, 448–458. doi:10.1016/j.engfracmech.2012.11.020

Liu, X.S., Bevill, G., Keaveny, T.M., Sajda, P., Guo, X.E., 2009. Micromechanical analyses of vertebral trabecular bone based on individual trabeculae segmentation of plates and rods. J. Biomech. 42, 249–56. doi:10.1016/j.jbiomech.2008.10.035

Lovering, R.M., Porter, N.C., Bloch, R.J., 2005. The Muscular Dystrophies: From Genes to Therapies. Phys. Ther. 85, 1372–1388.

Lynch, M.E., Main, R.P., Xu, Q., Walsh, D.J., Schaffler, M.B., Wright, T.M., van der Meulen, M.C.H., 2010. Cancellous bone adaptation to tibial compression is not sex dependent in growing mice. J. Appl. Physiol. 109, 685–691. doi:10.1152/japplphysiol.00210.2010

Macintosh, A. a., Davies, T.G., Ryan, T.M., Shaw, C.N., Stock, J.T., 2013. Periosteal versus true cross-sectional geometry: A comparison along humeral, femoral, and tibial diaphyses. Am. J. Phys. Anthropol. 150, 442–452. doi:10.1002/ajpa.22218

Maïmoun, L., Brennan-Speranza, T.C., Rizzoli, R., Ammann, P., 2012. Effects of ovariectomy on the changes in microarchitecture and material level properties in response to hind leg disuse in female rats. Bone 51, 586–591. doi:10.1016/j.bone.2012.05.001

Malshe, A.P., Rajurkar, K.P., Virwani, K.R., Taylor, C.R., Bourell, D.L., Levy, G., Sundaram, M.M., McGeough, J.A., Kalyanasundaram, V., Samant, A.N., 2010. Tip-based nanomanufacturing by electrical, chemical, mechanical and thermal processes. CIRP Ann. - Manuf. Technol. 59, 628–651. doi:10.1016/j.cirp.2010.05.006

Manolagas, S.C., 2000. Birth and death of bone cells: basic regulatory mechanisms and implications for the pathogenesis and treatment of osteoporosis. Endocr Rev 21, 115–137. doi:10.1210/edrv.21.2.0395

Martı́n-Badosa, E., Amblard, D., Nuzzo, S., Elmoutaouakkil, A., Vico, L., Peyrin, F., 2003. Excised Bone Structures in Mice : Imaging at Three-dimensional Synchotron Micro CT. Radiology 229, 921–928. doi:10.1148/radiol.2293020558

Mateos-Perez, J.M., Pascau, J., 2013. Image Processing with ImageJ. Packt Publishing Ltd.

McDonald, D.G.M., Kinali, M., Gallagher, A.C., Mercuri, E., Muntoni, F., Roper, H., Jardine, P., Jones, D.H., Pike, M.G., 2002. Fracture prevalence in Duchenne muscular dystrophy. Dev. Med. Child Neurol. 44, 695–8.

McGreevy, J.W., Hakim, C.H., McIntosh, M. a., Duan, D., 2015. Animal models of Duchenne muscular dystrophy: from basic mechanisms to gene therapy. Dis. Model. Mech. 8, 195–213. doi:10.1242/dmm.018424

Meganck, J.A., Kozloff, K.M., Thornton, M.M., Broski, S.M., Goldstein, S.A., 2009. Beam hardening artifacts in micro-computed tomography scanning can be reduced by X-ray beam filtration and the resulting images can be used to accurately measure BMD. Bone 45, 1104–16. doi:10.1016/j.bone.2009.07.078

Melville, K.M., Kelly, N.H., Khan, S. a, Schimenti, J.C., Ross, F.P., Main, R.P., van der Meulen, M.C., 2014. Female mice lacking estrogen receptor-alpha in osteoblasts have compromised bone mass and strength. J Bone Min. Res 29, 370–379. doi:10.1002/jbmr.2082

Monir, A.U., Gundberg, C.M., Yagerman, S.E., van der Meulen, M.C.H., Budell, W.C., Boskey, a. L., Dowd, T.L., 2010. The effect of lead on bone mineral properties from female adult C57/BL6 mice. Bone 47, 888–894. doi:10.1016/j.bone.2010.07.013

Montgomery, E., Pennington, C., Isales, C.M., Hamrick, M.W., 2005. Muscle-bone interactions in dystrophin-deficient and myostatin-deficient mice. Anat. Rec. A. Discov. Mol. Cell. Evol. Biol. 286, 814–22. doi:10.1002/ar.a.20224

Morgenroth, V.H., Hache, L.P., Clemens, P.R., 2012. Insights into bone health in Duchenne muscular dystrophy. Bonekey Rep. 1, 1–11. doi:10.1038/bonekey.2012.5

Moukhles, H., Carbonetto, S., 2001. Dystroglycan contributes to the formation of multiple dystrophin-like complexes in brain. J. Neurochem. 78, 824–834. doi:10.1046/j.1471-4159.2001.00466.x

Müller, R., Damme, B.V.A.N., Perre, G.V.A.N.D.E.R., Dequeker, J., Hildebrand, T., Ruegsegger, P., 1998. Morphometric Analysis of Human Bone Biopsies : A Quantitative Structural Comparison of Histological Sections and Micro-Computed Tomography. Bone 23, 59–66. doi:10.1016/S8756-3282(98)00068-4

Nakagaki, W.R., Bertran, C.A., Matsumura, C.Y., Santo-Neto, H., Camilli, J.A., 2011. Mechanical, biochemical and morphometric alterations in the femur of mdx mice. Bone 48, 372–379. doi:10.1016/j.bone.2010.09.011

Nakagaki, W.R., Camilli, J.A., 2012. Bone tissue and muscle dystrophin deficiency in mdx mice. Joint. Bone. Spine 79, 129–33. doi:10.1016/j.jbspin.2011.08.004

Novotny, S.A., Warren, G.L., Lin, A.S., Gulderg, R.E., Kristen, A., Lowe, D.A., 2011. Bone is functionally impaired in dystrophic mice but less so than skeletal muscle than skeletal muscle. Neuromuscul. Disord. 21, 183–193. doi:10.1016/j.nmd.2010.12.002.Bone

Nowak, K.J., Davies, K.E., 2004. Duchenne muscular dystrophy and dystrophin: pathogenesis and opportunities for treatment. EMBO Rep. 5, 872–6. doi:10.1038/sj.embor.7400221

Odgaard, A., 1997. Three-dimensional methods for quantification of cancellous bone architecture. Bone 20, 315–28.

Oftadeh, R., Entezari, V., Spo, G., Villa-camacho, J.C., Krigbaum, H., Strawich, E., Graham, L., Rey, C., Chiu, H., Hashemi, H.N., Vaziri, A., Nazarian, A., 2015. Hierarchical analysis and multi-scale modelling of rat cortical and trabecular bone. J. R. Soc. Interface 12, 5–7.

Oliver, W.C., Pharr, G.M., 2004. Measurement of hardness and elastic modulus by instrumented indentation: Advances in understanding and refinements to methodology. J. Mater. Res. 19, 3–20. doi:10.1557/jmr.2004.19.1.3

Oppl, B., Michitsch, G., Misof, B., Kudlacek, S., Donis, J., Klaushofer, K., Zwerina, J., Zwettler, E., 2014. Low Bone Mineral Density and Fragility Fractures in Permanent Vegetative State Patients. J. Bone Miner. Res. 29, 1096–1100. doi:10.1002/jbmr.2122

Pant, M., Sopariwala, D.H., Bal, N.C., Lowe, J., Delfín, D. a., Rafael-Fortney, J., Periasamy, M., 2015. Metabolic Dysfunction and Altered Mitochondrial Dynamics in the Utrophin-Dystrophin Deficient Mouse Model of Duchenne Muscular Dystrophy. PLoS One 10, e0123875. doi:10.1371/journal.pone.0123875

Parfitt, A., Drezner, M.K., Glorieux, F.H., Kanis, J.A., Malluche, H., Meunier, P.J., Ott, S.M., Recker, R.R., 1987. Bone Histomorphometry: Standardization of Nomenclature, Symbols, and Units. J. Bone Miner. Res. 2, 595–610. doi:10.1002/jbmr.5650020617

Paulus, M.J., Gleason, S.S., Kennel, S.J., Hunsicker, P.R., Johnson, D.K., 2000. High resolution X-ray computed tomography: an emerging tool for small animal cancer research. Neoplasia 2, 62–70.

Poundarik, A. a., Vashishth, D., 2015. Multiscale imaging of bone microdamage. Connect. Tissue Res. 56, 87–98. doi:10.3109/03008207.2015.1008133

Pouwels, S., De Boer, A., Leufkens, H.G.M., Weber, W.E.J., Cooper, C., Van Onzenoort, H. a W., De Vries, F., 2013. Risk of fracture in patients with muscular dystrophies. Osteoporos. Int. 25, 509–518. doi:10.1007/s00198-013-2442-2

R.Krug, AJ Burghardt , S. Majumdar, T.M., 2011. High-resolution Imaging Techniques for the Assessment of Osteoporosis. Radiol Clin North Am 48, 601–621. doi:10.1016/j.rcl.2010.02.015.High-resolution

Rasic, M. V., Vojinovic, D., Pesovic, J., Mijalkovic, G., Lukic, V., Mladenovic, J., Kosac, a., Novakovic, I., Maksimovic, N., Romac, S., Todorovic, S., Pavicevic, S.D., 2014. Intellectual Ability in the Duchenne Muscular Dystrophy and Dystrophin Gene Mutation Location. Balk. J. Med. Genet. 17, 25–36. doi:10.2478/bjmg-2014-0071

Redlich, K., Smolen, J.S., 2012. Inflammatory bone loss: pathogenesis and therapeutic intervention. Nat. Rev. Drug Discov. 11, 234–250. doi:10.1038/nrd3669

Rho, J.Y., Kuhn-Spearing, L., Zioupos, P., 1998. Mechanical properties and the hierarchical structure of bone. Med. Eng. Phys. 20, 92–102. doi:10.1016/S1350-4533(98)00007-1

Ridler, T.W., Calvard, S., 1978. Picture Thresholding Using an Iterative Selection Method. IEEE Trans. Syst. Man , Cybernatics 630–632.

Rietbergen, B. Van, Odgaard, A., Kabel, J., Huiskes, R., 1996. Direct mechanics assessment of elastic symmetries and properties of trabecular bone architecture. Biomechanics 29, 1653–1657. doi:10.1016/S0021-9290(96)80021-2

Ritchie, R.O., Koester, K.J., Ionova, S., Yao, W., Lane, N.E., Ager, J.W., 2008. Measurement of the toughness of bone: a tutorial with special reference to small animal studies. Bone 43, 798–812. doi:10.1016/j.bone.2008.04.027

Ritman, E.L., 2006. Medical X-ray Imaging, Current Status and Some Future Challenges. Copyr. ©JCPDS-International Cent. Diffr. Data 1–12.

Ritman, E.L., 2002. Molecular imaging in small animals--roles for micro-CT. J. Cell. Biochem. Suppl. 39, 116–24. doi:10.1002/jcb.10415

Rodriguez-Florez, N., Garcia-Tunon, E., Mukadam, Q., Saiz, E., Oldknow, K.J., Farquharson, C., Millán, J.L., Boyde, A., Shefelbine, S.J., 2014. An investigation of the mineral in ductile and brittle cortical mouse bone. J. Bone Miner. Res. doi:10.1002/jbmr.2414

Rodriguez-Florez, N., Oyen, M.L., Shefelbine, S.J., 2013. Insight into differences in nanoindentation properties of bone. J. Mech. Behav. Biomed. Mater. 18, 90–9. doi:10.1016/j.jmbbm.2012.11.005

Rubin, M. a., Rubin, J., Jasiuk, I., 2004. SEM and TEM study of the hierarchical structure of C57BL/6J and C3H/HeJ mice trabecular bone. Bone 35, 11–20. doi:10.1016/j.bone.2004.02.008

Rueckel, J., Stockmar, M., Pfeiffer, F., Herzen, J., 2014. Spatial resolution characterization of a X-ray microCT system. Appl. Radiat. Isot. 94, 230–4. doi:10.1016/j.apradiso.2014.08.014

Rufo, A., Del Fattore, A., Capulli, M., Carvello, F., De Pasquale, L., Ferrari, S., Pierroz, D., Morandi, L., De Simone, M., Rucci, N., Bertini, E., Bianchi, M.L., De Benedetti, F., Teti, A., 2011. Mechanisms inducing low bone density in Duchenne muscular dystrophy in mice and humans. J. Bone Miner. Res. 26, 1891–903. doi:10.1002/jbmr.410

Russ, J.C., Dehoff, R.T., 2001. Practical Stereology. doi:10.1007/978-1-4615-1233-2

Saito, M., Marumo, K., 2010. Collagen cross-links as a determinant of bone quality: a possible explanation for bone fragility in aging, osteoporosis, and diabetes mellitus. Int. Osteoporos. 21, 195–214. doi:10.1007/s00198-009-1066-z

Salmon, P.L., Ohlsson, C., Shefelbine, S.J., Doube, M., 2015. Structure Model Index Does Not Measure Rods and Plates in Trabecular Bone. Front. Endocrinol. (Lausanne). 6, 1–10. doi:10.3389/fendo.2015.00162

Schambach, S.J., Bag, S., Schilling, L., Groden, C., Brockmann, M. a., 2010. Application of micro-CT in small animal imaging. Methods 50, 2–13. doi:10.1016/j.ymeth.2009.08.007

Seeman, E., 2008. Bone quality: The material and structural basis of bone strength. J. Bone Miner. Metab. 26, 1–8. doi:10.1007/s00774-007-0793-5

Sharir, A., Barak, M.M., Shahar, R., 2008. Whole bone mechanics and mechanical testing. Vet. J. 177, 8–17. doi:10.1016/j.tvjl.2007.09.012

Shepherd, T.N., Zhang, J., Ovaert, T.C., Roeder, R.K., Niebur, G.L., 2011. Direct comparison of nanoindentation and macroscopic measurements of bone viscoelasticity. J Mech Behav Biomed Mater. 4, 2055–2062. doi:10.1016/j.jmbbm.2011.07.004

Sikavitsas, V.I., Temenoff, J.S., Mikos, A.G., 2001. Biomaterials and bone mechanotransduction. Biomaterials 22, 2581–2593. doi:10.1016/S0142-9612(01)00002-3

Silva, M.J., Brodt, M.D., Ettner, S.L., 2002. Long bones from the senescence accelerated mouse SAMP6 have increased size but reduced whole-bone strength and resistance to fracture. J. Bone Miner. Res. 17, 1597–1603. doi:10.1359/jbmr.2002.17.9.1597

Silva, M.J., Brodt, M.D., Fan, Z., Rho, J.-Y., 2004. Nanoindentation and whole-bone bending estimates of material properties in bones from the senescence accelerated mouse SAMP6. J. Biomech. 37, 1639–46. doi:10.1016/j.jbiomech.2004.02.018

Silva, M.J., Brodt, M.D., Hucker, W.J., 2005. Finite element analysis of the mouse tibia: estimating endocortical strain during three-point bending in SAMP6 osteoporotic mice. Anat. Rec. A. Discov. Mol. Cell. Evol. Biol. 283, 380–90. doi:10.1002/ar.a.20171

Silva, M.J., Brodt, M.D., Wopenka, B., Thomopoulos, S., Williams, D., Wassen, M.H., Ko, M., Kusano, N., Bank, R. a, 2006. Decreased Collagen Organization and Content Are Associated With Reduced Strength of Demineralized and Intact Bone in the SAMP6 Mouse. J Bone Min. Res 21, 78–88. doi:10.1359/JBMR.050909

Sinadinos, A., Young, C., Al-Khalidi, R., Teti, A., Kalinski, P., Mohamad, S., Floriot, L., Henry, T., Tozzi, G., Jiang, T., Wurtz, O., Lefebvre, A., Tong, J., Vaudry, D., Arkle, S., DoRego, J.-C., Gorecki, D., Shugay, M., 2015. P2RX7 Purinoceptor: A

Therapeutic Target for Ameliorating the Symptoms of Duchenne Muscular Dystrophy. PLoS Med 12(10), 1–33. doi:10.1371/journal.pmed.1001888

Söderpalm, A.-C., Magnusson, P., Ahlander, A.-C., Karlsson, J., Kroksmark, A.-K., Tulinius, M., Swolin-Eide, D., 2007. Low bone mineral density and decreased bone turnover in Duchenne muscular dystrophy. Neuromuscul. Disord. 17, 919–28. doi:10.1016/j.nmd.2007.05.008

Solle, M., Labasi, J., Perregaux, D.G., Stam, E., Petrushova, N., Koller, B.H., Griffiths, R.J., Gabel, C. a., 2001. Altered cytokine production in mice lacking P2X7 receptors. J. Biol. Chem. 276, 125–132. doi:10.1074/jbc.M006781200

Stock, S.R., 2009. MicroComputed Tomography: methodology and applications. Taylor & Francis Group, United States of America.

Sun, J., Ling, M., Wang, Y., Chen, D., Zhang, S., Tong, J., Wang, S., 2014. Quasi-Static and Dynamic Nanoindentation of Some Selected Biomaterials. J. Bionic Eng. 11, 144–150. doi:10.1016/S1672-6529(14)60029-9

Swaminathan, R., 2001. Biochemical markers of bone turnover. Clin. Chim. Acta 313, 95–105. doi:10.1016/S0009-8981(01)00656-8

Taylor, P.J., Betts, G. a., Maroulis, S., Gilissen, C., Pedersen, R.L., Mowat, D.R., Johnston, H.M., Buckley, M.F., 2010. Dystrophin gene mutation location and the risk of cognitive impairment in duchenne muscular dystrophy. PLoS One 5. doi:10.1371/journal.pone.0008803

Thomsen, J.S., Laib, a., Koller, B., Prohaska, S., Mosekilde, L., Gowin, W., 2005. Stereological measures of trabecular bone structure: Comparison of 3D micro computed tomography with 2D histological sections in human proximal tibial bone biopsies. J. Microsc. 218, 171–179. doi:10.1111/j.1365-2818.2005.01469.x

Tor Hildebrand, Ruegsegger, P., 1997. Quantification of Bone Microarchitecture with the SMI. CMBBE 1, 15–23.

Toriwaki, J., Yonekura, T., 2002. Euler Number and Connectivity Indexes of a Three Dimensional Digital Picture. Forma 17, 183–209.

Treuting, P.M., Dintzis, S.M. (Eds.), 2012. Comparative Anatomy and Histology: A Mouse and Human Atlas. Academic Press.

Turk, R., Sterrenburg, E., de Meijer, E.J., van Ommen, G.-J.B., den Dunnen, J.T., 't Hoen, P. a C., 2005. Muscle regeneration in dystrophin-deficient mdx mice studied by gene expression profiling. BMC Genomics 6, 98. doi:10.1186/1471-2164-6-98

Turner, C.H., 2006. Bone strength: current concepts. Ann. N. Y. Acad. Sci. 1068, 429–46. doi:10.1196/annals.1346.039

Turner, C.H., Bouxsein, M.L., Hsieh, Y., Muller, R., Rosen, C.J., Mccrann, M.E., Donahue, L.R.A.E., Beamer, W.G., 2001. Variation in Bone Biomechanical Properties , Microstructure, and Density in BXH Recombinant Inbred Mice. Bone Miner. Res. 16, 206–213.

Turner, C.H., Burr, D.B., 1993. Basic biomechanical measurements of bone: A tutorial. Bone 14, 595–608.

Turner, C.H., Hsieh, Y.F., Müller, R., Bouxsein, M.L., Baylink, D.J., Rosen, C.J., Grynpas, M.D., Donahue, L.R., Beamer, W.G., 2000. Genetic regulation of cortical and trabecular bone strength and microstructure in inbred strains of mice. J. Bone Miner. Res. 15, 1126–1131. doi:10.1359/jbmr.2000.15.6.1126

Turner, C.H., Rho, J., Takano, Y., Tsui, T.Y., Pharr, G.M., 1999. The elastic properties of trabecular and cortical bone tissues are similar: results from two microscopic measurement techniques. J. Biomech. 32, 437–41.

Tyrovola, J.B., 2015. The "Mechanostat Theory" of Frost and the OPG/RANKL/RANK System. J. Cell. Biochem. 117, 2724–2729. doi:10.1002/jcb.25265

Van der Meulen, M.C.H., Jepsen, K.J., Miki, B., 2001. Understanding bone strength: Size isn't everything. Bone 29, 101–104. doi:10.1016/S8756-3282(01)00491-4

Van Lenthe, G.H., Voide, R., Boyd, S.K., Müller, R., 2008. Tissue modulus calculated from beam theory is biased by bone size and geometry: Implications for the use of three-point bending tests to determine bone tissue modulus. Bone 43, 717–723. doi:10.1016/j.bone.2008.06.008

Vashishth, D., 2008. Small Animal Bone Mechanics. Bone 43, 794–797. doi:10.1016/j.bone.2008.06.013.Small

Vashishth, D., 2007. The role of the collagen matrix in skeletal fragility. Curr. Osteoporos. Rep. 5, 62–66. doi:10.1007/s11914-007-0004-2

Verdelis, K., Lukashova, L., Atti, E., Mayer-Kuckuk, P., Peterson, M.G.E., Tetradis, S., Boskey, a L., van der Meulen, M.C.H., 2011. MicroCT morphometry analysis of mouse cancellous bone: intra- and inter-system reproducibility. Bone 49, 580–7. doi:10.1016/j.bone.2011.05.013

Vestergaard, P., Glerup, H., Steffensen, B.F., Rejnmark, L., Rahbek, J., Moseklide, L., 2001. Fracture risk in patients with muscular dystrophy and spinal muscular atrophy. J. Rehabil. Med. 33, 150–155.

Volkman, S.K., Galecki, A.T., Burke, D.T., Miller, R. a, Goldstein, S. a, 2004. Quantitative trait loci that modulate femoral mechanical properties in a genetically heterogeneous mouse population. J. Bone Miner. Res. 19, 1497–1505. doi:10.1359/JBMR.040506

Waarsing, J.H., Day, J.S., Weinans, H., 2004. An improved segmentation method for in vivo microCT imaging. J. Bone Miner. Res. 19, 1640–50. doi:10.1359/JBMR.040705

Wagner, K.R., 2008. Approaching a new age in Duchenne muscular dystrophy treatment. Neurotherapeutics 5, 583–91. doi:10.1016/j.nurt.2008.08.013

Wallace, J., Rajachar, R.M., Allen, M.R., Bloomfield, S.A., Robey, P.G., Young, M.F., Kohn, D.H., 2007. Exercise-Induced Changes in the Cortical Bone of Growing Mice Are Bone and Gender Specific. Bone 40, 1120–1127. doi:10.1016/j.bone.2006.12.002

Wang, B., 2010. Gene Therapy and Muscles: The Use of Adeno-associated Virus— Where are We Today? Oper. Tech. Orthop. 20, 136–143. doi:10.1053/j.oto.2009.10.011

Wang, J., Kazakia, G.J., Zhou, B., Shi, X.T., Guo, X.E., 2015. Distinct Tissue Mineral Density in Plate- and Rod-like Trabeculae of Human Trabecular Bone. J. Bone Miner. Res. 30, 1641–1650. doi:10.1002/jbmr.2498

Wang, X., Shen, X., Li, X., Mauli Agrawal, C., 2002. Age-related changes in the collagen network and toughness of bone. Bone 31, 1–7. doi:10.1016/S8756-3282(01)00697-4

Weiner, S., Wagner, H.D., 1998. The Material Bone: Structure-Mechanical Function Relations. Annu. Rev. Mater. Sci. 28, 271–298. doi:10.1146/annurev.matsci.28.1.271

Wergedal, J.E., Ackert-Bicknell, C.L., Tsaih, S.-W., Sheng, M.H.-C., Li, R., Mohan, S., Beamer, W.G., Churchill, G. a, Baylink, D.J., 2006. Femur mechanical properties in the F2 progeny of an NZB/B1NJ x RF/J cross are regulated predominantly by genetic loci that regulate bone geometry. J. Bone Miner. Res. 21, 1256–1266. doi:10.1359/jbmr.060510

Whitmore, C., Morgan, J., 2014. What do mouse models of muscular dystrophy tell us about the DAPC and its components? Int. J. Exp. Pathol. 95, 365–377. doi:10.1111/iep.12095

Yeung, D., Zablocki, K., Lien, C.-F., Jiang, T., Arkle, S., Brutkowski, W., Brown, J., Lochmuller, H., Simon, J., Barnard, E. a, Górecki, D.C., 2006. Increased susceptibility to ATP via alteration of P2X receptor function in dystrophic mdx mouse muscle cells. FASEB J. 20, 610–620. doi:10.1096/fj.05-4022com

You, L., Temiyasathit, S., Lee, P., Kim, C.H., Tummala, P., Yao, W., Kingery, W., Malone, A.M., Kwon, R.Y., Jacobs, C.R., 2008. Osteocytes as mechanosensors in the inhibition of bone resorption due to mechanical loading. Bone 42, 172–179. doi:10.1016/j.bone.2007.09.047

Young, C.N., Sinadinos, A., Lefebvre, A., Chan, P., Arkle, S., Vaudry, D., Gorecki, D.C., 2015. A novel mechanism of autophagic cell death in dystrophic muscle regulated by P2RX7 receptor large-pore formation and HSP90. Autophagy 11, 113–130. doi:10.4161/15548627.2014.994402

Young, C.N.J., Brutkowski, W., Lien, C.-F., Arkle, S., Lochmüller, H., Zabłocki, K., Górecki, D.C., 2012. P2X7 purinoceptor alterations in dystrophic mdx mouse muscles: relationship to pathology and potential target for treatment. J. Cell. Mol. Med. 16, 1026–37. doi:10.1111/j.1582-4934.2011.01397.x

Young, C.N.J., Sinadinos, A., Gorecki, D.C., 2013. P2X receptor signaling in skeletal muscle health and disease. Wiley Interdiscip. Rev. Membr. Transp. Signal. 2, 265–274. doi:10.1002/wmts.96

Young, W.C., Budynas, R.G., 2002. Formulas for Stress and Strain, 7th ed, Journal of Applied Mechanics. doi:10.1115/1.3423917

Zhang, R., Gong, H., Zhu, D., Ma, R., Fang, J., Fan, Y., 2015. Multi-level femoral morphology and mechanical properties of rats of different ages. Bone 76, 76–87. doi:10.1016/j.bone.2015.03.022

Zhang, Y., Huang, J., Jiao, Y., David, V., Kocak, M., Roan, E., Di'Angelo, D., Lu, L., Hasty, K. a., Gu, W., 2015. Bone Morphology in 46 BXD Recombinant Inbred Strains and Femur-Tibia Correlation. Sci. World J. 2015, 1–8. doi:10.1155/2015/728278

Zhao, S., Zhang, Y.K.Y., Harris, S., Ahuja, S.S., Bonewald, L.F., 2002. MLO-Y4 osteocyte-like cells support osteoclast formation and activation. J. Bone Miner. Res. 17, 2068–2079. doi:10.1359/jbmr.2002.17.11.2068

Zioupos, P., 2005. In vivo fatigue microcracks in human bone : Material properties of the surrounding bone matrix. Eur. J. Morphol. 42, 31–41. doi:10.1080/09243860500095463

Zioupos, P., Currey, J.D., 1998. Changes in the stiffness, strength, and toughness of human cortical bone with age. Bone 22, 57–66.

Zioupos, P., Gresle, M., Winwood, K., 2008. Fatigue strength of human cortical bone: age, physical, and material heterogeneity effects. J. Biomed. Mater. Res. A 86, 627–36. doi:10.1002/jbm.a.31576

Zioupos, P., Rogers, K.D., 2006. Complementary Physical and Mechanical Techniques to Characterise Tooth: A Bone-like Tissue. J. Bionic Eng. 3, 19–31. doi:10.1016/S1672-6529(06)60003-6

Zysset, P.K., Guo, X.E., Hoffler, C.E., Kristin E. Moore, Goldstein, S.A., 1999. Elastic modulus and hardness of cortical and trabecular bone lamellae measured by nanoindentation in the human femur. J. Biomech. 32, 1005–1012.